EVOLUTION OF NEOGENE FAULT POPULATIONS IN
NORTHERN OWENS VALLEY, CALIFORNIA
AND IMPLICATIONS FOR THE EASTERN CALIFORNIA SHEAR ZONE

AN ABSTRACT

SUBMITTED ON THE 18th DAY OF JANUARY 2007

TO THE DEPARTMENT OF EARTH AND ENVIRONMENTAL SCIENCES

IN PARTIAL FULFILLMENT OF THE REQUIREMENTS
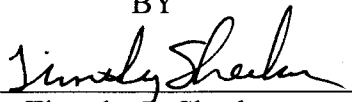
OF THE SCHOOL OF SCIENCE AND ENGINEERING

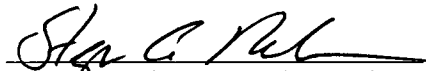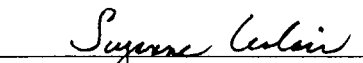OF TULANE UNIVERSITY

FOR THE DEGREE

OF

DOCTOR OF PHILOSOPHY

BY

_____
Timothy P. Sheehan

APPROVED: _____
Dr. Nancye H. Dawers, Ph.D.

_____
Dr. Stephen A. Nelson, Ph.D.

_____
Dr. Suzanne Leclair, Ph.D.

_____
Dr. Alex Densmore, Ph.D.

ABSTRACT

Field observations of faulting and associated deformation are used here to reconstruct the structural and kinematic evolution of northern Owens Valley, California. This work consists of three stand-alone research contributions (Chapters Three, Four, and Five). Chapter Three presents a model for the structural evolution of northern Owens Valley; focusing on the origin and evolution of the "Coyote Warp", as well as the relationship between normal shear along the Sierran Nevada range-front and dextral shear along the Owens Valley fault zone. This model relies on the theoretical relationship between fault spacing, fault dip, and seismogenic thickness in order to make predictions of crustal-scale conjugate normal fault intersection. Application of this model suggests that the structural evolution of northern Owens Valley can be explained in the context of a failed conjugate system, whereby fault intersection within the seismogenic crust results in the locking of one of the graben faults, and subsequent asymmetric range uplift and adjacent basin subsidence. Chapter Four presents a geologically based extensional slip rate history for the central portion of northern Owens Valley. Results suggest that the rate of extensional strain increased significantly since Middle Pleistocene time. These results are in agreement with similar observations of extension within and around northern Owens Valley, and correspond to a decrease in nearby rates of dextral shear over the same time interval. These observations are explained by a counter-clockwise rotation in the orientation of regional shear since Middle Pleistocene time. Furthermore, results from this study contribute to a geologically based extensional slip budget that is in agreement with geodetic based estimates of present-day strain accumulation. In Chapter Five, observations of fault length from several normal fault populations are used to examine the mechanisms that control the distribution of strain within the Eastern California Shear Zone. Results suggest that boundary fault spacing within shear induced fault networks plays a significant role in the redistribution of slip by placing geometric limitations on intermediary cross-cutting normal faults. Such redistribution is expected to occur over a timescale that is related to the lifespan of these constrained faults.

EVOLUTION OF NEOGENE FAULT POPULATIONS IN
NORTHERN OWENS VALLEY, CALIFORNIA
AND IMPLICATIONS FOR THE EASTERN CALIFORNIA SHEAR ZONE

A DISSERTATION

SUBMITTED ON THE 18th DAY OF JANUARY 2007

TO THE DEPARTMENT OF EARTH AND ENVIRONMENTAL SCIENCES

IN PARTIAL FULFILLMENT OF THE REQUIREMENTS

OF THE SCHOOL OF SCIENCE AND ENGINEERING
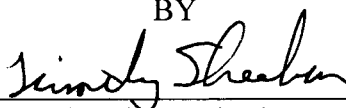
OF TULANE UNIVERSITY

FOR THE DEGREE

OF

DOCTOR OF PHILOSOPHY

BY

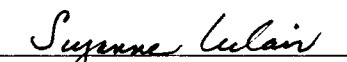_____
Timothy P. Sheehan

APPROVED: _____
Dr. Nancye H. Dawers, Ph.D.

_____
Dr. Stephen A. Nelson, Ph.D.

_____
Dr. Suzanne Leclair, Ph.D.

_____
Dr. Alex Densmore, Ph.D.

ACKNOWLEDGEMENT

TABLE OF CONTENTS

LIST OF TABLES

LIST OF FIGURES

Chapter 1

Introduction

Characterization of crustal deformation over several temporal and spatial scales is vital to formulating models of structural and kinematic evolution in tectonically active regions. Such characterization provides a basis for interpreting the processes that shape Earth's crust, and facilitates an understanding of the human risks and hazards posed by such processes. Plate boundaries provide an ideal natural laboratory to explore these processes, as they are the primary locus of tectonically induced deformation.

Geomorphic analyses provide a fundamental means to characterize the nature of crustal reorganization. For example, offset geomorphic markers are often used in order to place constraints on the magnitude and, if reliably dated, the rates of deformation assigned to tectonic faults. Analysis and compilation of fault attributes, in terms of the nature of slip, rate, magnitude of offset, and relation to other faults within a given tectonic domain yields important insights into past and present deformation, which are utilized in reconstructing kinematic and structural histories.

This study focuses on Neogene faulting within northern Owens Valley California, located within the Eastern California shear zone (ECSZ); a region encompassing a significant portion of shear tectonism associated with the North American-Pacific plate boundary (Figure 2-1; Chapter 2). Previous study within this region has yielded insights into the nature and distribution of deformation within this complex system, and has

provided a framework within which to focus the present study. In particular, rates of fault slip based on geologic data (e.g. Dokka and Travis, 1990; Beanland and Clark, 1994; Reheis and Sawyer, 1997; Lee et al., 2001a), and geodetically measured rates of present-day strain accumulation (e.g. Argus and Gordon, 1990; Savage and Lisowski, 1995; Dixon et al., 1995, Bennett et al 1999; Thatcher et al., 1999; Dixon et al., 2000; Miller et al., 2001; McClusky et al., 2001; Oldow et al., 2001) define the ECSZ as a regionally diffuse (i.e. ~100 km across) zone of active deformation that is characterized by several locally concentrated zones of dextral shear.

Owens Valley itself has been the subject of several investigations concerned with the general character (Bateman, 1965; Bryant, 1984) and rate of deformation (Gillespie, 1982; dePolo, 1989; Berry, 1990; Beanland and Clark, 1994; Pinter and Keller, 1995; Pinter, 1995; Lee et al., 2001a; Bacon et al., 2003), structural evolution (Bateman, 1965; Bachman, 1978; Gillespie, 1991; Hollet et al., 1991), and the relation of deformation within the valley to the regional deformation field of the ECSZ (Reheis and Dixon, 1996; Dixon et al, 1999, 2000; Lee et al. 2001a). Despite these focused efforts, however, several gaps remain in our understanding of this area. In particular, the relationship between normal faulting and through-going dextral shear remains unclear. The structure of Owens Valley is defined primarily by crustal scale range-front normal faulting; however, a significant component of dextral shear is presently accommodated within the graben floor on the Owens Valley and White Mountains fault zones (Figure 2-2; Chapter 2). Typical extensional basin models, which simply invoke large normal displacements on graben-bounding faults do not adequately describe the complexity associated with the predominantly dextral component of deformation within Owens Valley.

Questions pertaining to the structural evolution of valley exist as well. Notably, the western margin of northern Owens Valley is defined by an enigmatic topographical feature, known locally as the Coyote Warp (Figure 4-1; Chapter 4), which clearly constitutes part of, yet displays none of the structural characteristics of the greater Sierra Nevada escarpment. Previous interpretations fail to fully explain its origin. Moreover, the general characterization of faulting in northern Owens Valley, in terms of fault size, slip rate, slip orientation, offset, and age of initiation is incomplete, leaving questions concerning the role of this faulting in the context of the regional deformation field. In particular, knowledge of the temporal variation of slip rates, vital to understanding kinematic evolution, remains limited.

In a more general sense, the evolution of fault populations, in terms of fault growth and interaction, has garnered much attention in recent years, and has greatly increased our understanding of the mechanisms and manifestation of crustal deformation. Each dataset, however, comes with its own set of variables, and thus provides new and intriguing insights into the varied aspects of fault growth and evolution. Several geomorphic features within northern Owens Valley and surrounding areas capture distinct populations of faults, which may be used to gain insight into how fault populations evolve in a given tectonic and geologic setting.

This work consists of five subsequent chapters, which together are designed to broadly characterize deformation within northern Owens Valley, and to derive a structural and kinematic history compatible with observations of regional deformation. Three of these chapters (Chapters Three, Four, and Five) are written as stand-alone research contributions, which address several aspects of tectonism and deformation

within northern Owens Valley.

Chapter Two provides a description of previous work, as well as a description of the basic geologic framework of the study area. It serves as both a literature review and a presentation of pertinent observations made throughout the course of this study. Several regionally significant geologic features, including the ECSZ and its constituent dextral shear zones, the Sierra Nevada Mountains, and Owens Valley, as well as numerous features local to northern Owens Valley, including faults, alluvial fans, and terraces surfaces are described here. This chapter also summarizes the established glacial chronology for the Sierra Nevada, as knowledge of the timing and magnitude of past glaciations provides a primary means to characterize the relative rates of deformation here.

Chapter Three examines the structural evolution of northern Owens Valley through the application of a model of conjugate fault geometry. This model utilizes fault geometry, in terms of fault dip and fault spacing, in order to make predictions concerning fault intersection at depth. In the context of an inferred seismogenic thickness, these predictions have implications for basin development and range-front fault activity. In order to substantiate the interpretations drawn from these predictions, observations of Late Pleistocene deformation associated with range-front fault activity in northern Owens Valley are also presented and discussed. Furthermore, this chapter explores the relationship between normal faulting associated with the Sierran range-front and dextral shear associated with the nearby Owens Valley fault zone.

Chapter Four explores changes in the rate of east-west extension with northern Owens Valley since Middle Pleistocene time. This examination is based on elevation

profiles from several distinct geomorphic markers that each preserve extensive normal faulting related to the same extensional event. The observed deformation associated with each of these surfaces is combined with inferred surface abandonment ages in order to derive extensional slip rates over several time intervals from Middle to Late Pleistocene time. Furthermore, these results are combined with those of previous studies in order to derive a geologically based budget for extension within this part of the ECSZ, which is then compared with extension estimates based on geodetic techniques. The data presented here reduces the existing gaps in our understanding of the ECSZ, and provides new constraints for models concerning its past and present kinematic framework.

Chapter Five presents an analysis of fault population length-frequency data in order to examine the mechanisms of strain distribution within the ECSZ. Specifically, this chapter examines the relationship between observed regional-scale fault spacing and the range of fault sizes exhibited by several northeast-striking fault populations within the ECSZ. Furthermore, this chapter examines the size distributions characterizing three fault subsets, which are constituents of a single large population of normal faults within northern Owens Valley. These fault subsets, which are differentiated based on the inferred ages of the geomorphic surfaces in which they outcrop, each display unique size distributions that can be attributed to specific mechanisms that influence fault development.

Chapter Six summarizes the pertinent findings from each of the preceding chapters, and provides a synthesis of the overall contribution of this work towards a greater understanding of northern Owens Valley and relation to the greater ECSZ.

.

Chapter 2

Context and Overview

Introduction

The primary purpose of this chapter is to provide the contextual and descriptive geologic framework from which successive chapters are developed. Here I present a broad range of geologic observations and characterizations, both old and new, which have guided subsequent interpretations of tectonic and geomorphic development within the field area of northern Owens Valley, California. In this regard, the following serves as both a review of previous literature, and a contribution of original observations and interpretations. Because each of the successive chapters (Chapters Three, Four, and Five) are designed as stand-alone research contributions, each with their own pertinent geologic introductions and settings, this chapter provides brief introductory characterizations of major geologic structures, as well as descriptions of other important features within and around the field area.

One of the necessary goals in undertaking this project was a broad characterization of deformation, which within the field is predominated by faulting, with lesser occurrences of tilting and warping. To that end, a comprehensive fault map was compiled for the study area that includes known faults collated from several sources, as well as numerous previously unmapped faults. The compiled fault map was used as a guide for kinematic interpretation, as well as subsequent field surveys of fault length

and displacement.

The geometry and dimensions of faults provide an important means for characterizing deformation within tectonically active areas. As such, this chapter provides several brief descriptions of individual faults deemed of great importance to the overall interpretations and conclusions of this project. Several geomorphic observations aiding in tectonic interpretation are presented here including descriptions of fluvial and alluvial features, as well as inferences regarding their relationship to tectonic and climatic processes. Furthermore, this chapter provides a brief discussion of each of the methods of study used during the course of this project.

Lastly, a brief general summary of the Late Pleistocene climate history of the Sierra Nevada and surrounding area is discussed here in an attempt to place several of the climatically related geomorphic features, such as alluvial fan and terrace deposits, within a temporal frame of reference. Such a reference frame is useful for inferring changes in the magnitude of deformation through time that are recorded in these surfaces, and thus provides valuable constraints for interpreting kinematic evolution.

Geologic Setting

Owens Valley is situated near the southwestern margin of the continental United States (Figure 2-1A). This region is characterized as a broad zone of distributed crustal shear that has arisen from the northward motion of the Pacific plate in relation to the North American plate. While much of the relative motion between these plates is concentrated along the San Andreas fault system, a significant portion of the resulting dextral shear is transferred east of the Sierra Nevada Mountains where it is distributed on several large right-lateral strike-slip fault zones (Figure 2-1B). Owens Valley and the
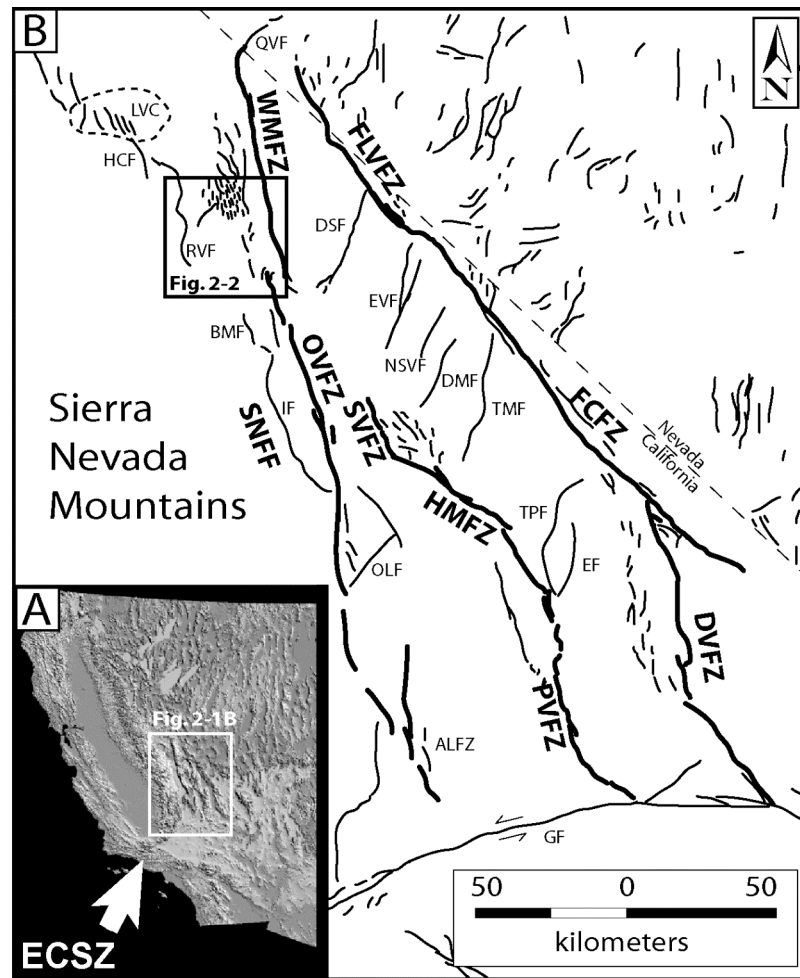
Figure 2-1. A) Regional location map of the Eastern California Shear Zone (ECSZ). **B)** The ECSZ is comprised of several large north-northwest trending dextral shear fault systems that accommodate plate motion east of the Sierra Nevada Mountains. Heavy lines denote dextral fault systems. Inset illustrates location of Figure 2-2. SNFF – Sierran Nevada Frontal Fault system; OVFZ – Owens Valley fault zone; WMFZ – White Mountain fault zone; SVFZ – Saline Valley fault zone; HMFZ – Hunter Mountain fault zone; PVFZ – Panamint Valley fault zone; FLVFZ – Fish Lake Valley fault zone; FCFZ – Furnace Creek fault zone; DVFZ – Death Valley fault zone; HCF – Hilton Creek fault; RVF – Round Valley fault; DSF – Deep Springs fault; EVF – Eureka Valley fault; NSVF – North Saline Valley fault; DMF – Dry Mountain fault; TMF – Tin Mountain fault; TPF – Towne Pass fault; EF – Emigrant fault; IF – Independence fault; BMF – Birch Mountain fault; QVF – Queen Valley fault; OLF – Owens Lake fault; LVC – Long Valley Caldera; RVF – Round Valley fault; GF – Garlock fault.

Sierra Nevada Mountains define the western margin of this zone of intra-continental shear.

Sierra Nevada Mountains

The development of the Sierra Nevada Mountains has provided significant structural control for the development of Owens Valley. The Sierra Nevada Mountains form a continuous north-northwest trending range that extends along much of the length of east-central California. The range is characterized by a gently west-dipping western margin, which grades from the granodioritic basement rocks of the high Sierran peaks to the progressively tilted Eocene-Pleistocene sedimentary and volcanic strata of the Sierran foothills and the San Joaquin Valley (Bateman, 1965; Unruh, 1991; Chamberlain and Poage, 2000). The eastern margin of the Sierra Nevada Mountains is characterized by a steep escarpment that is bounded by a discontinuous array of large north-northwest-striking normal faults, which mark the structural boundary with Owens Valley. The southern-most portion of the Sierra Nevada escarpment extends for over 100 km as an unbroken mountain front from the Garlock fault, north to the town of Bishop, California (Figure 2-1B). This relatively linear section of range-front is disrupted in the vicinity of Bishop by a series of en echelon west-stepping normal faults, which redirect the Sierran mountain front to a more northwesterly trend for the remainder of its northward extent (e.g. Jennings, 1994).

The uplift and formation of the modern-day Sierra Nevada Mountains began during the late Cenozoic (Bateman, 1965; Bachman, 1978; Unruh, 1991; Small and Anderson, 1995). Stratigraphic evidence from the San Joaquin Valley indicates that tilting and uplift of the Sierra Nevada block began around ~5 Ma (Unruh, 1991).

Because faulting along the eastern escarpment likely initiated as a result of such tilting, this age estimate provides a maximum limiting age for the formation of the Sierra Nevada Mountains. Indeed, estimates of orogen initiation based on evidence from the eastern margin of the Sierra Nevada indicate the present range began forming at least since Pliocene time (Bateman, 1965; Bachman, 1978; Stockli et al., 2003).

The tectonic history of the Sierra Nevada escarpment and surrounding region has been heavily influenced by the dynamics of the Pacific-North American plate boundary. Extensional faulting within eastern California likely initiated during the Middle Miocene, as suggested by inferences concerning the exhumation and tilting of the White-Inyo Mountains at ~12 ma (Stockli et al., 2003). This early bout of extension in eastern California subsequently evolved into predominately dextral shear beginning as early as ~10 Ma (e.g. Dokka and Travis, 1990) in the Mojave Desert region to as recently as ~3 Ma in Owens Valley (Reheis and Sawyer, 1997; Stockli et al., 2003). The marked change in deformational style (i.e. extension to dextral) is attributed to the Early to Middle Miocene evolution of the North American-Pacific plate boundary from a subduction boundary to the present transform boundary (Atwater, 1970; Atwater and Stock 1998).

The Eastern California Shear Zone

The zone of distributed dextral shear located south and east of the Sierra Nevada Mountains was initially termed the Eastern California Shear Zone (ECSZ) by Dokka and Travis (1990) who first recognized the importance of this region as a significant structural pathway for plate boundary-related shear (Figure 2-1B). Their estimate of ~10 to 6 Ma for the initiation of dextral slip in the southern portion of the ECSZ implies this

region has accommodated ~9-23% of the relative North American-Pacific plate motion since its inception. These early observations were based primarily on geological data, and were later confirmed by Savage et al. (1990) through the use of geodetic measuring techniques. Furthermore, Savage et al. (1990) found evidence that dextral shear extends northward beyond the Mojave Desert region into Owens Valley. Subsequent findings from a broad range of geologic and geodetic studies have since reaffirmed and expanded upon these initial interpretations (Table 2-1). The term ECSZ presently applies to a broad swath of eastern California from the Mojave Desert in the south, to approximately the northern margin of the White Mountains, near the latitude of Long Valley Caldera.

The ECSZ is characterized as a zone of regionally diffuse right-lateral shear located between the relatively aseismic Sierra Nevada block, and the western margin of the Basin and Range province of Nevada (e.g. Dixon et al. 2000). The ECSZ is separated into two broad structural and kinematic domains by the left-lateral Garlock fault (Figure 2-1B). Geodetic data indicate present-day crustal strain accumulation is continuous within a north-trending zone extending across the Garlock fault (e.g. Miller et al., 2001; Peltzer et al. 2001); however, a firm structural connection between these two domains has yet to be adequately established. South of the Garlock fault, shear is accommodated on an array of discontinuous right-lateral faults developed as a result of clockwise rotation of discrete crustal blocks within the Mojave Desert (Dokka and Travis, 1990; Golombek and Brown, 1988; Miller et al., 2001). North of the Garlock fault, shear is distributed on three main interconnected fault zones: the Death Valley-Furnace Creek-Fish Lake Valley, the Hunter Mountain-Panamint Valley-Saline Valley, and the Owens Valley-White Mountain fault zones (Figure 2-1B and Table 2-1). Based on extensive geodetic surveys,

TABLE 2-1. SUMMARY OF GEODETIC AND GEOLOGIC DEXTRAL SLIP RATES WITHIN THE ECSZ

	SN - NA	ECSZ	orientation	OVFZ	DV-FCFZ	PV-HM-SVFZ	FLVFZ	WMFZ
Geodetic Rates (mm/yr)								
Savage (1990)	8.2 ± 0.4	8.2 ± 0.4	N34^{o}W					
Argus/Gordon(1991)	11 ± 1		N28^{o}W ± 3°					
Sauber et al. (1994)		12 ± 2 (Mojave)	N39^{o}W ± 5°					
Savage and Lisowski (1995)				2.9 ± 0.4				
				7 (ehs model)				
Dixon et al. (1995)	12.1 ± 1.2	10.7 ± 1.6	N38^{o}W ± 5°	3.9 ± 1.1	3.3 ± 2.2		6.2 ± 2.3	3.4 ± 1.2
Bennett et al. (1997)					5 ± 1 (DV + HM)			
Bennett et al. (1999)	11 - 13		N20^o-40°W					
Thatcher et al. (1999)	8-12		N50^{o}W					
Gan et al. (2000)			N23^{o}W	6.9 ± 1.6	3.2 ± 0.9	3.3 ± 1.6		
Dixon et al. (2000)	1.8 ± 1.4 (ext.)	11.4 ± 1.1		3 ± 2 (vec model)			8.2 ± 2	
				7 ± 2 (ehs model)				
Miller et al. (2001)		13		7 (ehs model)	6 (DV-PV)			
		14 (Mojave)						
McClusky et al. (2001)		11 ± 2 (Mojave)		5.6 ± 0.6 (N site)	2.8 ± 0.5 (DV)	2.5 ± 0.8 (PV)	5.8 ± 0.4	
				4.6 ± 0.5 (S site)	2.7 ± 0.6	3.2 ± 1.0 (HM)		
						2.7 ± 1.9 (SV)		
Peltzer et al. (2001)		7 ± 3						
Oldow et al. (2001, 2003)	14-15							
Dixon et al. (2003)				2.1 ± 0.7 (e-v model)	8.3 ± 1.2	2.4		
Geologic Rates (mm/yr)								
Hamilton and Meyers (1966)					3 (DV; 3-5 Ma)			
Burchfiel et al. (1987)						2-3 (4 Ma)		
Lubetkin and Clark (1988)				0.7-2.2				
dePolo (1989)								0.5 - 1.2 (Holo)
Zhang et al. (1990)						2.4 ± 8 (PV; Holo)		
Dokka and Travis (1990)		6-12 (Mojave; 10-6 Ma)						
Beanland and Clark (1994)			N20^{o}W	2.0 ± 0.5 (Holo)				
Pinter (1995)								
Reheis and Sawyer (1997)							3-12 (10 Ma)	
							6 (late-Miocene)	
							3 (early-Pleist)	
							11 (mid-Pleist)	
							4 (late-Pleist)	
Lee et al. (2001a)				1.8 ± 0.3 - 3.6 ± 0.2 (Holo)				
Kirby et al. (2006)								0.7-0.8 (mid-Pleist)
								0.3-0.4 (late-Pleist)

Unless otherwise noted (i.e. Mojave), dextral slip rates for the ECSZ refer to rates derived north of the Garlock Fault
vec - visco-elastic coupling; ehs - elastic half-space; e-v - elastic-viscoelatic coupling
SN-NA - Sierra Nevada-North America; ECSZ - Eastern California Shear Zone; OVFZ - Owens Valley fault zone; DV-FCFZ - Death Valley-Furnace Creek fault zone;
PV-HM-SVFZ - Panamnit Valley-Humter Mountain-SalineValley fault zone; FLVFZ - Fish Lake Valley fault zone; WMFZ - White Mountains fault zone

it is suggested that these fault zones collectively accommodate ~10-13 mm/yr, or 25-30%, of the relative Pacific-North American plate motion (e.g. Dixon et al., 1995, 2000; Miller et al., 20001; McClusky et al., 2001). Furthermore, observed geologic deformation within the ECSZ is broadly consistent with dextral strike-slip faulting (e.g. Dokka and Travis, 1990; Butler et al., 1988; dePolo, 1989; Beanland and Clark, 1994; Reheis and Sawyer, 1997, Lubetkin and Clark, 1988; Lee et al., 2001a; Bacon et al., 2003).

The prevailing kinematic model for the ECSZ, first proposed by Dixon et al. (1995), suggests that dextral slip within this region is transferred between the discrete zones of shear through extensional right-steps, which appear as large (>20 km along strike) northeast-striking normal faults. These faults include the Queen Valley (QVF), Deep Springs (DSF), Dry Mountain (DMF), Tin Mountain (TMF), and Towne Pass (TPF) faults (Figure 2-1B). Several researchers have subsequently demonstrated structural interconnectivity between these two distinct (dextral and normal), yet genetically related fault populations (Burchfiel et al., 1987; Reheis and Dixon, 1996; Reheis and Sawyer, 1997; Lee et al., 2001b; Oswald and Wesnousky, 2002).

Owens Valley

Owens Valley is a normal fault-bounded graben situated between the Sierra Nevada and White-Inyo Mountains. It extends as a nearly linear depression from the Garlock fault north to Long Valley Caldera (Figure 2-1B). Normal fault activity along both the Sierra Nevada and the White-Inyo Mountain range-fronts has resulted in relief of up to 3,000 m between the basin floor and mountain crest. Such relief has in turn provided the gravitational potential to drive erosion and transport of material from the
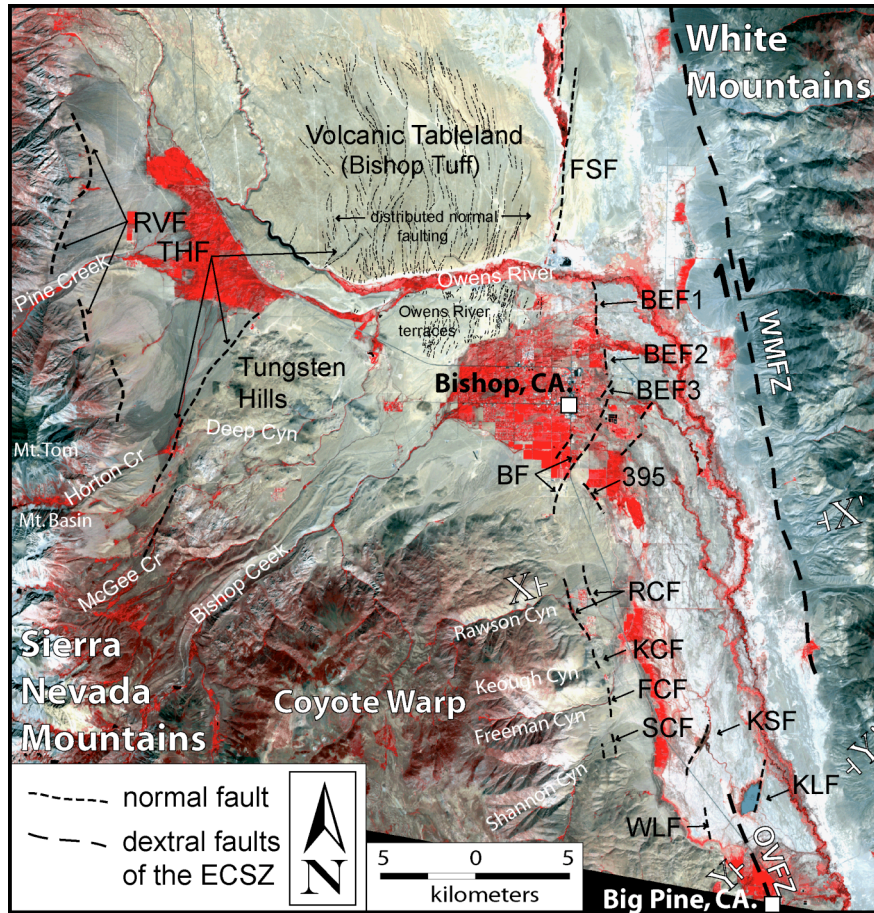
Figure 2-2. Infrared satellite image of northern Owens Valley indicates vegetation cover in red. Normal faults (small dashed lines) are often apparent from sharp vegetation divides. With the exclusion of the RVF and some faults on the Volcanic Tableland, all normal faults dip west. Dextral faults (thick dashed lines) in the field area accommodate right-lateral slip on localized on two discrete shear zones: OVFZ and WMFZ. Section lines X-X' and Y-Y' denote location of gravity profiles in Figure 2-3. 395 – 395 fault; BEF1-3 – Bishop East faults 1 though 3; BF – Bishop fault; FCF – Freeman Canyon fault; FSF – Fish Springs fault; KLF – Klondike Lake fault; KSP – Klondike Spring fault; OVFZ – Owens Valley fault zone; RCF – Rawson Canyon fault; RVF – Round Valley fault; THF – Tungsten Hills fault; SCF – Shannon Canyon fault; WLF – Warren Lake fault; WMFZ – White Mountains fault zone.

range to the basin. Such material provides the primary template for recording much of the Late Pleistocene deformation discussed here.

The opposing forces of tectonic uplift and erosion, punctuated with pulses of volcanic outpouring, have provided Owens Valley with a unique and varied geology. The predominantly granodioritic bedrock peaks of the Sierra Nevada give way to the broad expanse of the alluviated valley floor. Alluvial fans within the valley are ubiquitous as they issue from each of the mountain catchments draining to the valley. Moreover, glacial advances throughout the Late Pleistocene have emplaced several generations of moraine deposits, which in some instances extend up to ~5 km from the range-front. Infilling of the greater Owens basin is attributed to a combination of fluvial, pluvial and debris flow processes which have contributed great thicknesses of alternating fine to coarse sedimentary sequences to the basin (Bateman, 1965; Bachman, 1978; Hollet et al., 1991). Furthermore, several episodes of volcanism, including eruption of the Bishop Tuff as well as basaltic cinder cones and flows, cover large portions of the valley.

Much of the underlying basement of northern Owens Valley is obscured by Late Pleistocene alluvium; however, several geological and geophysical techniques have been used to make inferences regarding its subsurface structure. Geologic data from the eastern side of the valley indicate as much as 2,300 m of vertical offset between the Owens Valley basement and the nearby White-Inyo Mountains (Bachman, 1978). There is further indication that the depth of the basin varies significantly along-strike. Gravity data obtained south of the town of Big Pine, California, reveals the presence of an intra-basin high that splits the larger Owens basin into two sub-basins (Bateman, 1965; Hollett

et al., 1991). Such marked fluctuations in basin depth typically result from along-strike

variations in accumulated normal displacement on the graben-bounding faults, with basin

highs corresponding to fault tip and relay zone regions (Anders and Schlische, 1994).

While much of the variability in along-strike basin structure in Owens Valley may be

attributed to differential activity on the basin bounding normal faults, the basin high

observed south of Big Pine corresponds to a surficial exposure of deformed granodioritic

and Paleozoic meta-sedimentary basement rock, which reflects an en echelon

compressive left step of the Owens Valley fault zone (Taylor, 2002).

The subsurface structure of the northern sub-basin, centered between the towns of

Bishop and Big Pine, resembles that of an east-tilted graben, which presumably formed

through slip on the bounding faults to the east and west (Figure 2-2 and 2-3). The

western margin of the graben corresponds to a distinct portion of the Sierran range

termed the Coyote Warp. Along the Coyote Warp the large range-front elevations and

variable topography, characteristic to the south and north, give way to a broad elevated

surface with internally low relief (Figure 2-2). This surface is mantled by a veneer of

Quaternary alluvium and glacial tills, which overlie quartz monzanitic and granodioritic

basement. Based on the combination of low topography and extensive sediment cover,

this area is inferred to represent a Middle to Late Pliocene erosional surface (Bateman,

1965). The Coyote Warp was originally described by Taylor (1933) as a *scarpramp*,

whereby the Sierran range-front faults to the south and north die out towards each other

along their overlapping tips; thus forming a broad, gently sloping surface. Bateman

(1965) suggested that the development of the Coyote Warp resulted from a broad

warping of the Sierran range-front. Pinter (1995) slightly modified this interpretation,
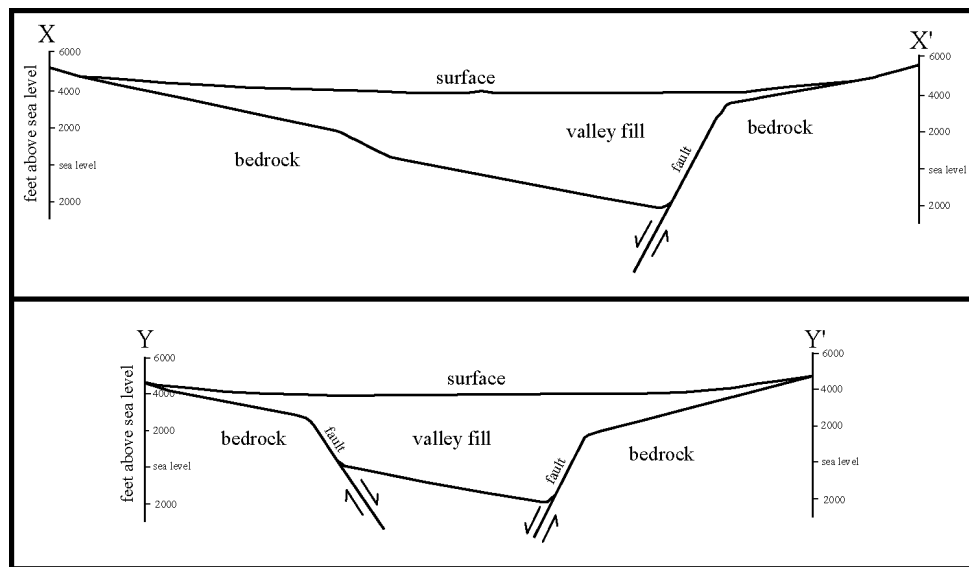
Figure 2-3. Interpretations of northern Owens Valley subsurface structure based on seismic data (modified from Bateman, 1965). See Figure 2-2 for location of X-X' and Y-Y'. Profiles reflect the asymmetric nature of the basin structure of northern Owens Valley.

suggesting that the anticlinal nature of Coyote Warp formed as a result of differential rotations of the Sierra Nevada block and Owens Valley basement.

Sierra Nevada Frontal Fault System

The Sierra Nevada Frontal Fault (SNFF) system is a relatively linear, north trending zone of discontinuous normal fault segments that define the eastern margin of the greater Sierra Nevada escarpment (Figure 2-1B). The SNFF system extends along the length of the Sierra Nevada Mountain front from the Garlock fault to Long Valley Caldera, and is largely responsible for the considerable relief associated with Owens Valley. Recent activity along the SNFF system is documented on several Late Pleistocene and Holocene normal fault segments, including the Independence fault (IF), the Birch Mountain fault (BMF), the Round Valley fault (RVF), the Hilton Creek fault (HCF), and several other small, unnamed fault segments (Figure 2-1B) (Bateman, 1965; Gillespie, 1982; Bryant, 1984; Berry, 1990, 1997). Slip rates for the southern and central portions of the range-front are poorly known, except for a few locations. Inferred Late Pleistocene slip rates range from <0.5 mm/yr for the IF (Gillespie, 1982), to ~0.4-0.6 mm/yr for faulting near the mouth of nearby Onion Valley (Le et. al., 2005). Slip rates for the northern portion of the SNFF system, including the RVF and the HCF, are better constrained, as these faults, and the fan and moraine features they displace, have been subject to several in-depth mapping and analytical campaigns (Bateman, 1965; Bryant, 1984; Berry, 1990, 1994, 1997).

The RVF is the primary locus for extensional accommodation along the western margin of northern Owens Valley (Figure 2-2). It consists of a series of discontinuous east-dipping normal fault scarps that outcrop along the base of the Sierran escarpment in

the vicinity of Mt. Humphreys, Basin Mountain, Mt. Tom, and the Wheeler Crest. The

RVF terminates near the northern portion of Round Valley where range-front faulting

steps north and west to the HCF. The Late Pleistocene vertical slip rate of the RVF,

estimated from offset alluvial fans and glacial moraines, is ~0.4-1.0 mm/yr (Berry, 1997).

The HCF exhibits a Late Pleistocene rate of ~0.9-1.3 mm/yr (Berry, 1997). The higher

slip rate inferred for the HCF is due likely to a local zone of crustal weakness associated

with the resurgent dome of Long Valley Caldera (Gillespie, 1991; Sharp and Glazner,

1997).

The Owens Valley Fault Zone

The Owens Valley Fault Zone (OVFZ) is the westernmost dextral shear fault zone

of the ECSZ. It extends roughly 110 km from Owens Lake to just north of the town of

Big Pine, where right-lateral displacement dies out via a series of northeast-striking

horsetail splays (Figure 2-1B and 2-2). The OVFZ has an average strike of N20^{o}W,

slightly more northerly than the orientation of the inferred regional shear orientation, and

an average dip of 80° ± 15° ENE (Beanland and Clark, 1994). The sense of slip observed

along the length of the fault zone is largely consistent with right lateral displacement,

with a lesser component of normal offset. Faulting is primarily evident from surface

lineaments, groundwater barriers, scarps, depressions, and pressure ridges (Beanland and

Clark, 1994).

Active seismicity along the OVFZ is documented through historical report and

paleoseismic investigation. Historical seismicity is evidenced by the 1872, Owens Valley

earthquake, which ruptured the entire length of the fault zone in a M_w 7.5-7.7 event

(Beanland and Clark, 1994). The average right-lateral component of offset is estimated

to be 6 ± 2 m, with a maximum of 10 m near the town of Lone Pine, California, which is located ~100 km south of Bishop. The overall right-lateral to normal offset ratio is 6:1. The average inferred Holocene slip rate for the fault zone is 1.5 ± 1 mm/yr, however several sites yield a rate closer to 2 ± 1 mm/yr (Beanland and Clark, 1994). Lubetkin and Clark (1988) presented a similar rate of 0.7-2.2 mm/yr, which takes into account dextral slip on the OVFZ, as well as a subsidiary fault strand known as the Lone Pine fault.

Paleoseismic investigation has uncovered evidence for at least one, and possibly two, pre-1872, Holocene rupture events. Rupture events are documented at ~3.3-3.8 ka (Lee et al., 2001a) and 8.9-9.5 ka (Bacon et al., 2003), yielding slip rates of ~1.8-3.6 mm/yr and 1.0-1.6 mm/yr, respectively. Furthermore, published estimates for the recurrence interval for large earthquakes along the OVFZ of 3.5-5 ka (Beanland and Clark, 1994), 3-4.1 ka (Lee et al., 2001a), and 5-10.5 ka (Lubetkin and Clark, 1988) are in relative agreement.

Several ground and space-based geodetic studies indicate that the OVFZ is a primary locus of dextral shear within the ECSZ (Table 2-1). Savage and Lisowski (1995), using trilateration data, determined a dextral slip rate of 2.9 ± 0.4 mm/yr, with a valley-perpendicular extensional component of 1.0 ± 0.3 mm/yr. Depending on the geodetic model used, however, as much as 7 mm/yr of dextral shear may be presently accommodated within the valley. Dixon et al. (1995) presented GPS data suggesting that 3.9 ± 1.1 mm/yr of dextral slip is presently accommodated on the OVFZ. Dixon et al. (2000) further revised this rate to 3.0 ± 2.0 mm/yr. Gan et al. (2000), also using GPS data, determined a rate of dextral slip of 6.9 mm/yr for the southern portion of the OVFZ, and Miller et al. (2001) found a similar rate of 7 mm/yr. McClusky et al. (2001)

suggested that nearly half of the shear assigned to the ECSZ is accommodated along the Airport Lake fault zone (5.3 ± 0.7 mm/yr), located near the Garlock fault, and the southern (5.0 ± 0.6 mm/yr) and central (4.6 ± 0.5 mm/yr) portions of the OVFZ. Furthermore, McClusky et al. (2001) presented rates of extension for sites along the southern and central portions of the OVFZ of 2.7± 0.6 mm/yr and 1.9±0.7 mm/yr respectively.

The White Mountains Fault Zone

The White Mountains faults zone (WMFZ) delineates the western margin of the White Mountains, the westernmost range of the Basin and Range province (Figure 2-1B). It extends ~115 km from the Waucoba Embayment, which is located adjacent to the northern tip of the OVFZ, to the northern end of the White Mountains, where it curves abruptly eastward and merges with the northeast-trending Queen Valley fault, which bounds a small extensional basin. The WMFZ is largely characterized as a right-oblique fault system exhibiting both dextral and normal slip (dePolo, 1989; Kirby et al., 2006). Distinct kinematic indicators (dip-slip striations overprinted with right-lateral slickensides) (Stockli et al., 2003), as well as laterally offset geomorphic features (dePolo, 1989; Kirby et al., 2006) suggest that dextral slip is currently dominant. Dextral shear is transferred north and eastward from the OVFZ to both the WMFZ, via several northeast-striking intra-valley normal faults, and the Fish Lake Valley fault zone (FLVFZ), via the Deep Springs fault (Figure 2-1). Holocene activity along much of the fault zone is inferred from its youthful geomorphology and the young age of displaced deposits (dePolo, 1989), however, Late Pleistocene activity is better constrained (Kirby et al., 2006).

The tectonic history of the WMFZ began ~12 Ma with the exhumation, extensional break-up, and subsequent eastward tilting of the White Mountains block. Extension during this early phase resulted in the accumulation of up to ~8 km of dip-slip movement along the WMFZ (Stockli et al., 2003). Dextral shear in the area first initiated along the eastern margin of the White Mountains on the FLVFZ at ~6 Ma (Reheis and Sawyer, 1997), and later migrated, at ~3 Ma, to the WMFZ where the pre-existing normal fault planes were reactivated by right-lateral slip (Stockli et al., 2003).

Geomorphic Markers in Northern Owens Valley

Exposures of faulting within northern Owens Valley are largely confined to the existing bedrock overburden, which consists of alluvial fan surfaces, river terrace deposits, glacial moraines, river plain deposits, and extrusive volcanic units. These deposits are the primary geomorphic markers used here to infer the rate and magnitude of recent deformation within the field area.

The primary indicators for active range-front faulting within the valley are discrete vertical displacements evident within the numerous alluvial fan and glacial moraine surfaces that are associated with the drainage catchments of the Sierran range-front (Figure 2-2). The largest of these catchments, Big Pine Creek, Bishop Creek, and Pine Creek, are interspersed with several lesser-sized drainages, each with their own contribution to the alluvial apron. Alluvial fans ubiquitously line the valley, and are clearly distinguishable both in the field, and on aerial photographs. Much of the variability between these deposits lies in the relative appearance of their upper surfaces.

Alluvial fan deposits are the predominant geomorphic marker found along the eastern margin of the Coyote Warp (Figure 2-2). Several generations of progradational

alluvial fan units within this area record vertical fault displacements within their upper surfaces. The most extensive fan units extend from the three main active catchments in this area, including Rawson Canyon, Freeman Canyon, and Shannon Canyon. These primary fan surfaces, as well as other small intervening fan units, are host to a series of discontinuous north-striking normal faults, which dip west towards the range-front.

Fluvial terrace deposits within Owens Valley provide a further means for measuring deformation within northern Owens Valley. Several alternating episodes of aggradation and incision throughout the Late Pleistocene have resulted in the preservation of a series of fluvial terrace surfaces (Figure 2-2). In all, four terrace surfaces, designated Qt1 through Qt4 from youngest to oldest, are tentatively correlated with several Late Pleistocene glacial events as defined in the Sierran Nevada glacial chronology (Table 4-2; Chapter 4) (Pinter et al., 1994). Each of these terrace surfaces records a discrete interval of accumulated fault displacement, thus making it possible to measure, and to furthermore compare deformation rates over different intervals of geologic time. A comparison of these rates provides the primary basis for Chapter 4.

Sierra Nevada Glacial Chronology

The geomorphology of tectonically driven landscapes is often heavily influenced by climate. Climatic events and fluctuations provide controls for the redistribution of clastic material eroded from the active mountain-front to the valley, where in the case of northern Owens Valley, much of the observed tectonic deformation is preserved. Because the alluvial landscape here provides a primary means for interpreting deformation, it is critical to relate the timing and magnitude of past climatic processes to the formation of the landscape. Thus, establishment of a reliable glacial chronology is

key to determining the ages and slip rates of faults within the area. The following provides a review of glacial age constraints derived from various sources in the greater Owens Valley.

Several varied techniques have been applied to unravel the glacial history of the Sierra Nevada. Initial efforts relied primarily on the use of relative dating techniques. Such methods typically qualify weathering character (i.e. clast-sound velocity, moraine morphology, boulder surface appearance) and soil development profiles of moraines (e.g. Birkeland et al, 1991; Bursik and Gillespie, 1993; Berry, 1994). Relative dating techniques have proved useful for establishing the temporal relationship between past glaciations, however, the usefulness of the record in constraining fault activity has been limited due both to the discontinuity of glacial sequences between drainages (i.e. not all glaciations are recorded in each drainage), and to the lack on numerical ages for these glaciations.

Blackwelder (1931) first defined the Sierra Nevada glacial chronology with four distinct glacial events termed, from youngest to oldest, Tioga, Tahoe, Sherwin, and McGee. Subsequent revisions added minor glaciations including the Tenaya, between the Tioga and Tahoe, and the Mono Basin and Casa Diablo, between the Tahoe and Sherwin glaciation (Sharp and Bierman, 1963). The larger divisions have, to varying degrees, been identified in several drainages located along the eastern margin of the Sierra Nevada. For instance, based on soil and geomorphic analysis, Berry (1994) was able to differentiate between Tioga, Tahoe, and pre-Tahoe in the catchments of Bishop and Pine Creeks, and between only the Tioga and Tahoe at McGee Creek. However, Berry (1994) uncovered no solid evidence for the Tenaya event in any of these drainages.

The Sherwin glaciation is the oldest defined, yet least understood glaciation of the Sierran region. Deposits of Sherwin tills, which underlie the well-dated Bishop Tuff (Bateman, 1965), have only a minimum limiting age of ~760 ka (Izett and Obradovich, 1994; Sarna-Wojcicki, 2000). The pre-Tahoe glaciation (evident in the Mono Basin, north of Long Valley Caldera) is bracketed between 133-218 ka by Phillips et al. (1990) (Table 4-2; Chapter 4). This age estimate, based on cosmogenic ^{36}Cl accumulation in moraine boulders, corroborates Gillespie (1988) who, based on a dated basalt flow, derived an age of >133 ± 10 ka. The Tahoe glaciation is bracketed to between 55.9 and 65.8 ka (Phillips et al., 1990). This age range is in relative agreement with a dramatic increase in rock flour evident in Owens Lake core, which occurred between 68.1 and 78.0 ka (Bischoff and Cummins, 2001). James et al. (2002), using cosmogenic ^{10}Be, similarly provided evidence for significant glaciation within the northwestern Sierra Nevada at 76.4 ka. Phillips et al., (1990) provided a limiting age for the Tioga glaciation between 20.4 and 23.1 ka. Based on a range of subsequent studies, the Tioga glaciation lies broadly in the range of 15 and 25 ka (Table 4-2; Chapter 4).

Methods of Study

A broad range of measuring and analytical techniques was utilized in the completion of this project. Several of these techniques are presented and described here, including, for each of the methods used, the analytical basis, its application, and its limitations.

Geological Techniques

Basic geological mapping was conducted in the field at a scale of 1:24,000 and 1:62,500, and through examination of U.S. Geological Survey (USGS) National Aerial

Photography Program (NAPP) photographs (1:40,000), and one-meter cell resolution USGS digital orthophoto quadrangles (DOQQ). Mapping primarily involved estimation of surficial fault traces from visible scarps, and delineation of alluvial fan and fluvial terrace surfaces. Alluvial fan surfaces were identified and differentiated based primarily on surface color variations, with slope continuity, surface lithology, boulder frequency, and the degree of weathering of exposed boulders also taken into account. Spatially continuous alluvial fan and terrace surfaces with similar character throughout were generally considered to be of the same deposit. Distinct elevation differences between surfaces, notably the terrace surfaces, made local differentiation relatively straightforward (Figure A-6, Appendix A). Furthermore, cross-sections and stratigraphic sections were created for several meter-scale outcrops of fault and fractures planes, as well as prominent sedimentary packages.

Differential Global Positioning System

Fault attribute (length and displacement) surveys were conducted using an Ashtech Differential Global Positioning System (DGPS). DGPS units employ a base station and rover station that each receive the same GPS signal, and thus negate the inherent error associated with standard GPS signal transmission. The utility of such systems lies in their ability to very accurately survey points within a local reference frame. DGPS typically affords decimeter-scale horizontal and vertical accuracy. Survey data obtained using DGPS can later be tied to local benchmarks in order to place the data within a global reference frame.

Measurements of along-strike displacement profiles and cross-strike profiles were obtained for several faults within the field area (Figure 2-2; Appendix A). Along-strike

displacement profiles were obtained from fault surveys by subtracting the corresponding

hangingwall and footwall elevations points measured along the fault scarps. Pairs of

corresponding elevation points each lie on a line perpendicular to fault strike. Cross-

strike profiles were measured along lines perpendicular to fault scarps, typically near the

inferred location of maximum displacement.

Computing Methods

Mapping and survey data were digitally compiled using ArcView 3.2, a GIS

computing tool. DOQQ images and digital elevation models (DEM) were used as base

maps in ArcView. Data processing was performed using standard numerical

manipulation and graphing programs (Excel, Sigma-plot).

Dating Methods

The primary analytical dating technique utilized for this study is optically

stimulated luminescence (OSL). The theory behind, as well as the application of this

dating method is described in Appendix B.

Samples submitted for OSL analysis (Table B-1; Appendix B) were collected in

the field area from four locations, including the Qt2 Owens River terrace surface (Figure

4-1B; Chapter 4), the scarp footwall of a prominent intra-valley normal fault near Bishop

(BEF-1; Figure 2-4), the basal portion of the Qt3 terrace deposit overlying a strath of

Bishop Tuff, and from a site in Deep Canyon just below the contact between the upper

debris flow unit and the lower sand unit (Figure C-2; Appendix C). Samples were

collected by removing, and shielding from light, a portion of relatively fine-grained,

predominantly quartz sediment. The material intended for sample was tightly wrapped

with an opaque covering so as to limit its exposure to light before being sent to the
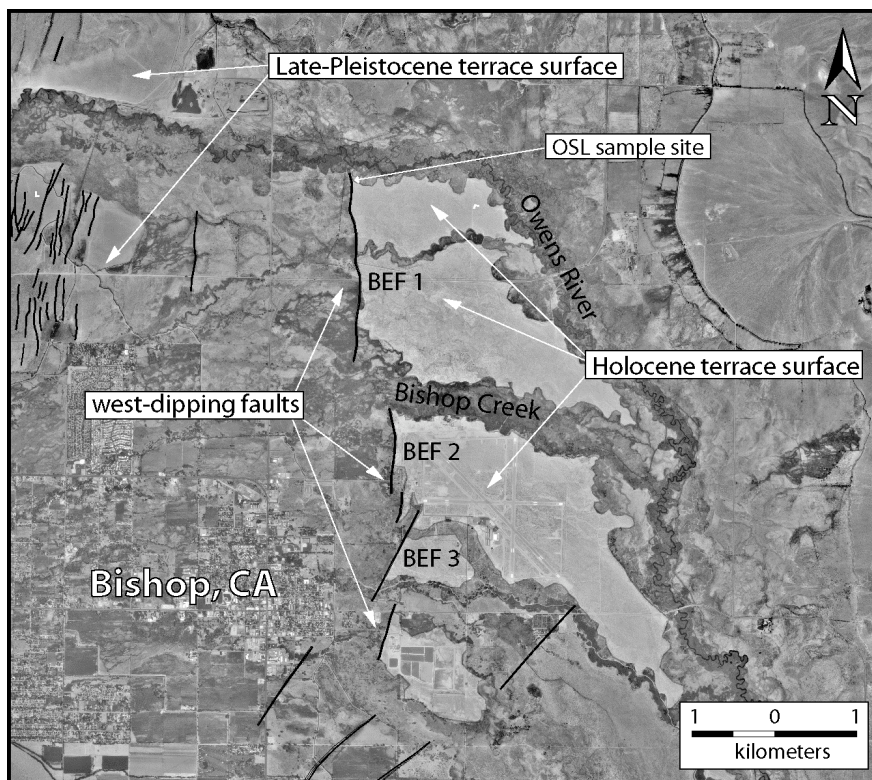
Figure 2-4. Aerial view of the Bishop area faults and displaced Holocene terrace surface illustrates the influence of active faulting on the drainage patterns of the Owens River and Bishop Creek. BEF 1-3 – Bishop East faults 1-3.

analytical lab.

Faulting in Northern Owens Valley

Deformation within northern Owens Valley is largely characterized by normal and dextral faulting. Normal faulting within the valley is much more distributed than dextral faulting, which is localized on the OVFZ and WMFZ. The largest normal faults associated with Owens Valley are those constituting the SNFF system; however, the vast majority of normal faults within the valley are distributed across the central alluvial apron and overlying volcanic units (Figure 2-2). These faults, referred to herein as intra-valley faults, broadly constitute two distinct populations, representative of two distinct styles of deformation presently active in the valley. Given the varied fault populations within northern Owens Valley, useful insights may be drawn into the nature and history of deformation of this area, particularly in terms of style, magnitude, and evolution through time.

Intra-Valley Normal Faulting

Intra-valley normal faults within the field area are separated into two distinct fault populations based on their kinematic role and subsequent geometry. The larger of the two populations consists predominantly of north-striking, variable dip normal faults, which occur almost exclusively within the Mid-Pleistocene Bishop Tuff. Faulting extends southward from the tuff into several nearby Late Pleistocene fluvial terrace units associated with of the Owens River (Figure 2-2 and 4-1B). The faulted terrace surfaces provide a means to characterize both the rate of extension within northern Owens Valley over multiple timescales (Chapter 4), and changes in the patterns of strain distribution through time (Chapter 5).

The second intra-valley fault population consists of a number of northeast-striking, west-dipping normal faults, which are confined to the eastern margin of northern Owens Valley near the overlapping tip region of the OVFZ and WMFZ (Figure 2-2). These faults primarily offset Holocene basin deposits, with some limited exposure in nearby Late Pleistocene alluvial fan deposits. The geometry of these northeast-striking faults is consistent with a kinematic transfer of dextral slip across the right step from the OVFZ to the WMFZ.

The Tungsten Hills Fault

The Tungsten Hills fault (THF) is a large (~14 km in length) northeast-striking fault, which delineates the western margin of a prominent salient of bedrock for which it is named (Figure 2-2). The THF juxtaposes Mesozoic age granodioritic bedrock of the Tungsten Hills footwall block against post-late glacial debris flow and fan units issuing from nearby Sierran drainages. Meandering perennial streams, namely Horton Creek and McGee Creek, have embayed the main body of the Tungsten Hills resulting in an irregular surface trace of the THF. Much of the evidence for the latest interval of activity along the fault has thus been either eroded or buried by recent alluviation. The elevation contrast between the nearby fan surface and several prominent bedrock highs within the Tungsten Hills provides a minimum estimate of ~300 m for cumulative throw on the THF. A well-preserved surface expression of the THF occurs near its northern tip (Figure 2-2), where ~50 m of throw has accumulated since emplacement of the Mid-Pleistocene Bishop Tuff (Appendix A). Based on the age of the Bishop Tuff of ~760 ka (Izett and Obradovich, 1994; van der Bogaard and Schirnick, 1995; Sarna-Wojcicki, 2000), and assuming fault initiation quickly followed tuff emplacement, the THF has an

inferred minimum Mid-Pleistocene slip rate of ~0.06 mm/yr; however this estimate is derived from very near the northern fault tip, and thus is likely not representative of the fault as a whole. Holocene displacement is evident on the THF just south of the VT, where a distinct vegetation divide marks the fault trace; however, due to drainage incision along strike, the surveyed vertical displacement along this section likely does not accurately reflect Holocene offset (Appendix A).

Differential movements along both the THF and the RVF appear to have decoupled the Tungsten Hills block from the adjacent Sierra Nevada Mountains (Figure 2-2). The occurrence of similar bedrock outcrops of distinct meta-sedimentary sequences within both the Tungsten Hills and the adjacent Sierran Nevada (Bateman, 1965) suggests that these nearby locales once comprised a single coherent basement block, and that faulting has since resulted in the formation of a broad graben between the two (Figure 2-2). The graben, which forms the southern portion of Round Valley, provides a primary pathway for drainage within this area. As such, several of the small drainage systems originating from the nearby Sierran escarpment have been influenced by the development of the THF (see Appendix C for discussion). Paleo-drainage patterns and fluvial/alluvial deposits located within and around the Tungsten Hills provide constraints for interpreting the development of the THF.

The Bishop Fault

The Bishop Fault (BF) is the largest (~4 km) of several west-dipping normal faults extending from the northeastern margin of the Coyote Warp (Figure 2-2). The southernmost portion of the BF strikes almost due north, however, overall it has a northeast strike. The BF displaces Late Pleistocene fan deposits and Holocene alluvium

(Bateman, 1965). The fault scarp is visible on air photos and satellite images, where it is clearly recognized by a distinct vegetation divide that separates its footwall and hangingwall (Figure 2-2). Much of the footwall is mantled with sparse gravels and eolian sand, and is largely devoid of vegetation save for scattered sage, whereas the hangingwall supports a variety of lush grasses and trees. The increased vegetation cover on the hangingwall reflects its close proximity to groundwater.

South of the town of Bishop, the Bishop fault (BF) intersects a large excavation pit located within the grounds of the Inyo County Bishop-Sunland Landfill (Figure 2-2). The BF fault was documented in cross-section at a 1 m vertical outcrop located ~20 m below the current fan surface (Figure 2-5; Appendix D). The main fault plane exhibits a dip of 68° towards N65^{o}W, with evidence for two possible rupture events. A cumulative vertical offset (throw) of ~3.2 m was measured on several fracture planes, however because of the limited dimensions of the outcrop, this estimate represents the minimum offset. Much of the throw is derived from correlation of the middle unit with a similar unit located ~17 m to the east (Figure 2-5).

The stratigraphic section cut by the BF is composed of three main units (see Appendix D for discussion). Each unit consists of distinct lithology with internally consistent depositional structures broadly representative of three distinct depositional regimes (Figure 2-5). The exposure shows evidence for offset on two main fault planes, such that from left to right, the stratigraphic units become younger. The three stratigraphic units have been emplaced side-by-side through relative down-dropping of the hangingwall of each of the primary fracture planes.

A throw of ~1.75 m is evident on the BF at the fan surface, however it is unclear
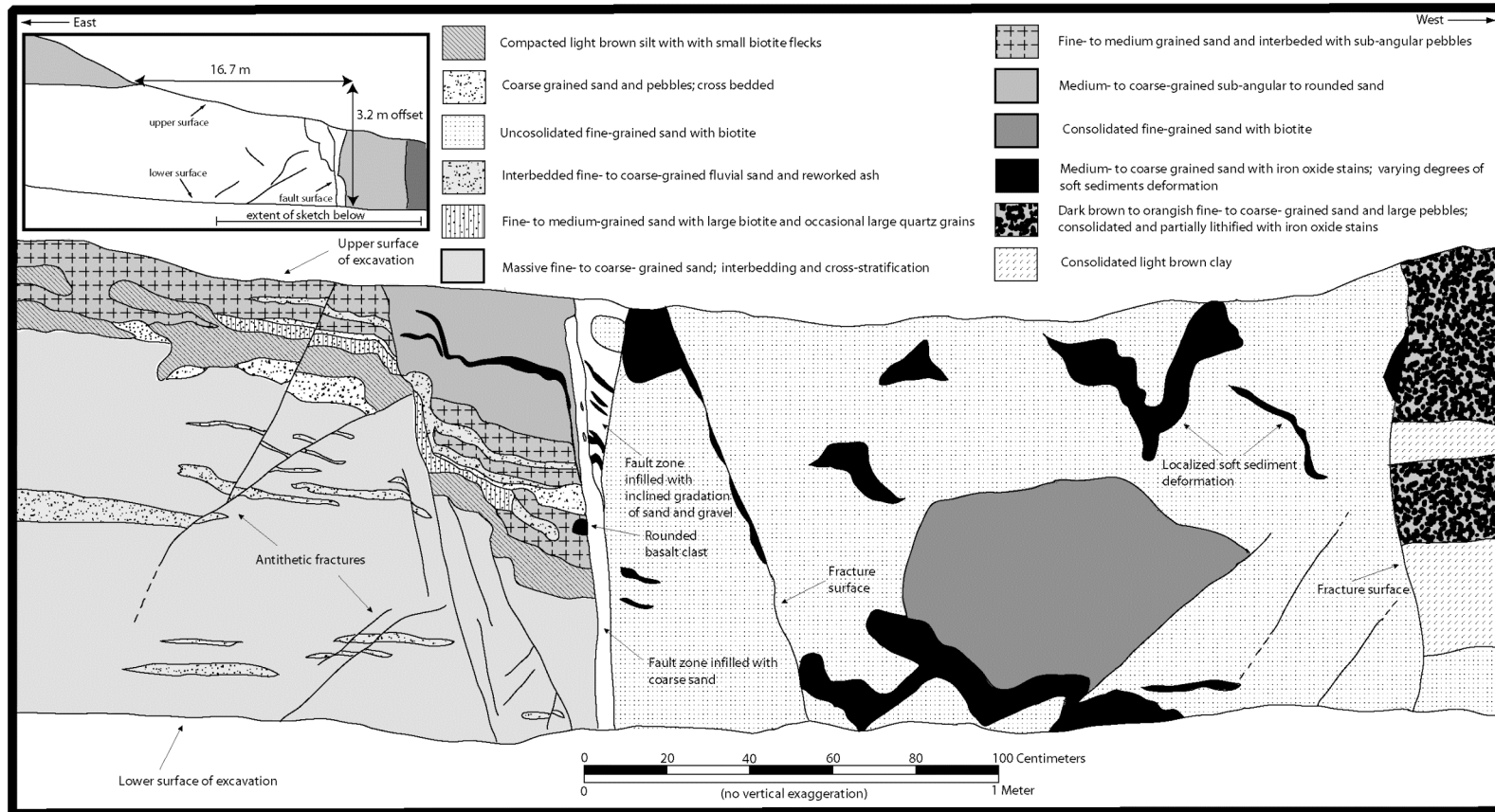
Figure 2-5. Cross-section of the Bishop Fault (BF) located in the Inyo County Bishop-Sunland Landfill. See Figure 2-2 for location of BF. See Appendix D for further documentation.

how surficial throw relates to displacement at depth (i.e. whether it represents part of, or should be counted in addition to throw at depth). The age of the fan surface remains uncertain, however, Bateman (1965) assigns it to Mid-Late Pleistocene age. Comparison of the fan surface character to that of other younger fan surfaces in the area suggests it likely predates the latest glaciation. Assuming a reasonable abandonment age of greater than 25 ka, the estimated Late Pleistocene slip rate for the BF, based only on surface offset, is less than 0.07 mm/yr. This rate nearly matches the inferred rate for the similarly oriented THF of ~0.06 mm/yr.

Klondike Area Faults

The Klondike area exhibits two well-defined northeast-striking, west-dipping normal faults with evidence for Holocene offset (Figure 2-6). The Klondike Lake fault (KLF) forms a prominent 1.8 km long fault scarp exhibiting a maximum offset of ~5 m (Appendix A). The scarp forms a natural dam that has backed up the flow of a small spring-fed stream resulting in the formation of Klondike Lake. Along strike, the scarp exhibits highly variable offset due drainage incision and wave erosion from lake waters.

The Klondike Spring fault (KSF) lies to the north of the KLF (Figure 2-6). This 2.7 km long fault offsets Holocene alluvium and exhibits a maximum throw of ~4 m (Appendix A). From air photos, it appears the KSF scarp may have recently hosted a lake similar to that of Klondike Lake. The hangingwall exhibits active marsh and spring deposits as well as playa deposits, which were likely abandoned when the stream successfully breached the scarp. Both faults are inferred to have exhibited surface rupture from the 1872, Owens Valley earthquake. They mark the northern-most terminus of surface rupture associated with the 1872 event (Beanland and Clark, 1994). Given the
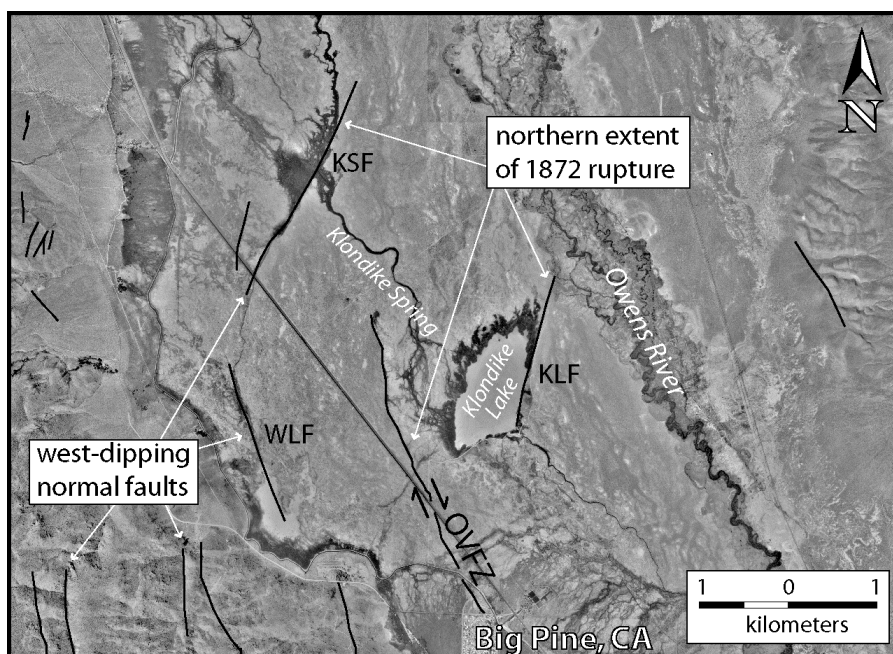
Figure 2-6. The Klondike Lake fault (KLF) and Klondike Spring fault (KSF) mark the northern extent of rupture on the OVFZ during the 1872 Owens Valley earthquake. Normal displacement along each of these faults has resulted in fault damming of a natural spring. The Warren Lake fault (WLF) is west-dipping normal fault that partially displaces a playa deposit

relatively large throws (~4-5 m) measured on each of these faults, and the unstable scarp material (predominantly playa deposits and eolian sands), relatively recent rupture as suggested by Beanland and Clark (1994) is probable.

Faulting along the Coyote Warp

The eastern margin of the Coyote Warp is bounded by a series of discontinuous, west-dipping normal faults that offset Late Pleistocene fan units (Figure 2-2). Faulting is relatively localized along the central and northern portions of the Coyote Warp margin; however, to the south, near Big Pine, faulting is distributed over a broad area of crystalline basement known as the Warren Bench. Collectively, slip on the west-dipping faults along the Coyote Warp has replaced slip on the much larger east-dipping range-front fault, whose existence is inferred from the steep elevation gradient between the range and the valley, and the steep walled bedrock drainages in this area. The presently active west-dipping faults are inconsistent with the observed relief, suggesting they may be a relatively recent occurrence, possibly related to the northward progression of the OVFZ, and its interaction with the pre-existing range-front fault (Chapter 3). Previous analysis of this area has implicated these west-dipping faults as indicative of tectonic warping (Bateman, 1965; Pinter, 1995). Based on field observations, it is probable that faulting in this area is controlled to some extent by a pervasive north-striking, west-dipping joint set, which is visible within many of the bedrock outcrops along the eastern margin of the Coyote Warp. However, despite the inferred exploitation of pre-existing bedrock weaknesses, the origin of these faults has largely remained enigmatic. Chapter 3 explores the origin of the Coyote Warp.

Conclusion

The field area for this project encompasses a host of readily observable geologic and geomorphic features, which together are used to gain insight into the relationship between northern Owens Valley and the greater deforming region of eastern California. The observations and interpretations presented here illustrate the diverse means with which to account for the continuum of deformation associated with this area, and thus provide a foundation for more encompassing interpretations of deformational history. These varied observations have guided the observations and interpretations presented in the following chapters.

Chapter 3

Conjugate fault failure in crustal scale extensional fault populations: An example from the eastern Sierra Nevada, California

Abstract

Simple geometric constraints can be used to predict fault intersection at depth. Here we use a theoretical relationship between fault dip, horizontal fault spacing, and seismogenic thickness to explain the unique structure of northern Owens Valley, California, as well as its relationship to through going dextral shear associated with the Owens Valley (OVFZ) and White Mountains (WMFZ) fault zones. Our results suggest that the Coyote Warp fault (CWF), an inferred east-dipping segment of the Sierra Nevada frontal fault system, became inactive due to intersection with the west-dipping WMFZ. Conversely, to the north of the CWF, the geometric relationship between the Round Valley fault and the WMFZ, combined with evidence for Late Pleistocene fault activity on both structures, suggests these two antithetically dipping faults are spaced sufficiently for uninhibited down-dip propagation within the brittle upper crust. Furthermore, the geometry and spacing of the OVFZ and Birch Mountain fault (BMF), a segment of the Sierra Nevada frontal fault system located south of the CWF, suggest that these two faults do not intersect within the seismogenic layer. Based on several lines of geologic evidence, however, we suggest that the positioning of the BMF may have been influenced by the development of the nearby OVFZ.

Introduction

Interactions among faults, through crustal stress perturbations and ultimate structural linkage, play an integral role in the development of tectonic landscapes. Between crustal scale normal faults, such interactions have implications for the evolution of associated range and basin morphology in that they govern the fundamental structural characteristics of extensional settings. For example, early in the development of large normal fault systems, along-strike segmentation typically gives rise to a series of discrete basins; however, continued development and eventual linkage of the bounding fault

segments results in a significant change in structural character, as the initial basin array

is amalgamated into a single large composite basin (e.g. Anders and Schlische, 1994;

Schlische and Anders, 1996). Such structural changes may also be reflected in the

adjacent footwall morphology in the form of steps or relay-ramps (e.g. Larson, 1988;

Peacock and Sanderson, 1991), which typically provide primary pathways for drainage

and sediment distribution (e.g. Jackson and Leeder, 1994; Densmore et al., 2003).

     In a similar manner, down-dip linkage of conjugate normal fault pairs also

influences basin and range development. Scholz and Contreras (1998) suggested that

such linkage plays an important role in the development of continental rift basins. They

proposed a simple model of rift development where conjugate fault growth and

subsequent down-dip intersection within the brittle portion of the upper crust guides basin

development from an initially symmetric configuration to an asymmetric system when

one fault effectively becomes "locked" as a failed conjugate. Explicit in this model is

that a combination of dip angle and horizontal fault spacing dictates the depth at which

conjugate faults will intersect (Figure 3-1). Because down-dip propagation of crustal

scale faulting is inhibited at depths below the lower bound of the seismogenic layer (e.g.

Scholz, 2000), there is a finite range of values for fault spacing and dip angle that will

result in physical intersection and subsequent conjugate fault locking, or death, within the

upper crust. The occurrence of intersection at depth inhibits further propagation of the

affected antithetic fault (e.g. Jackson and McKenzie, 1983; McLeod et al., 2000; Scholz

and Contreras, 1998), and is reflected in the development of associated hangingwall and

footwall morphology. There are few recognized examples, however, of conjugate fault

intersection where its effect on well-developed range and basin morphology has been
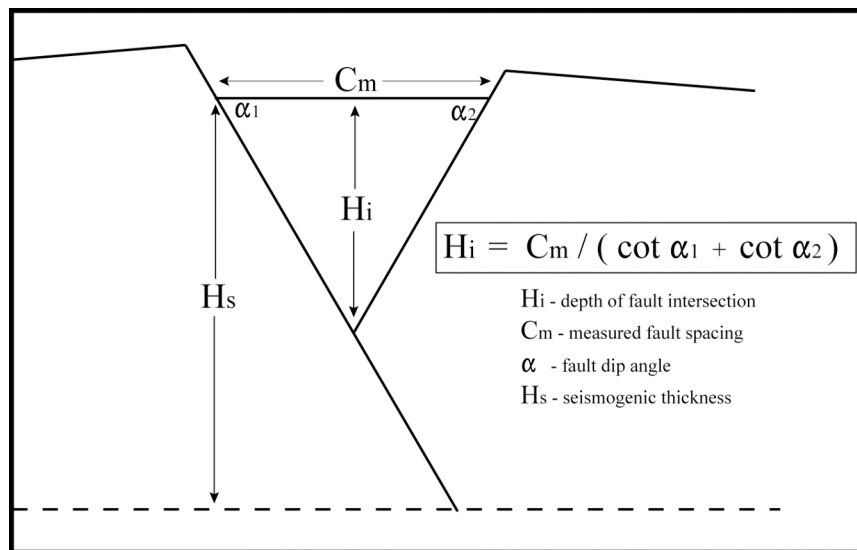
Figure 3-1. Cross-sectional diagram of a conjugate fault pair. The depth of fault intersection, H_i is a function of horizontal fault spacing, C_m, and dip of the respective fault planes, α_1 and α_2. If intersection occurs above the seismogenic base, H_s then one fault becomes locked as a failed conjugate, and an asymmetric basin develops (e.g. Scholz and Contreras, 1998).

assessed.

Here we apply a model similar to that derived by Scholz and Contreras (1998), in which we use the theoretical relationship between fault dip, horizontal fault spacing, and depth to the base of seismogenic zone to explain the Neogene structural evolution of northern Owens Valley, California, located within the Eastern California Shear Zone (ECSZ) (Figure 3-2). Our analysis is supplemented with new geologic evidence derived from deformed Late Pleistocene geomorphic features, which reflect activity along the range-front faults of northern Owens Valley. We also discuss the relationship between the largely normal fault controlled structure of northern Owens Valley and the distribution of through-going dextral shear within this part of the ECSZ.

Geologic Setting

Owens Valley is the westernmost of a series of prominent north-trending extensional basins located in eastern California between the Sierra Nevada batholith and the Basin and Range province (Figure 3-2). The valley, which extends ~160 km from the Garlock fault to Long Valley Caldera, is characterized as a structural basin bounded by the range-front faults of the Sierra Nevada and White-Inyo Mountains. The formation of Owens Valley is largely attributed to extension beginning during Middle Miocene-Pliocene time that has since resulted in the development of steep escarpments with elevations in excess of 4 km (Bateman, 1965; Bachman, 1978; Stockli et al., 2003). East-west extension within the valley is primarily accommodated on segments of the greater Sierra Nevada frontal fault zone (SNFF), including the Round Valley (RVF), Birch Mountain (BMF), and Independence faults (Bateman, 1965; Bryant, 1984; Gillespie, 1991), and on the dextral-oblique White Mountains fault zone (WMFZ) (dePolo, 1989;
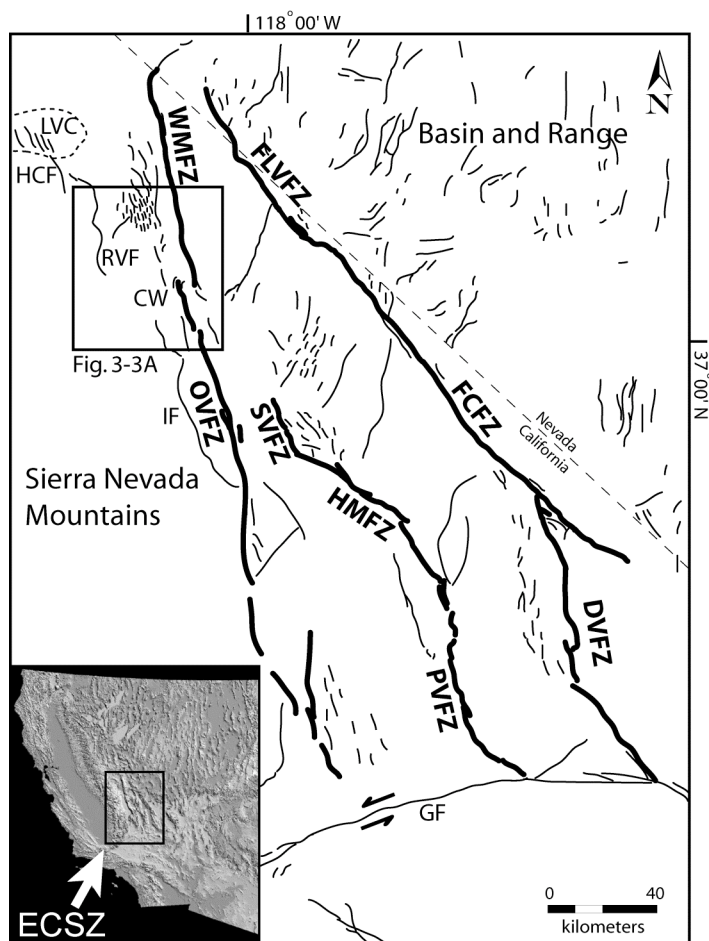
Figure 3-2. Map of Late Cenozoic faults of the Eastern California Shear Zone (ECSZ) north of the Garlock fault (GF). Dextral fault zones of the ECSZ (indicated by bold dark traces) include the Death Valley (DVFZ), Furnace Creek (FCFZ), Fish Lake Valley (FLVFZ), Panamint Valley (PVFZ), Hunter Mountain (HMFZ), Saline Valley (SVFZ), Owens Valley (OVFZ), and White Mountain (WMFZ) fault zones. CW – Coyte Warp; HCF – Hilton Creek Fault; IF – Indepence fault; LVC – Long Valley Caldera; RVF – Round Valley fault. Box denotes extent of field area of northern Owens Valley dipicted in Figure 3-3.

Stockli et al., 2003; Kirby et al., 2006).

The current tectonic environment of Owens Valley is dominated by dextral shear on the Owens Valley fault zone (OVFZ) and the WMFZ, which initiated during the Middle Pliocene (Stockli et al., 2003) (Figure 3-2). These two fault zones, together with the Fish Lake Valley-Furnace Creek-Death Valley and the Saline Valley-Hunter Mountain-Panamint Valley fault zones of the ECSZ, accommodate ~25-30% of the relative motion associated with the North American-Pacific plate boundary (Dixon et al., 1995; Bennett et al., 1999; Dixon et al., 2000; Gan et al., 2000; McClusky et al., 2001; Miller et al., 2001; Oldow et al., 2001).

Several unique structural and kinematic aspects characterize the northernmost portion of Owens Valley (Figure 3-3A). Notably, a large portion of the Sierran range-front associated with this area, known locally as the Coyote Warp, lacks evidence for an active east-dipping range-front fault. Deformation along the eastern margin of the Coyote Warp, as well as to the south, is largely characterized by numerous west-dipping, or mountain-down, normal faults (Figure 3-3A), which in some cases offset basement by up to ~120 m. The crest of the Coyote Warp is described as a broad, locally subdued, low relief erosional surface situated at an elevation of ~3,300 m (Bateman, 1965). Moreover, the southeastern margin of the Coyote Warp is coincident with the northern-most extent of surface rupture associated with the 1872, Owens Valley earthquake (Beanland and Clark, 1994). The existence of several northeast striking, west-dipping extensional structures within the valley floor east of the Coyote Warp suggest that dextral shear on the OVFZ is transferred east to the WMFZ in this area (Figure 3-3A). Furthermore, to the north, near the town of Bishop, the northern margin of the Coyote
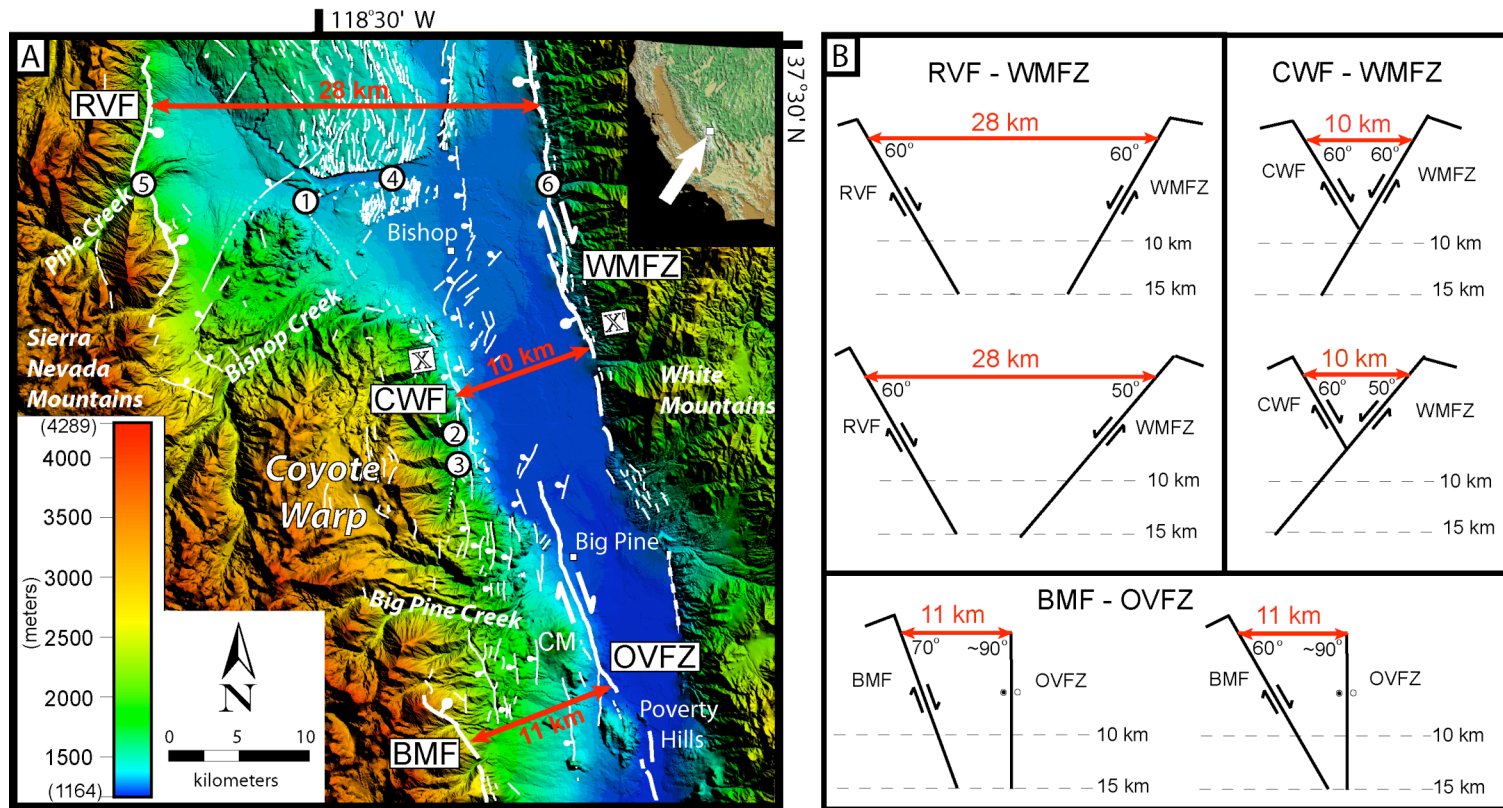
Figure 3-3. A) Combined digital elevation model (DEM) and fault map of northern Owens Valley with cross section locations denoted by red arrows. Faults compiled from Bateman (1965), Bryant (1984), Beanland and Clark (1994) and new mapping. X-X' denotes location of gravity profile (Figure 3-9) modified from Bateman (1965). Numbers denote site locations for this and other studies: Site 1 - Horton Creek terraces; Site 2 - Freeman Canyon; Site 3 - Shannon Canyon; Site 4 - Owens River terraces (Pinter, 1995); Site 5 – Pine Creek (Berry, 1997); Site 6 – Silver Canyon (Kirby et al., 2006). **(B)** East-west cross sections from northern Owens Valley illustrate the relationship between fault spacing, fault dip, and depth of fault intersection within the context seismogenic thicknesses of 10 km and 15 km. BMF – Birch Mountain fault; CWF – Coyote Warp fault; RVF – Round Valley fault; OVFZ – Owens Valley fault zone; WMFZ – White Mountains fault zone; CM – Crater Mountain.

Warp is defined by a large (~20 km) westward step in the Sierran range-front, which consequently increases the valley width by a factor of three (Figure 3-3A).

The Coyote Warp has previously been described as a tectonic hinge that accommodates both the westward rotation of the Sierra Nevada and the eastward rotation of Owens Valley (Pinter, 1995). While this model explains the present tectonic role of the Coyote Warp, it fails to address the underlying mechanics responsible for its development. Furthermore, we note that the relationship between the Coyote Warp and the greater OVFZ-WMFZ has received little attention despite their close proximity.

Geometric Relations of Conjugate Normal Faults

The development of conjugate normal faults in extensional settings, such as continental rifts, can lead to fault intersection at depth, and may result in the subsequent death of one of the constituent faults if intersection occurs within the brittle upper crust (Scholz and Contreras, 1998). The depth of intersection (H_i) for a conjugate fault pair is dependent on the horizontal fault spacing and the fault dip (Figure 3-2). This depth is calculated using the equation:

$$H_i = C_m / (\cot \alpha_1 + \cot \alpha_2), \tag{1}$$

where α_1 and α_2 are the respective dip angles for the constituent faults, and C_m is the measured horizontal distance between surface exposures of the two faults. This relationship is illustrated graphically in Figure 3-4 for conjugate fault pairs with the same dip. If H_i is greater than the inferred depth of the seismogenic base, then a conjugate fault pair is *not* expected to intersect within the seismogenic layer, and thus each fault is able to continue to accrue displacement. Conversely, if H_i is less than the inferred depth to the seismogenic base, then the faults are expected to intersect, with one fault becoming
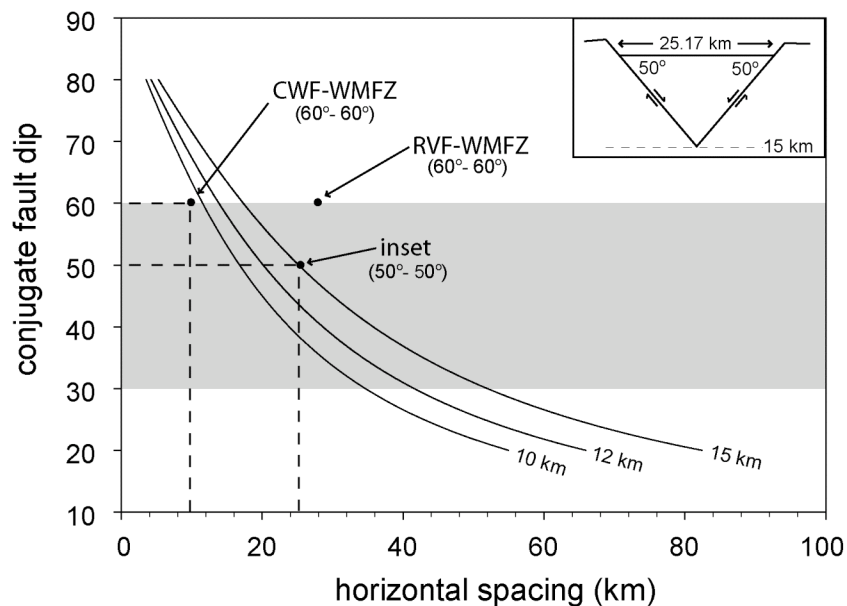
Figure 3-4. The predicted depth of fault intersection is illustrated by a plot of normal fault dip versus horizontal spacing between two adjacent conjugate faults. Plotted points represent the depth of intersection for two faults with a given dip and spacing. Plotted curves represent lines of equal depth, which correspond here to the inferred seismogenic thickness (H_i). If a conjugate fault pair plots below a given curve, this suggests the two faults intersect above the seismogenic base, and therefore one fault should become inactive as a failed conjugate. Faults that plot above a given curve are projected to intersect below the seismogenic base, and thus each remains active. The shaded region indicates the typical range of dips (30°-60°) observed for crustal scale normal faults (Jackson and White, 1989). Inset is an example cross-section that illustrates a hypothetical conjugate fault pair. In this case, two conjugate faults spaced ~25 km with dips of 50° will intersect at 15 km depth. Based on 60° dips, the graph suggest that the CWF and WMFZ intersect within the seismogenic upper crust, where as the RVF and WMFZ do not.

inactive as a failed conjugate (e.g. Jackson and McKenzie, 1983; Scholz and Contreras, 1998). The first scenario will result in the evolution of a more or less symmetric graben with potentially similar displacements being accommodated on the graben bounding faults. In the latter scenario, a symmetric graben will also form; however, once the faults propagate to the point of intersection, one of the graben bounding faults will become locked due to the displacement of its propagation plane, and relative subsidence along one side of the graben will cease. The active fault will continue to accrue displacement, and the valley structure will evolve from its initially symmetric graben configuration to a more asymmetric form (e.g. Scholz and Contreras, 1998).

Similarly, for conjugate normal faults with down-dip dimensions that span the thickness of the seismogenic layer, there exists a critical spacing (C_h), below which fault intersection is expected to occur *above* the seismogenic base. Critical spacing is defined here as the horizontal map-view distance required for a pair of conjugate faults to intersect precisely at the seismogenic base. The critical spacing for a conjugate fault pair is thus a function of both the inferred depth to the seismogenic base (H_s) and the assumed fault dip. It is calculated by rearranging equation (1) to:

$$C_h = H_s (\cot \alpha_1 + \cot \alpha_2) \qquad\qquad (2)$$

Fault spacing measured in map view can be compared to C_h in order to determine whether or not intersection is likely. If the measured spacing is smaller than C_h then the faults likely intersect within the seismogenic layer, and thus the implications discussed above will apply. Alternately, fault spacing greater than C_h is not expected to result in physical intersection at depth.

Implicit in this approach is the assumption that fault geometry remains essentially

planar throughout the subsurface extent of a given fault. Any deviation from the inferred or measured fault dip at the surface will introduce error into the calculations of the predicted depth of intersection and critical spacing. However, despite uncertainty concerning fault dip at depth, we expect deviations in dip to result in shallower depths of intersection than predicted here, owing to the tendency of some large normal faults to become listric or flatten with depth (Jackson and McKenzie, 1983). We note there is an indication that large seismic ruptures of normal faults generally occur along essentially planar surfaces to depths of up to 10 km (e.g. Stein and Barrientos, 1985; Jackson and White, 1989). Another point of uncertainty pertains to the seismogenic base, which, rather than a discrete boundary, represents a gradational zone characterized by brittle tendencies at shallower depths, and by ever increasing ductility with greater depth (e.g. Scholz, 2000).

Here we apply the above relationships to northern Owens Valley (Figure 3-3), where basin geometry is highly variable within our field area. We also examine deformation associated with range-front faulting in an effort to relate fault activity to predictions of subsurface geometry for the existing range-front conjugate fault pairs.

Data and Methods

A fault map for northern Owens Valley (Figure 3-3A) was compiled from several sources, including Bateman (1965), Bryant (1989), and Beanland and Clark (1994), and from field mapping supplemented by analysis of 1:40,000 scale aerial photographs. Cross-sections were generated from the finalized fault map in an effort to illustrate the fundamental aspects of basin and fault geometry within northern Owens Valley (Figure 3-3B). We calculated the depth of fault intersection based on measured fault spacing and

fault dip (Equation 1; Figure 3-1). Fault spacing was obtained from the fault map of northern Owens Valley, and is defined as the distance between the surface expressions of range-front faulting. Fault dips, which are assumed here to be representative of fault plane orientation at depth, are inferred based on previously reported field measurements for the RVF (Bateman, 1965; Bryant, 1984), BMF (Bateman, 1965), OVFZ (Beanland and Clark, 1994), and WMFZ (Stockli et al., 2003).

The maximum depth of observed seismicity in this area is used to approximate the seismogenic thickness. Earthquake and aftershock locations from the 1986 Chalfant Valley earthquake sequence near the eastern margin of Volcanic Tableland, just north of Bishop, reveal two distinct cutoff depths for seismicity at approximately 10 km and 15 km (Smith and Priestly, 2000). These depths are similar to those used to define the seismogenic base in previous rheologic models proposed for the ECSZ (e.g. 15 km, Malservisi et al., 2001; 10 km, Dixon et al., 2003). For this study we represent the seismogenic thickness at both 10 km and 15 km (Figure 3-3B).

In an effort to gauge the relative magnitude of fault related deformation within northern Owens Valley, several geomorphic surfaces associated with faulting along Round Valley and the Coyote Warp were surveyed using a differential global positioning system (DGPS). We conducted DGPS transects oriented approximately perpendicular to the north-trending horizontal tilt axis for terrace surfaces near Horton Creek in Round Valley (Figure 3-5), and in Freeman Canyon along the eastern margin of the Coyote Warp (Figure 3-6), as well as a fan surface near the mouth of Shannon Canyon (Figure 3-7). In this manner we obtained east-west trending elevation profiles, which were then used to calculate slopes for several generations of alluvial surfaces. For a given survey
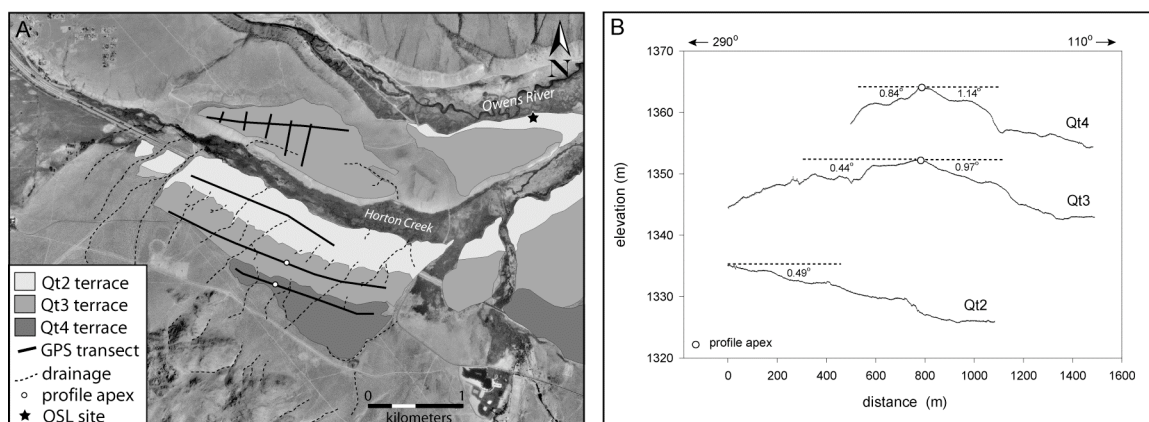
Figure 3-5. A) Aerial image of mapped Horton Creek terraces. These terrace units are continuous with the Owens River terraces to the east. Heavy lines indicate DGPS tracks. Southern terrace transects are oriented to 290°. Elevation data obtained from the northern terrace transects define a plane dipping 1.13° oriented to ~220°. **B)** Elevation profiles for the southern terrace transects. Elevation data for the Qt1 surface (not shown), representative of the modern floodplain of Horton Creek, was derived from a USGS DEM.
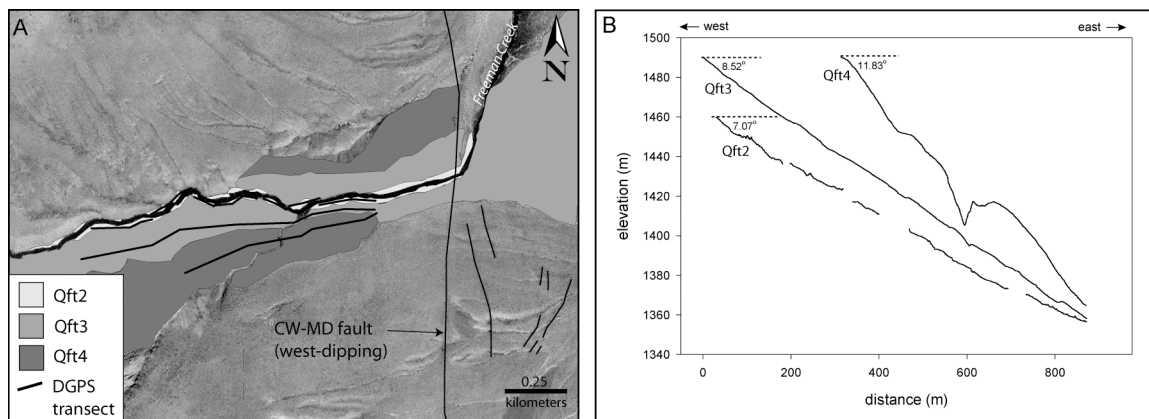
Figure 3-6. A) Aerial image of mapped Freeman Canyon terraces. Heavy lines indicate DGPS tracks. The Qt2 surface is discontinuous due to erosion by the modern stream. CD-MF fault – Coyote Warp-Mountain Down fault. **B)** Elevation profiles for the terrace transects. Elevation data for the Qft1 surface (not shown), is representative of the modern stream gradient, was derived from a USGS DEM.
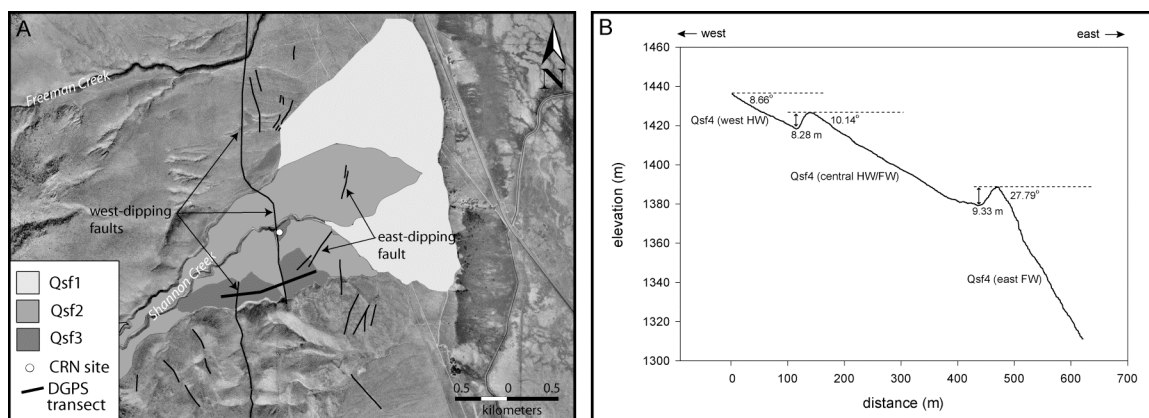
Figure 3-7. A) Aerial image of mapped Shannon Canyon fans. Heavy line indicates DGPS track. **B)** Elevation profile indicates offset on two west-dipping faults, and subsequent fan surface tilt.

location, we assume that the orientation of the most recently active surface (Qt1 for the Horton Creek terraces, and Qft1 for the Freeman Canyon terraces) approximates the original orientation of the successively older surfaces. The relative magnitude of deformation for a given surface is defined as the degree of tilt on a horizontal axis required to restore that surface to an orientation similar to that of the youngest observed surface. We calculated tilt rates based on the inferred ages of each surface.

The age ranges used here for the terrace surfaces of Horton Creek are based on correlations of the nearby Owens River terraces with glacial moraines in Pine Creek, a major glaciated drainage along the western margin of Owens Valley (Pinter et al., 1994). Note that the terraces associated with Horton Creek and those of the Owens River together form continuous units; however, in order to differentiate between site locations we refer to them separately. The work of Pinter et al. (1994), which is based on comparisons of clast weathering rinds and soil descriptions, and supplemented with a radiocarbon age of 7170 ± 100 yr B.P. derived from a clast-carbonate coating, correlates the abandonment ages of the Qt2, Qt3, and Qt4 surfaces to the waning stages of the Tioga, Tahoe, and pre-Tahoe glaciations, respectively, of the Sierra Nevada Mountains. However, because few solid numerical age constraints exist for the moraines of Pine Creek (e.g. Birkeland et al., 1991; Bierman and Gillespie, 1994) and due to the uncertainty involved in the relative age correlations, as well as, the potential for contamination of the carbonate age source (Pinter et al., 1994, Pinter and Keller, 1995), these initial terrace age constraints are regarded as tentative.

Definitive ages for terrace surfaces of Freeman Canyon and the fan surface at Shannon Canyon are lacking, however, it is probable that each of these surfaces were

abandoned during Late Pleistocene time (< 200 ka) (Bateman, 1965). We note that despite remaining uncertainty associated with the Owens terrace age correlations (Pinter et al., 1994; Berry, 1997), and the Freeman and Shannon Canyon units, the surfaces from each of these locations collectively provide a measure of the magnitude of Late Pleistocene deformation, which is useful in our broader discussion and comparison of range-front activity within northern Owens Valley.

In an effort to relate terrace tilting to hangingwall deformation associated with nearby faulting, tilted terrace surfaces were projected towards the associated tilt-inducing fault planes in order to estimate the slip rate required to account for the degree of observed tilt. In this manner we used the tilt of the Freeman Canyon terraces to derive relative slip rates for a small west-dipping fault along the Coyote Warp (CW-MD) (Figure 3-6A). Given the potential for other deformation mechanisms, such as distributed faulting or flexure associated with hangingwall subsidence, we acknowledge that this method provides an approximate measure of slip rate; however, because these mechanisms are expected only to increase the amount of displacement projected for a given fault, we suggest that rates determined by this method approximate minimum slip rate estimates.

Results

The basin width of northern Owens Valley varies from ~10 km between the inferred CWF and WMFZ, to ~28 km between the RVF and WMFZ (Figure 3-3A). The map view distance between the BMF and the OVFZ is ~11 km. Observations of fault dip obtained from fault plane exposures along the RVF are in the range of 45°-70° E (Bateman, 1965; Bryant, 1984). Here we assign the RVF a dip of 60° E (Figure 3-3B),

which is consistent with typical observations of large normal faults (e.g. Jackson and White, 1989). Mean dip measurements taken from fault plane exposures along the WMFZ suggest it has a dip of ~50°-55° W (Stockli et al., 2003). Based on these values we illustrate the WMFZ using dips of 50° and 60° (Figure 3-3B). Fault plane measurements for the BMF indicate it has a dip of ~70° E (Bateman, 1965). In order to illustrate the sensitivity of the BMF-WMFZ section to fault dip, we assign the BMF dips of 60° and 70° (Figure 3-3B). The OVFZ has an average dip of 80°±15° E. This estimate is inferred from measurements of surface rupture associated with the 1872 Owens Valley Earthquake (Beanland and Clark, 1994). Here we approximate the OVFZ using a vertical fault plane (Figure 3-3B). The CWF, which exhibits no Late Pleistocene surface expression, is a segment of the SNFF that is inferred largely from the elevation contrast (up to ~2 km) between the crest of the Coyote Warp and the adjacent valley floor, and additionally from gravity data (Bateman, 1965; Hollett et al., 1991). Given the paucity of available fault plane data we assign it a dip of 60° E (Figure 3-3B). We consider this estimate reasonable given the range of fault dips observed or inferred along the remainder of the Sierran range-front (Bateman, 1965; Gillespie, 1982; Bryant, 1984), as well as, those observed along typical large normal faults (e.g. Jackson and White, 1989).

Depths of Predicted Fault Intersection

Based on the determined fault dips and spacings, the predicted depth of intersection for the conjugate fault pairs examined here ranges from 7.1 to 8.7 km for the CWF-WMFZ, and from 19.8 to 24.2 km for the RVF-WMFZ (Figure 3-3B and Table 3-1). By accounting for the elevation difference between fault surface exposures (~2 km),

TABLE 3-1. FAULT AND BASIN GEOMETRY

section	dip	fault spacing (basin width, km)	predicted depth of intersetcion (km)
RVF - WMFZ	$60° - 60°$	28	24.2
	$60° - 50°$		19.8
CWF - WMFZ	$60° - 60°$	10	8.7
	$60° - 50°$		7.1
BMF - OVFZ	$70° - 90°$	11	28.3
	$60° - 90°$		17.1

See Figure 3-3A for section locations.

the predicted depth of intersection for the BMF-OVFZ ranges from 17.1 km, for a dip of 60°, to 28.3 km for a dip of 70° (Table 3-1).

Geomorphic Surface Ages

The abandonment ages of the alluvial surfaces examined here are based primarily on Pinter's et al. (1994) correlation of the Owens River terraces with the glacial moraines of Pine Creek. We use several published age constraints for the upper and lower bounds of the Tioga (15-25 ka), Tahoe (55-130 ka) and Pre-Tahoe (130-200 ka) glaciations to infer limiting age ranges the Qt2, Qt3, and Qt4 surfaces, respectively (Table 3-2). Moreover, the inferred age of the Qt2 terrace surface is corroborated by an optical stimulated luminescence (OSL) age of 21 ± 3.3 ka (see Chapter 4; Appendix F).

DGPS Transect Data

Data from the DGPS transects and calculated tilts are listed in Table 3-3. The Horton Creek terraces, located near the west side of northern Owens Valley (Site 1, Figure 3-3A), exhibit both east and west oriented slopes. The oldest terrace surfaces, Qt4 and Qt3, are characterized by convex topographic profiles with spatially corresponding apices (Figure 3-5B). Both the east and west limbs of the Qt4 and Qt3 profiles exhibit increasing slope, and thus estimated tilt, with increasing age. The Qt2 terrace surface and the modern floodplain (Qt1) are each characterized by tilting to the east. The slope of the Qt2 surface (0.49°) matches the slope of the modern floodplain (0.48°), both of which are oriented to the east. This slope is consistent with the trend of increasing slope and surface age observed for the east-tilted limbs of the Qt3 and Qt4 surfaces. Elevation data obtained from a DGPS survey conducted north of Horton Creek indicates that the Qt3 terrace surface can be approximated by a plane with a dip of 1.13° oriented toward ~220°

TABLE 3-2. GLACIAL AGE CONSTRAINTS IN THE SIERRA NEVADA

Glacial Stage	age constraints (ka)	study	ages inferred from
Tioga	15 - 30.5	Bischoff and Cummins (2001)	rock flour in Owens Lake core
	18.6 +/- 1.2	James et al. (2001)	cosmogenic ^{10}Be and ^{26}Al dating of erratics
	>14 - 15	Clark and Gillespie (1997)	radiocarbon dating of lake cores
	15 - 28	Benson et al. (1996)	^{18}O, TOC, TIC, mag. suscep. in core sediment
	16 - 25	Phillips et al. (1996)	cosmogenic ^{36}Cl dating of moraine deposits
	>15.5 - 16.2	Mensing (2001)	pollen and algae from Owens Lake core
	>14.8	Porinchu et al. (2003)	insect abundance in high altitude lake core
	>17 - 19	Koehler and Anderson (1995)	vegetation changes in packrat middens
	<25.2 +/- 2.5	Bursik and Gillespie (1993)	RD techniques (e.g. morphology, weathering)
	20.4 - 23.1	Phillips et al. (1990)	cosmogenic ^{36}Cl dating of morraine deposits
Tahoe	68.1 - 78.0	Bischoff and Cummins (2001)	rock flour in Owens Lake core
	55.9 - 65.8	Phillips et al. (1990)	cosmogenic ^{36}Cl dating of morraine deposits
	< 119 +/- 7	Gillespie (1988)	dated basalt
Pre-Tahoe	133 - 218	Phillips et al. (1990)	cosmogenic ^{36}Cl dating of morraine deposits
	>131 +/- 10	Gillespie (1988)	dated basalt

TABLE 3-3. LATE PLEISTOCENE DEFORMATION IN NORTHERN OWENS VALLEY

study	location	transect	landform age (ka)	slope (°)	estimated tilt (°)[#]	direction	rate (°/Ma)	estimated vert. slip rate (mm/yr)[&]
this study		VT*	760 [§]	1.31	1.31	W	1.72	
	Horton Creek terraces (Site 1, Fig. 3-1A)	Qt4 (west limb)	130 - 200	0.84	1.32	W (290°)	6.6 - 10.2	
		Qt4 (east limb)		1.14	0.66	E (110°)	3.3 - 5.1	
		Qt3 (north tran.)	55 - 130	0.39	0.87	W (290°)	6.7 - 15.8	
		Qt3 (north tran.) [†]		1.13		SW (220°)		
		Qt3 (south tran., west limb)		0.44	0.92	W (290°)	7.1 - 16.7	
		Qt3 (south tran., east limb)		0.97	0.49	E (110°)	3.8 - 5.1	
		Qt2	15 - 25	0.49	0.01	E (110°)	0.4 - 0.7	
		Qt2	21 ± 3.3 (OSL)	0.49	0.01	E (110°)	0.4 - 0.6	
		Qt1 (modern floodplain)*	------	0.48	------	E (110°)	------	
	Freeman Cyn terraces (Site 2, Fig. 3-1A)	Qft4	< 200	11.83	6.85	E	> 34.3	> 0.3 (CW - MD fault)
		Qft3	(?)	8.52	3.54	E		
		Qft2	15 - 25 (?)	7.07	2.09	E	83.6 - 139.3 (?)	0.4 - 0.7 (CW - MD fault)
		Qft1 (modern stream)*	------	4.98	------	E	------	
	Shannon Cyn alluvial fan (Site 3, Fig. 3-1A)	Qsf3 (west HW)	< 200	8.66	3.68	E	> 18.4	> 0.1 (CW - MD fault)
		Qsf3 (central HW/FW)		10.14	5.16	E	> 25.8	
		Qsf3 (east FW)		27.79	22.81	E	> 114.1	
Pinter (1995)		VT	760	1.40	------	E	------	
	Owens River terraces (Site 4, Fig. 3-1A)	Qt4 (pre-Tahoe)	79 - 218	0.78	0.52	E	2.4 - 6.6	
		Qt3 (Tahoe)	53 - 119	0.72	0.42	E	3.5 - 7.9	
		Qt2 (Tioga)	13 - 26	0.40	0.11	E	4.2 - 8.5	
		Qt1 (modern)	------	0.29	------	E	------	
Berry (1997)			130 - 188		0.25 - 0.54 [$]	W		0.4 - 0.6 (RVF)
	Pine Ceek		64 - 140		0.12 - 0.53 [$]	W		0.4 - 0.8 (RVF)
	morraines (Site 5, Fig. 3-1A)		15 - 25		0.03 - 0.12 [$]	W		0.4 - 1.0 (RVF)
Kirby et al. (2006)			760					0.15 - 0.25 (WMFZ)
	Silver Cyn alluvial fan (Site 6, Fig. 3-1A)		72 ± 15					0.1 - 0.2 (WMFZ)

* Elevation data obtained from 10 meter USGS digital elevation model.   Other transects for this study were obtained using DGPS.

[§] Ar^{40}/Ar^{39} dating of sanidine from the Bishop Tuff yield ages of 757.7 ± 1.8 ka (basal air fall pumice) and 762.2 ± 4.7 ka (overlying ash flow tuff) (Sarna-Wojcicki et al., 2000).

[†] Several north-south trending DGPS transects (Fig. 3-5) combined with the Qt3 (north) east-west transect are fit with a plane oriented to the southwest with a dip of 1.13° .

[#] Estimated tilt calculated relative to the slope of the modern flood plain (Qt1) or the modern stream (Qft1).

[$] Projected range of tilt for the RVF hangingwall block based on the slip rate estimates of Berry (1997).

[&] Slip rates associated with the CW-MD fault are projected from tilted terraces surfaces. Other slip rates are inferred from measured scarp offsets.

RVF - Round Valley fault; CW-MD - Coyote Warp mountain-down (west-dipping) faults; WMFZ - White Mountain fault zone; VT - Volcanic Tableland.

(Table 3-3). The apparent dip of the Qt3 surface resolved to 290° (the same dip direction as the southern terrace transects), is 0.39°, which compares well with the dip measured on the corresponding Qt3 terrace to the south (0.44°).

Tilt rates derived from the west-tilted portions of the Qt4 and Qt3, are 6.6°-10.2°/Myr, and 6.7°-15.8°/Myr (north terrace) and 7.1°-16.6°/Myr (south terrace), respectively. The east-tilted portions of the terrace surfaces have inferred tilt rates of 3.3°-5.1°/Myr (Qt4), 3.8°-5.1°/Myr (Qt3), and 0.4°-0.6°/Myr (Qt2), respectively. The eastward tilt rates for the Qt4 and Qt3 surfaces compare well with the eastward tilt rates presented by Pinter (1995) of 2.4°-6.6°/Myr (Qt4), and 3.5°-7.9°/Myr (Qt3), which were derived from correlative exposures of the Owens River terraces located in the central portion of the valley (Site 4, Figure 3-3A).

The east-tilted Freeman Canyon terrace surfaces, located along the eastern margin of the Coyote Warp (Site 2, Figure 3-3A), exhibit a trend of increasing slope with increasing age. The modern streambed (Qft1) has a slope of ~5.0°, whereas the Qtf2, Qtf3, and Qtf4 surfaces have slopes of ~7.1°, ~8.5°, and ~11.8°, respectively (Figure 3-6B). Based on these measured tilts, and if we assume that periods of significant aggradation and subsequent incision were contemporaneous throughout Owens Valley, the projected Late Pleistocene slip-rate for a prominent west-dipping normal fault located ~300 m east of the down-gradient elevation convergence of the terraces surfaces is estimated to be less than ~1.0 mm/yr down to the west (Table 3-3). While speculative, we suggest the abandonment age of the Qft2 surface, upon which this rate estimate is based, likely post-dates the Tioga Glaciation (15-25 ka). We base this assertion on the relatively small amount of present-day stream incision (~5 m) evident within the Qft2

surface.

The oldest fan surface (Qsf3) associated with Shannon Canyon is offset at two locations by prominent west-dipping faults (Site 3, Figure 3-3A and Figure 3-7). The eastern fault scarp, which can be traced to Freeman Canyon, exhibits a throw (vertical displacement) of 9.33 m. The west scarp exhibits a throw of 8.23 m. The slopes exhibited by the hangingwall-footwall complex increase from 8.7° to 27.8° from west to east (Figure 3-7B). If we assume the Qsf3 fan surface was abandoned by ~200 ka, the combined minimum vertical slip rate across these faults is ~0.1 mm/yr down to the west.

The Birch Mountain Fault and Owens Valley Fault Zone

Several striking observations of faulting in northern Owens Valley provide insight into the relationship between the Sierran range-front and the OVFZ. Firstly, the observed spacing between the BMF and OVFZ (~11 km) very narrowly exceeds the predicted critical spacing (~10 km) derived for a dip of 60° E (BMF) and an inferred seismogenic thickness of 15 km. Similarly, the projected depth of intersection of a 60° E dipping fault with the vertical OVFZ (~17 km) lies relatively close to this seismogenic depth. Secondly, the BMF represents the northernmost surface exposure of the Sierran frontal fault system south of the RVF (Figure 3-3A). The surface trace of the BMF, which is characterized by a moderately sized bedrock scarp (~100 m), is exposed at a relatively high elevation (up to an elevation of ~3,400 m) on the range-front (Figure 3-8). This observation is inconsistent with long-term basin development associated with typical range-front faulting, suggesting that the exposure of the BMF here may be a recent occurrence. While no age constraints exist for the BMF, based on the magnitude of displacement, we suggest that it post-dates the development of the OVFZ. Thirdly, near

Figure 3-8. Westward view of the BMF scarp. The fault scarp is situated at an elevation of ~3,400 m. The positioning of the BMF scarp is inconsistent with long-term range and basin development.

the Poverty Hills (Figure 3-3A), the surface trace of the OVFZ exhibits a prominent westward step which shifts its surface trace ~3 km towards the Sierran range-front (Figure 3-3A). In an east-west sense, this step corresponds with the positioning of the BMF high within the range-front, as well as with the discontinuance of the Sierra Nevada frontal fault just to the north. In a north-south sense, this step also corresponds to the appearance of several distributed west-dipping normal faults, which extend from Crater Mountain (CM, Figure 3-3A) in the Big Pine volcanic field to the southeastern margin of the Coyote Warp.

Discussion

Analysis of fault geometry and basin width provides insight into the structural development of northern Owens Valley. We suggest that the predicted depths of intersection for the conjugate fault pairs of the RVF-WMFZ, CWF-WMFZ, and BMF-OVFZ explains the unique nature of the Sierra Nevada range-front morphology and basin structure in this area. New geologic evidence presented here, is in agreement previous study in the area, and supports our interpretations for the various levels of Late Pleistocene activity associated with range-front faults within northern Owens Valley.

The Round Valley Fault and White Mountain Fault Zone

The simplified RVF-WMFZ cross-section (Figure 3-3B) indicates that the relatively large valley width associated with the northernmost portion of Owens Valley (~28 km), as measured between the associated range-fronts of the Sierra Nevada and White Mountains, precludes fault intersection within the brittle upper crust. The projected depth of intersection (~20-24 km) lies well below the inferred depth of the seismogenic base (10-15 km), suggesting that both the RVF and WMFZ are each capable

of accommodating normal displacement along unimpeded fault planes. If the fault dips

are reduced to minima for the observed ranges (45° for the RVF, and 50° for the WMFZ)

the predicted depth of intersection is 15.2 km. This value matches the lower inferred

bound for the seismogenic base; however, given the striking relief associated with the

RVF, it unlikely the lower dip estimate of 45° is valid.

Detailed DPGS surveys of four terrace surfaces deposited by a tributary of the

Owens River (Horton Creek) (Site 1, Figure 3-3A) provide a relative measure of Late

Pleistocene activity along the RVF. Tilt rates derived from the oldest two surfaces, Qt4

(6.6°-10.2°/Myr) and Qt3 (6.7°-16.7°/Myr), indicate that the magnitude of hangingwall

flexure associated with subsidence along the RVF, meets or exceeds that of the

hangingwall associated the WMFZ since the Late Pleistocene (2.4°-8.5°/Myr; Pinter,

1995; 3.3°-5.1°/Myr; this study) (Table. 2). A comparison of Late Pleistocene extension

rates for the RVF (0.4-1.0 mm/yr; Berry, 1997) and WMFZ (0.1-0.2 mm/yr; Kirby et al.,

2006) corroborates this assessment.

Our estimates of eastward tilt for the Qt4 (0.66° E), Qt3 (0.49° E), and Qt2

(0.01°) terraces compare well with the tilt estimates of Pinter (1995) (Qt4 – 0.52°; Qt3 –

0.42°; Qt2 – 0.11°) (Table 3-3). Overall, while there is significant uncertainty associated

with the estimated ages assigned to these terrace surfaces, and thus the assigned rates of

tilt (Pinter, 1994; Berry, 1997), the general indications of Late Pleistocene activity from

this and other studies, suggest that both the RVF and WMFZ are presently active

structures (Bateman, 1965; Bryant, 1984; Berry, 1997; dePolo, 1989; Stockli et al., 2003;

Kirby et al., 2006).

The Coyote Warp Fault and White Mountain Fault Zone

In contrast to the RVF-WMFZ section, the CWF-WMFZ section indicates that the fault planes associated with the inferred CWF and the WMFZ intersect above the seismogenic base (Figure 3-3B). The graben width of ~10 km between the surface projections of the inferred CWF and WMFZ is unfavorable for each of these faults to have independently propagated to the base of the seismogenic layer. Given the observed graben width, fault dips would need to exceed 80° in order for each fault to have independently propagated to a seismogenic base of 10 km. This estimate is reduced to a minimum dip of 72° for an inferred seismogenic depth of 15 km. Recall that available evidence along the WMFZ indicates an average fault dip of ~50°-55° (Stockli et al., 2003). Note that in the most extreme case, if we approximate the CWF with a vertical fault plane, and use the observed values of dip for the WMFZ, the predicted depth of intersection is between ~12-14 km.

Given the above geometric relationships, we suggest that the structural nature of the Coyote Warp is attributable to inhibited activity along the CWF. Further support for this interpretation comes from several lines of independent geologic evidence. Firstly, the eastern margin of the Coyote Warp lacks evidence for an active east-dipping range-front fault. Faulting along the Coyote Warp is dominated by numerous small west-dipping scarps, which are oriented antithetic to the range-front, and are thus at odds with the observed elevation contrast of ~2 km between crest of the Coyote Warp and the adjacent alluvial floor (Figure 3-3A). Given this elevation difference, it is likely that some amount of valley subsidence/range uplift associated with the eastern margin of the Coyote Warp has occurred.

A second line of evidence supporting inhibited activity along the CWF is derived

from the basement structure of northern Owens Valley, which, adjacent to the Coyote

Warp, resembles an asymmetric graben (Bateman, 1965; Hollett et al., 1991). Geologic

evidence from this area indicates that a significantly larger portion of valley subsidence

has occurred along the White Mountains than along the Coyote Warp (Bachman, 1978;

Bateman, 1965; Hollet et al., 1991). Gravity data provides an indication that a buried

east-dipping fault does exist along the eastern margin of the Coyote Warp (Figure 3-9)

(Bateman, 1965; Hollett et al., 1991). This suspected fault, inferred here to be the CWF,

is buried by a significant amount of valley fill (> 1 km) suggesting it is inactive. Based

on these lines of evidence, we conclude that a significant amount of east-side-down

displacement has accumulated on a range-bounding fault along the Coyote Warp, yet the

rate of normal displacement has either slowed significantly or ceased altogether since, at

the very minimum, Late Pleistocene time.

Evidence from tilted geomorphic features along the eastern margin of the Coyote

Warp provides some insight into Late Pleistocene fault activity in the vicinity of the

inferred CWF. Four generations of terrace surfaces preserved within Freeman Canyon

exhibit a trend of increasing eastward tilt with increasing age (Figure 3-6). There are

several possible mechanisms that may give rise to this observation. Firstly, tilting may

reflect hangingwall subsidence associated with a west-dipping normal fault (CW-MD)

located ~300 m east of the point where the terrace surface elevations converge (Figure 3-

6). If this is indeed the case, we calculate a minimum vertical slip rate of 0.3 mm/yr for

this west-dipping fault based on a maximum age of 200 ka for the Qft4 surface. This

minimum rate amounts to at least half of the maximum rate derived for the RVF over the

last 188 ka (0.6 mm/yr; Berry, 1997), suggesting that a significant amount of Late
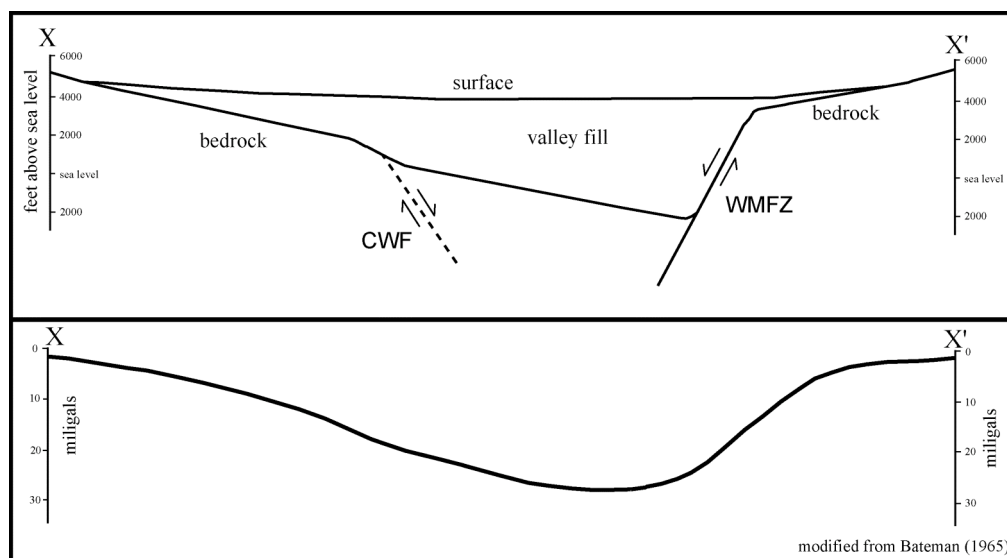
Figure 3-9. Interpreted gravity profile of northern Owens Valley adjacent to the Coyote Warp illustrates the asymmetric nature of the underlying basin structure. The CWF is an inferred fault.

Pleistocene extension is likely accommodated on west dipping structures along the eastern margin of the Coyote Warp. Furthermore, if the abandonment of the Qft2 surface does indeed correlate with that of the youngest Owens River terrace (15-25 ka), the estimated Late Pleistocene slip rate of 0.4-0.7 mm/yr (based on a projection of the Qft2 surface to the CW-MD fault) compares well with Berry's (1997) Late Pleistocene rate (0.4-1.0 mm/yr) for the RVF.

If we assume that east-west extensional stress is equally distributed along northern Owens Valley, our inferred rate for the west-dipping fault (CW-MD) along the Coyote Warp implies that extension on this fault is a relatively recent occurrence, possibly through the redistribution of slip from the deceased CWF. This implication is drawn simply from the idea that, given two primary faults (CW-MD fault and RVF) exhibiting comparable slip rates over a similar period of time, yet significantly different amounts of displacement (meters vs. kilometers), there exists a slip deficit associated with smaller fault, which in an area of uniform extensional stress distribution, must have been previously accommodated on an adjacent structure. In this regard, we suggest that this previous structure was the CWF.

A second mechanism for the observed tilts in Freeman Canyon may relate to far-field basin subsidence concentrated along the eastern margin of the present asymmetric graben. In this regard, continued subsidence along the WMFZ might impart some small amount of hangingwall flexure, and thus tilt, to the Freeman Creek terraces. However, given the proximity of the terraces to the WMFZ (~10 km), we would expect this mechanism to contribute only a small component of tilt to the Freeman Canyon terraces. Lastly, we note that the apparent tilt of these surfaces may reflect some climatic

component of terrace formation. However, given the consistent and pronounced

divergence of slope with increasing age, and the close spatial relation of these surfaces to

active faulting, we suspect any climatic influence is superseded by tectonism.

Basin Development

The present asymmetric configuration of Owens Valley in the vicinity of the

Coyote Warp (Figure 3-9) indicates that the average displacement rate of the CWF has

been outpaced by that of the WMFZ on a timescale comparable to the age of the basin

(i.e. averaged since at least the Late Pliocene). Two simplified scenarios of basin

evolution can explain this apparent mismatch in long-term displacement rates. In the first

scenario, displacement rates for both faults were comparable in the early stages of basin

development with the displacement rate along the CWF either slowing or ceasing when it

intersected the plane of the WMFZ (Figure 3-10). In this scenario, a symmetric graben

bounded by antithetically dipping normal faults initially developed; however, because

faulting nucleated with a spacing that was less than the critical spacing, the initial graben

developed a pronounced asymmetry upon fault intersection and subsequent failure of the

CWF. The early stage of this scenario is analogous to the present day configuration of

the RVF and WMFZ, where, given their wide berth, both faults remain active along a

more or less symmetric graben (Figure 3-3B).

The only requirement for the formation of an asymmetric graben, however, is that

displacement on one side of the graben far exceeds that of the other. This can occur as a

consequence of one fault growing faster than, or nucleating later than another, or simply

because an antithetically dipping fault does not exist. Thus, for the second scenario, there

is no requirement to invoke the CWF, as the basin here may have initially developed as a
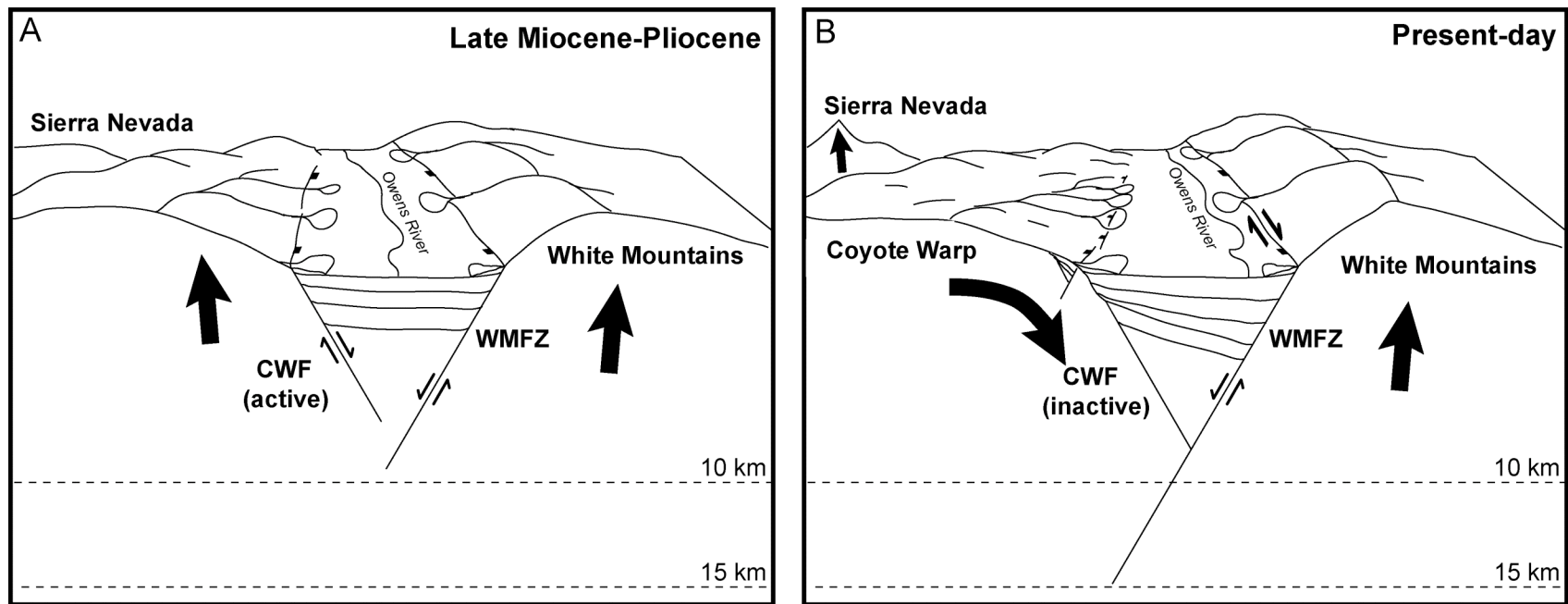
Figure 3-10. Conceptualized evolution of northern Owens Valley and the Coyote Warp. Early extension accommodated on both the CWF and the WMFZ gave rise to an initially symmetric graben. The basin began to grow asymmetrically once the CWF propagated into the plane of the WMFZ. The Coyote Warp presently responds to normal displacement concentrated along the WMFZ.

truly asymmetric graben with displacement being accommodated on only one fault, the WMFZ. However, it is unlikely that subsidence along the WMFZ alone could result in the great relief of the Coyote Warp relative to the adjacent valley (~2 km). In this regard we favor the former scenario.

We note that despite uncertainty regarding the existence of the CWF, the latter model of asymmetric growth is applicable to modern-day basin development in this portion of Owens Valley. This interpretation, espoused by Pinter (1995), suggests that basin development is driven only by normal displacement on the WMFZ. The available geomorphic evidence regarding present-day range-front fault activity along both the Coyote Warp and WMFZ supports this interpretation (Figure 3-10; Table 3-3).

Normal Faulting and the Owens Valley Fault Zone

The BMF and OVFZ section helps illustrate the relationship between the pre-existing normal fault geometry associated with the Sierra Nevada range-front and the distribution of dextral shear within this portion of northern Owens Valley (Figure 3-3B and Figure 3-11). The OVFZ is largely characterized by dextral shear, however, examination of rupture from the 1872 Owens Valley earthquake indicates a coseismic displacement ratio of 6:1 for dextral versus normal displacement (Beanland and Clark, 1994). Because the OVFZ is younger than the range-front normal fault system (e.g. Bateman, 1965), it would be expected to displace any pre-existing normal fault planes such that they would become inactive.

From our analysis, the observed spacing between the BMF and the OVFZ (~11 km) appears sufficient for continued activity on the BMF without intersection with the OVFZ (Figure 3-3B). The steep dip (>60°) and fresh appearance of the bedrock scarp
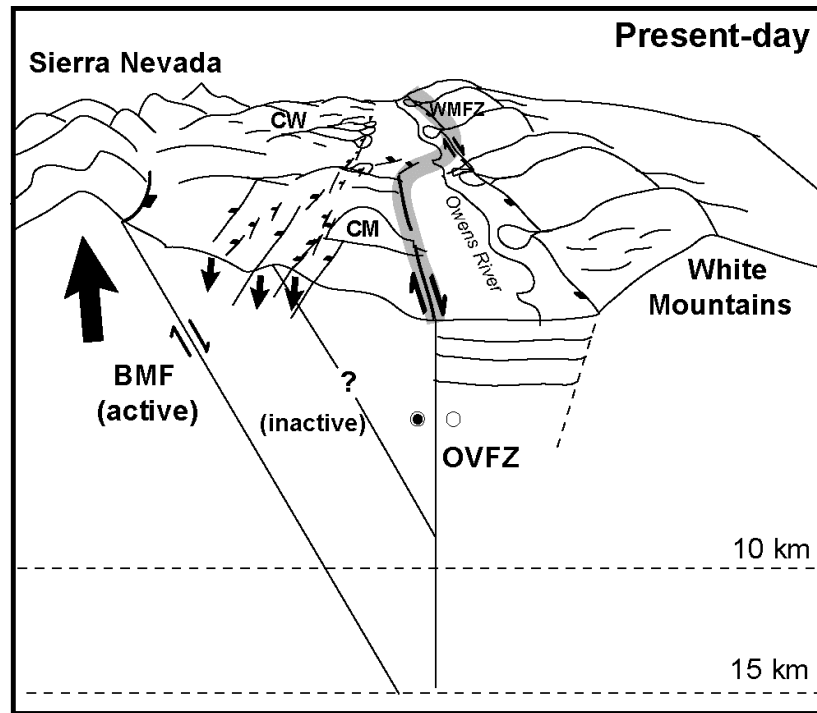
Figure 3-11. Conceptualized model illustrates the relationship between the BMF and the OVFZ. The BMF, a segment of the SNFF system, and the OVFZ do not appear to intersect within the seismogenic layer. However, a several lines on evidence (see text) suggest a previous segment of the SNFF, situated east of the BMF, may have been truncated by the OVFZ. Grey line illustrates the path of dextral shear within northern Owens Valley. Shear is presently transferred from the OVFZ to the WMFZ near the southeastern margin of the Coyote Warp

associated with the BMF (Figure 3-8) fit well with this interpretation. We note that in order for the BMF to intersect the OVFZ at <15 km depth, and thus become locked, it requires a dip of <57°. For intersection with the OVFZ at <10 km requires the BMF to dip at <47°.

Several geologic observations shed light on the relationship between the Sierran range-front and the OVFZ. These observations include the similarity of the spacing between the BMF and the OVFZ (~11 km) to the predicted critical spacing for these faults (~10 km), the lack of a significant east-dipping range-front fault north of the BMF, and the spatial correspondence between the absence of a range-front fault (and the onset of several west-dipping normal faults) with the prominent westward step of the OVFZ near the Poverty Hills. One possible explanation for these observations is that an earlier version of the Sierran range-front fault in the vicinity of the BMF was previously truncated by the OVFZ. In this regard the BMF may represent a re-established version of the Sierran frontal fault west of its original position. If a previous version of the frontal fault did become inactive by this mechanism, new faults would be required to nucleate in order to accommodate ongoing extension. If these new faults nucleated close to the OVFZ (i.e. < 11 km), they too would eventually become truncated at depth. A viable east-dipping range-front fault could only be reestablished if it nucleated at a distance approximated by the predicted critical spacing (Figure 3-11). We suggest this explains why the spacing between the BMF and the OVFZ (~11 km) very narrowly exceeds the predicted critical spacing of ~10 km.

Lastly, we suggest that the asymmetric development of the basin adjacent to the eastern margin of the Coyote Warp here has in turn influenced the spatial distribution of

dextral shear associated with the greater OVFZ-WMFZ. The asymmetric graben structure of this portion of northern Owens Valley, which developed after the CWF became inactive (Figure 3-10), effectively imposes a kinematic restraint on the northward propagation of dextral shear on the OVFZ. The WMFZ, which is characterized by continued activity, provides a path of least shear resistance for crustal shear associated within this area, and thus facilitates the eastward transfer of dextral shear from the northern tip of the OVFZ (Figure 3-11).

Conclusion

Down-dip intersection between conjugate faults plays an important role in normal fault growth, and therefore has implications for landscape evolution in tectonically active areas. The depth of down-dip intersection of conjugate normal faults is predicted here using simple geometric relations that take into account fault dip and the horizontal spacing between faults. These predictions, when applied to crustal scale normal faults, and put in the context of an inferred seismogenic thickness, place constraints on the spatial and temporal evolution of large fault controlled structures.

Our analysis of basin width and fault geometry in northern Owens Valley suggests that the unique nature of the Sierran range-front here can be explained in the context of a failed conjugate fault system. Simplified cross-sections that take into account fault spacing and dip indicate that the CWF and WMFZ intersect well above the inferred seismogenic base. This has resulted in the inactivity of the CWF, and is reflected by the lack of an active east-dipping range-front fault, the subdued topographic character of the Coyote Warp, and the asymmetric structure of the adjacent basin. A similar cross-section for the RVF and WMFZ indicates that range-front faulting to the

north of the Coyote Warp does not intersect within the brittle upper crust. This interpretation is corroborated by Late Pleistocene activity associated with each of these faults.

The BMF segment of the Sierran frontal fault system and the OVFZ do not intersect within the brittle upper crust. Given its youthful character, however, and its positioning on the range-front, the BMF may have shifted westward as a result of intersection at an earlier time. The lack of significant range-front faulting immediately to the north of the BMF, as well as the preponderance of distributed small west-dipping normal faults, may be an indication of previous intersection at depth. Moreover, the development of the asymmetrical graben structure of northern Owens Valley due to the death of the CWF restricts the continued northward propagation of shear along the OVFZ. This may explain why surface rupture associated with the 1872 Owens Valley earthquake propagated to, but not beyond the southeastern margin of the Coyote Warp. Dextral shear is subsequently transferred east to the WMFZ, as its oblique nature provides a path of least resistance for crustal shear in this area.

Chapter 4

Temporal variation in extensional strain rate within northern Owens Valley, California

Abstract

Understanding the pace and tempo of fault slip and its spatial distribution can yield insight into the geodynamics of lithospheric deformation. Here we evaluate the role of distributed strain across the northern Owens Valley based on summed displacements measured across a population of relatively small (< 40 m throw) normal faults. These faults extend through several geomorphic units spanning an age range from ~760 ka to ~15 ka. Geologically based vertical slip rates from northern Owens Valley, California, reflect a two to three-fold increase in extension from Middle (0.31 mm/yr) to Late Pleistocene (0.54-0.91 mm/yr) time. These results, which are in agreement with a similar change in vertical slip rates in nearby Fish Lake Valley, show an inverse correlation with dextral shear rates from Owens and Fish Lake valley since Middle Pleistocene time. We propose this relationship reflects a change in the orientation of regional shear from NNW to NW over the same period. Furthermore, our results indicate that significant extensional deformation may occur on distributed arrays of small faults, suggesting studies that focus primarily on the largest faults within a fault zone may underestimate the total inventory of geologic slip. Moreover, our results contribute to the compilation of an extensional slip budget for northern Owens Valley that is in agreement with geodetic based estimates.

Introduction

Knowledge of deformation rates over multiple timescales provides the foundation

on which to base interpretations of kinematic evolution in tectonically active regions.

Analyses of offset geomorphic markers have traditionally provided a key measure for

determining long-term geologic fault slip rates; however, the resolution of geologic

techniques is such that important variability in deformation rates may be masked,

especially when the age of a geologic marker is significantly greater than the timescales

over which temporal variations may occur. Recent advancements in space based

geodetic measuring techniques, notably InSAR and GPS, have drawn attention to the veracity of geologic slip rates by greatly increasing our understanding of the timescales over which variations in deformation rates may occur (e.g. Peltzer et al., 2001; Bennett et al., 1999; Dixon et al., 2000). This new understanding raises fundamental questions concerning how geologic datasets relate to the continuum of deformation in kinematically evolving regions. Particularly, in regions where the deformation field is rapidly evolving, it is often unclear how averaged long-term ($>10^5$ yrs) geologic slip rates relate to those measured over relatively shorter timescales ($<10^5$ yrs). Geologic observations concerning temporal changes in the magnitude of deformation often remain elusive due simply to the lack of reliable geomorphic markers at a specific location from which multiple estimates of slip rate can be obtained. Furthermore, it is often unclear how geologic slip rates relate to the overall deformation field associated with a given fault. For example, implicit in published studies concerning geologic slip rates is the assumption that the cumulative displacement observed on a given fault is representative of the total deformation with which that fault is associated. However, in reality, large faults (lengths $>>10^4$ m), which are typically the focus of such studies, may only accommodate a portion of the total strain, especially when deformation is distributed on nearby arrays of small faults.

Here we examine a large population of small normal faults in order to better characterize the spatial and temporal distribution of extensional strain within the western portion of the Eastern California Shear Zone (ECSZ). The faults examined here have developed within several distinct Middle to Late Pleistocene age geomorphic surfaces, which each record a discrete (time) interval of the same protracted extensional event. Based on our analysis, we present new geologic data that highlight both time dependent

changes in the rate of extensional deformation within Owens Valley, as well as the contribution of small faulting to regional strain.

Study Area

The study area is located in northern Owens Valley in eastern California (Figure 4-1A). Owens Valley is the western-most of a series of large extensional basins north of the Garlock fault that provide structural pathways for the large dextral shear faults of the ECSZ. Together these dextral faults accommodate ~25-30% of the North-American Pacific plate related shear (e.g. Bennett et al., 1999; Dixon et al., 2000; Miller et al. 2001). Deformation within Owens Valley is thus largely characterized by right lateral shear (Savage and Lisowski, 1995; Beanland and Clark, 1994); however, a component of east-west extension is evident from numerous Middle Pleistocene to Holocene age normal fault scarps. Normal displacement within northern Owens Valley is primarily concentrated along the range-bounding faults of the Sierra Nevada (Bateman, 1965; Bryant, 1984; Berry, 1997) and the right-oblique White Mountain fault zone (WMFZ) (Stockli et al., 2003; Kirby et al., 2006); however, a significant number of intra-valley normal faults are broadly distributed between these two larger fault zones (Bateman, 1965; Sheridan, 1975; Dawers et al., 1993; Pinter, 1995). The intra-valley fault population, which has developed within several distinct geomorphic surfaces, is related to activity on the larger range-bounding faults, and can thus be used to determine a measure of the relative magnitude of crustal deformation in this part of Owens Valley (Sheridan, 1975; Pinter and Keller, 1995; Pinter, 1995).

Volcanic Tableland

The Volcanic Tableland (VT), the oldest and most extensively faulted surface, is
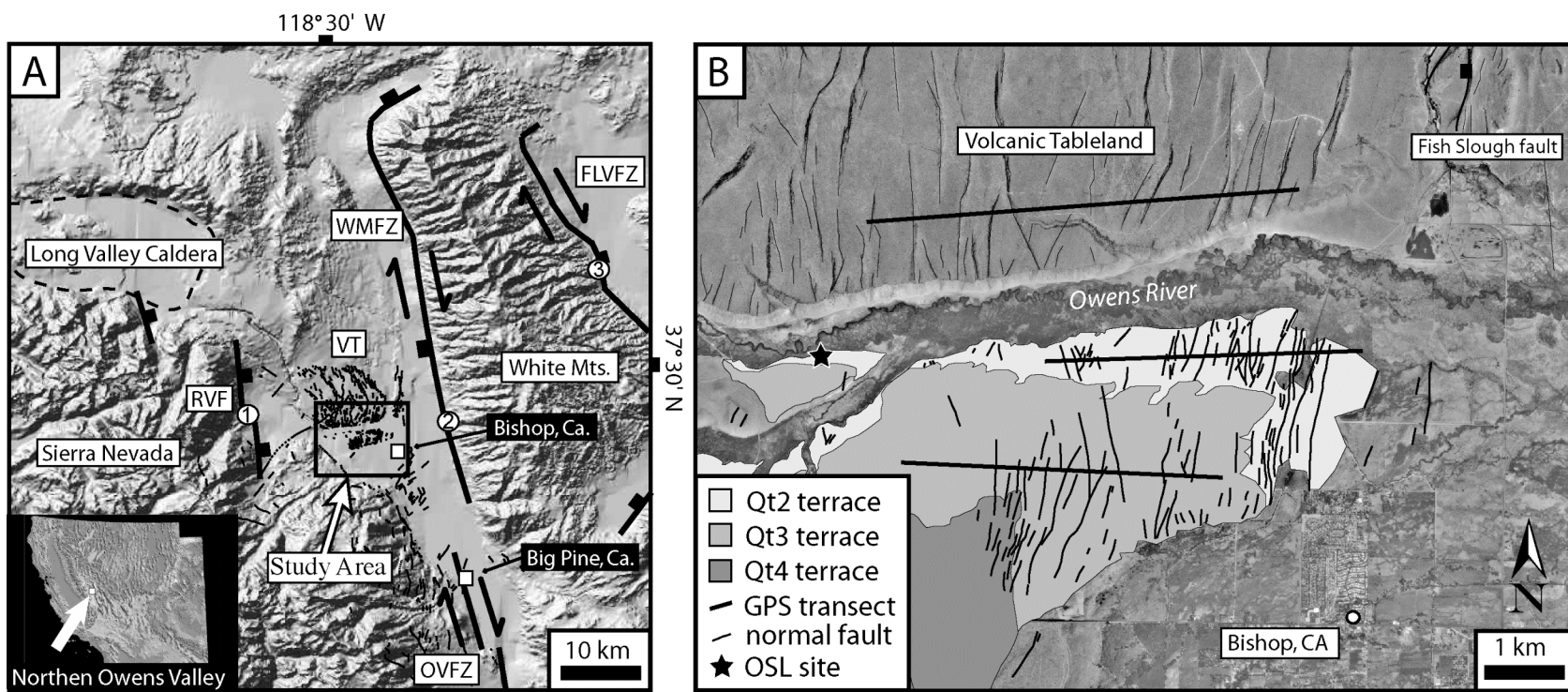
Figure 4-1 A) Location of study area in northern Owens Valley, California. Thick lines indicate major faults. Thin lines indicate intra-valley normal faults. Numbers indicate the site locations for fault slip rate estimates from (1) Berry (1997), (2) Kirby et al. (2006), and (3) Reheis and Sawyer (1997). **B)** Heavy east-west trending lines indicate locations of DGPS transects. Thin lines indicate normal faults with variable east and west dips. Star denotes location of OSL sample site. White Mountains fault zone – WMFZ; Owens Valley fault Zone – OVFZ; Fish Lake Valley fault zone – FLVFZ; Round Valley fault – RVF; Volcanic Tableland – VT.

composed of the Bishop Tuff. It is characterized as a broad, southward-sloping anticlinal feature, which extends as a continuous sheet from the Long Valley caldera to near the town of Bishop (Figure 4-1B). The Bishop Tuff itself is an extensive, ~150 m thick deposit of welded to unwelded rhyolitic tuff (Gilbert, 1938; Bateman, 1965), which was emplaced ~760 ka (Sarna-Wojcicki et al., 2000) during the cataclysmic eruption of the Long Valley caldera. The brittle character of the Bishop Tuff provides an ideal medium for preserving deformation as its resistant upper surface is inferred to have undergone very little erosion since emplacement (Gilbert, 1938; Bateman, 1965; Sheridan, 1975; Dawers et al., 1993). This interpretation is bolstered by the presence of numerous relatively intact fumarole mounds on the surface of the VT (Bateman, 1965).

Fluvial Terraces

Several distinct fluvial (fill) terrace surfaces have been preserved by the Owens River system through the incremental incision and subsequent abandonment of portions of its floodplain (Figure 4-1B). The abandonment ages of these surfaces (Qt2, Qt3, and Qt4) have previously been correlated to the waning stages of the Tioga, Tahoe, and pre-Tahoe glaciations, respectively, of Sierra Nevada Mountains (Pinter et al., 1994). These correlations are based primarily on comparisons of clast weathering rinds and soil descriptions from the Owens River terraces and the glacial moraines of Pine Creek (Site 1, Figure 4-1A), and are supplemented with a radiocarbon age of 7170 ± 100 yr B.P., which was derived from carbonate clast coatings from the Qt2 terrace surface (Pinter et al., 1994). Because few solid numerical age constraints exist for the moraines of Pine Creek (e.g. Birkeland et al., 1991; Bierman and Gillespie, 1994), however, and due to the uncertainty involved in the relative age correlations, as well as the potential for

contamination of the carbonate age source (Pinter et al., 1994, Pinter and Keller, 1995), these initial terrace age constraints are regarded as tentative.

Faulting

The fault map for this study was compiled from Bateman (1965) and Bryant (1984), and from field and aerial photo (1:40,000 scale) mapping. Numerous fault scarps exhibiting normal displacement are preserved within the VT and the Qt2 and Qt3 terrace surfaces (Figure 4-1B). These faults strike to the north and exhibit both east and west facing scarps. Despite uncertainty in fault dip, especially for those faults within the terrace units, our overall preferred dip estimate of 70° is in relative agreement with dips inferred from previous study on the VT (Bateman, 1965; Dawers et al., 1993; Pinter, 1995). Fault scarps on the Qt2 and Qt3 terrace surfaces exhibit similar strike, and in some cases, project directly in line with scarp terminations along the truncated southern margin of the VT (Figure 4-1B). However, no visible faulting is observed on the Holocene floodplain of the Owens River, which lies immediately south of the VT and north of the Qt2 terrace. The lack of measurable fault offset here is due to recent reworking of alluvial material by the Owens River.

Slip Rate Determination

We calculated vertical and extensional slip rates for a total of three east-west transects measured across the Qt2, Qt3 and VT surfaces (Figure 4-1B). Elevation data were collected at one-meter intervals using a differential global positioning system (DGPS). Measurement error is estimated to be <0.5 m. Fault throw (vertical displacement) was estimated by differencing the elevation points from the footwall crest and the hangingwall trough. Throw and an inferred fault dip of 70° were used to

calculate heave (horizontal extension) (Table 4-1). The total extension measured for a given transect is equal to the sum of the heave contributions from each sampled fault. We calculated cumulative vertical and extensional slip rates based on both the inferred age of each surface (long-term rate), and the time interval between surface ages (interval rate) (Table 4-1). By calculating the interval slip rate, the slip rate since emplacement of the latter surface is extracted from the long-term rate.

In a conservative effort, we present our findings in the context of age ranges after those complied from various Sierra Nevada glacial studies which we infer to bracket the ages of terrace abandonment (Table 4-1 and 4-2). We used several published age constraints for the upper and lower bounds of the Tioga glaciation to infer a limiting age range of 15-25 ka for the Qt2 surface (Table 4-2). In order to test the validity of this inferred age range, we submitted sediment samples from the Qt2 terrace for optically stimulated luminescence (OSL) analysis. Due to the lack of solid age constraints for the Tahoe glaciation, we infer the limiting ages for the Qt3 surface to range from the end of the pre-Tahoe (~130 ka) to the end of the Tahoe (~55 ka) glaciation (Phillips, et al. 1990; Fred Phillips, written communication; Pinter et al., 1994).

Results

The one-dimensional transects used in our analysis sampled 19 scarps on the VT, and 10 scarps each on the Qt3 and Qt2 surfaces (Figure 4-1B and 4-2, Appendix E). The sum of sampled throws of 238.6 m for the VT, 41.8 m for Qt3, and 13.6 m for Qt2 yield cumulative long-term vertical slip rates of 0.31 mm/yr for the VT, 0.32-0.76 mm/yr for Qt3, and 0.54-0.91 for Qt2. The resulting cumulative heaves of 86.8 m for the VT, 15.2 m for Qt3, and 5.0 m for Qt2, yield extension of 1.6% for the VT, 0.4% for Qt3, and

TABLE 4-1. TRANSECT ATTRIBUTES AND COMPLIED SLIP RATES

study	location	age (ka)	transect length (m)	faults sampled	total throw (m)	total heave (m) (70° dip)	vertical slip rate (mm/yr)	% extension	extension rate (mm/yr)
this study	VT	760 [§]	5300	19	238.6	86.8	0.31	1.6	0.11
		760 - 130 (630)*					0.31[†]		0.11[†]
		760 - 55 (705)*					0.28[†]		0.10[†]
	Qt3	130 - 55	3900	10	41.8	15.2	0.32 - 0.76	0.4	0.12 - 0.28
		130 - 15 (115)*					0.25[†]		0.09[†]
		55 - 15 (40)*					0.71[†]		0.26[†]
	Qt2	25 - 15	3900	10	13.6	5.0	0.54 - 0.91	0.1	0.20 - 0.33
		21 ± 3.3 [#]					0.56 - 0.77		0.21 - 0.28
Reheis and Sawyer (1997)	FLVFZ (Dyer sec.)	760					0.18 - 0.59 0.13 - 0.61		
		360 - 190					0.29 - 1.1		
		75 - 50					1.2 - 3.6 0.47 - 1.4		
		8 - 5					1.6 - 5.2		0.6 - 1.9
Berry (1997)	RVF	15 - 20					0.4 - 1.0		0.15 - 0.36
Kirby et al, 2006	WMFZ	760 72 ± 15					0.15 - 0.25 0.1 - 0.2		0.15 - 0.25 0.1 - 0.2

[§] Ar^{40}/Ar^{39} dating the Bishop Tuff yield ages of 757.7 ± 1.8 ka (basal pumice) and 762.2 ± 4.7 ka (overlying tuff) (Sarna-Wojcicki et al., 2000)

* age interval used to calculate interval slip rate. younger rate(s) are extracted from the long-term rate

[†] interval rate = (cumulative displacement of older unit - (younger rate x time interval of younger rate)) / time interval of older rate

[#] preferred OSL age for a sediment sample obtained from ~2 meters below the Qt2 terrace surface (see Figure 4-1B)

TABLE 4-2. GLACIAL AGE CONSTRAINTS IN THE SIERRA NEVADA

Glacial Stage	age constraints (ka)	study	ages inferred from
Tioga	15 - 30.5	Bischoff and Cummins (2001)	rock flour in Owens Lake core
	18.6 +/- 1.2	James et al. (2001)	cosmogenic ^{10}Be and ^{26}Al dating of erratics
	>14 - 15	Clark and Gillespie (1997)	radiocarbon dating of lake cores
	15 - 28	Benson et al. (1996)	^{18}O, TOC, TIC, mag. suscep. in core sediment
	16 - 25	Phillips et al. (1996)	cosmogenic ^{36}Cl dating of moraine deposits
	>15.5 - 16.2	Mensing (2001)	pollen and algae from Owens Lake core
	>14.8	Porinchu et al. (2003)	insect abundance in high altitude lake core
	>17 - 19	Koehler and Anderson (1995)	vegetation changes in packrat middens
	<25.2 +/- 2.5	Bursik and Gillespie (1993)	RD techniques (e.g. morphology, weathering)
	20.4 - 23.1	Phillips et al. (1990)	cosmogenic ^{36}Cl dating of morraine deposits
Tahoe	68.1 - 78.0	Bischoff and Cummins (2001)	rock flour in Owens Lake core
	55.9 - 65.8	Phillips et al. (1990)	cosmogenic ^{36}Cl dating of morraine deposits
	< 119 +/- 7	Gillespie (1988)	dated basalt
Pre-Tahoe	133 - 218	Phillips et al. (1990)	cosmogenic ^{36}Cl dating of morraine deposits
	>131 +/- 10	Gillespie (1988)	dated basalt

Figure 4-2. Topographic profiles obtained from DGPS transects across the VT, Qt3, and Qt2 surfaces (see Figure 4-1B for transect locations). Sampled fault scarps are indicated by numbers

0.1% for Qt2. The calculated long-term net extension rates are 0.11 mm/yr for the VT,
0.12-0.28 mm/yr for Qt3, and 0.20-0.33 mm/yr for Qt2 (Table 4-1). The two sediment
samples taken from the Qt2 terrace (Figure 4-1B) yielded OSL ages of 6.2 ± 1.8 ka and
21.0 ± 3.3 ka (Appendix F). Slip rates derived from the latter OSL age (0.56-0.77
mm/yr) agree well with the rate estimate derived using the age range inferred from
previous correlation of the Qt2 surface with the Tioga glaciation (0.54-0.91 mm/yr).

Discussion

Geologic slip rates averaged over relatively long time intervals ($>10^5$ yrs) often
mask temporal variations in deformation. This is attributed to the episodic nature of
available geologic constraints, which often leave large gaps in the characterization of past
deformation rates. Geologic slip rates are typically based on the assumption that, despite
the short-term variability expected over the course of one or more earthquake rupture
cycles, averaged long-term rates accurately characterize a given deformation field.   In
kinematically dynamic regions, however, such as nascent crustal block boundaries, where
the deformation field is rapidly evolving ($<10^5$ yrs), relatively long-term ($>10^5$ yrs) rates
derived from geologic data may be in error.

Slip History

Our results suggest that the rate of extensional deformation within northern
Owens Valley has undergone a significant, yet previously unrecognized, increase since
Mid-Pleistocene time (Table 4-1). Depending on the inferred age of the Qt3 surface, this
increase occurred either before or after abandonment of the Qt3 surface. Within age
uncertainty (~130-55 ka), the long-term vertical slip rate derived from the Qt3 surface is
estimated to be 0.32-0.76 mm/yr. If the Tahoe (~55 ka) correlation of Qt3 is strictly

adhered to, the long-term (0.76 mm/yr) and interval (0.71 mm/yr) slip rates imply that the extension rate increase preceded abandonment of the Qt3 surface. These vertical slip rates are twice the rates derived from the Mid-Pleistocene VT (0.31 and 0.28 mm/yr). However, if the pre-Tahoe age (~130 ka) is valid, the long-term (0.32 mm/yr) and interval (0.25 mm/yr) rates from the Qt3 surface nearly match the rate since the Mid-Pleistocene (0.31 and 0.28 mm/yr). Nonetheless, the vertical slip rate determined from the Qt2 surface, based on both the correlation age range (0.54-0.91 mm/yr) and confirmed with a new OSL age (0.56-0.77 mm/yr), is two to three times that of both the long-term and interval slip rates calculated for the VT (0.31 and 0.28 mm/yr). Despite greater uncertainty in the age of the Qt3 surface, comparison of results from the VT and Qt2 surfaces suggests that a significant increase in the rate of extension occurred within northern Owens Valley since Mid-Pleistocene time.

We note there is some uncertainty regarding the initiation age of faulting on the VT; however, based on the lack of significant incision by fault-cut paleo-river channels within the VT, which presumably represent initial short-lived versions of the reestablished (post-Long Valley event) fluvial system, we suggest that faulting initiated relatively close (in time) to the emplacement of the VT such that early versions of the Owens River were defeated before a significant fluvial system could be established here. Note, that if we allow 100 ka after the formation of the VT before faulting initiated, the inferred vertical slip rate increases only slightly to 0.36 mm/yr. This rate is still significantly lower than the Late Pleistocene rate.

Corresponding Slip Histories

Several distinct geomorphic markers along the Dyer section of the Fish Lake

Valley fault zone (FLVFZ), located east of Owens Valley, provide a slip rate history indicating that long-term vertical slip rates increased by a factor of at least two or more from Mid-Pleistocene to Holocene time (Table 4-1). The vertical slip rate since the Mid-Pleistocene (0.13-0.61 mm/yr), based on ~760 kyr Bishop ash amounts to, at most, one-third of the Holocene rate (1.6-5.2 mm/yr). Moreover, this rate amounts to, at most, one-half of the rate since deposition ceased on an inferred Tahoe age (75-50 ka) alluvial fan (1.2-3.6 mm/yr). While Reheis and Sawyer (1997) present two vertical slip rates based on the 75-50 ka age fan, we assume the higher rate (0.13-0.61 mm/yr; Table 4-1) is a better representation of the actual rate, as it is more likely that slip is under-accounted for (due to slip on subsidiary faults) than over-accounted for.

Agreement in the general trend of increasing vertical slip rates, both in Owens Valley and on the Dyer section of the FLVFZ, suggests these disparate locations may be tectonically linked, and thus likely reflect similar changes in regional kinematics. Kirby et al. (2006) came to the same conclusion based on a comparison of dextral slip rates from the WMFZ (Site 2, Figure 4-1A) and FLVFZ. They suggest that a significant decrease in the dextral slip rate on the WMFZ during Middle-Late Pleistocene time mimics a decrease in dextral slip on the FLVFZ over the same interval.

It thus stands to question why extensional slip rates observed in northern Owens Valley (this study) and on the Dyer section of the FLVFZ (Reheis and Sawyer, 1997) exhibit an inverse correlation with respect to dextral slip rates (Kirby et al., 2006) over the same interval of time? We acknowledge that the similarity in vertical slip rate variation in these areas may be coincidental, yet, because of the corresponding link in dextral slip variation, it is likely these rates reflect regional tectonic variation.

Coexistence of these two modes of active deformation (normal and dextral) suggests they are manifest from the same driving stress, and thus each is expected to experience coeval, though not necessarily concordant changes. In general, slip within this part of the ECSZ appears to be partitioned based on fault strike, as north-trending faults tend to accommodate a larger proportion of extension than more northwest-trending faults, which accommodate primarily dextral shear.

The contrast in rate variations (i.e. normal increase vs. dextral decrease) may be explained by a counter-clockwise rotation in the orientation of regional shear. Such a change would facilitate more efficient partitioning of normal slip on north-striking faults, and lead to a corresponding reduction in dextral slip, since the large right-lateral faults would be expected to fall slightly out of favor with respect to the orientation of regional shear. If this hypothesis is valid, then similar trends in slip histories are expected throughout the region. Interestingly, the orientation of average oblique-slip vectors for the WMFZ, which incorporate both normal and dextral offset, indicate a shift in shear orientation since the Mid-Pleistocene (Kirby et al., 2006). Average oblique slip vectors since ~760 ka trend toward N10^o-20°W, whereas, inferred slip vectors since 72 ±15 ka trend toward N20^o-40°W.

Implications for Geologic vs. Geodetic Extension Rates

Compilation of geologic slip rates over a broad area facilitates a comparison between geologic and geodetic based extension estimates. If we extrapolate the data from the youngest surface, Qt2, to estimate the extension rate over a distance that is twice the length of the original transect (in order to approximate the width of faulting within the VT), we estimate a minimum Late Pleistocene extension rate of ~0.4-0.6 mm/yr between

the valley bounding faults of the Sierra Nevada and WMFZ. This estimate is considered

conservative, given the broad, and relatively even distribution of faulting across the width

of the VT, as well as, the apparent trend of such faulting into the surrounding terrace

units. A summation of published latest-Pleistocene extensional rates for faults within

northern Owens Valley, including the Round Valley fault (~0.2-0.4 mm/yr; Site 1, Figure

4-1A; Berry, 1997), the WMFZ (~0.1-0.2 mm/yr; Site 2, Figure 4-1A; Kirby et al., 2006),

and this study (extrapolated to ~0.4-0.6 mm/yr), yields a valley perpendicular extension

rate of ~0.7-1.2 mm/yr. This estimate is in remarkable agreement with the geodetic

extension rate of 1.0 ± 0.3 mm/yr determined for the breadth of Owens Valley between

Owens Lake and the town of Bishop from Savage and Lisowski (1995). Furthermore,

space-based geodetic data presented by Dixon et al. (2000) allow for 1.8 ± 1.4 mm/yr of

extension between sites in the central Sierra Nevada and Ely, Nevada, with much of the

extension being accommodated in Owens Valley and Fish Lake Valley. A summation

that includes extension from Owens Valley and the Dyer section of the FLVFZ (~0.6-1.9

mm/yr; Site 3, Figure 4-1A; Reheis and Sawyer, 1997) yields an extension rate of 1.3-3.1

mm/yr across Owens Valley and Fish Lake Valley. This estimate overlaps within

uncertainty with the geodetic estimate of Dixon et al. (2000).

Inclusion of distributed faulting within northern Owens Valley indicates that

geological extension rates are commensurate with similarly oriented geodetic rates.

These results suggest that a significant portion (up to ~50%) of Late Pleistocene

extensional deformation within northern Owens Valley is distributed amongst a large

population of relatively small faults, which occur several kilometers away from the main

fault strands used to compile typical estimates of slip rate. In this respect, geologic slip

rate estimates that do not explicitly account for subsidiary faults should be considered partial or minimum estimates. Moreover, these results suggest that missing slip may account for part of the discrepancy between geologic and geodetic rates.

Conclusion

Analysis of a distributed population of small normal faults preserved across several distinct Middle to Late Pleistocene age geomorphic surfaces indicates that the rate of extension within northern Owens Valley has varied with time. A comparison of rates derived from the Mid-Pleistocene VT and the Late Pleistocene Qt2 terrace surface indicate a two to three-fold increase in the rate of extension across the breadth of this part of Owens Valley. The time dependant increase in extension corresponds to a similar increase in nearby Fish Lake Valley, suggesting regional tectonic forcing. The concurrent increase in extensional slip rates and decrease in dextral slip rates within Owens Valley and Fish Lake Valley suggest that the orientation of regional shear may have experienced a counter-clockwise rotation during the Late Pleistocene. Furthermore, our geologic slip budget for extensional deformation across Owens Valley is in agreement with estimates of ground and space based geodetic extensional strain accumulation, suggesting that incorporation of distributed faulting, as well as, better resolution of time variable changes in the magnitude of deformation may help account for discrepancies between geologic and geodetic rates within the ECSZ.

Chapter 5

Constraints on kinematic evolution within the Eastern California Shear Zone

Abstract

Analyses of fault size-frequency distributions yield insights into the mechanisms of strain partitioning within the brittle crust. Such analyses provide a means to relate the number and relative sizes of faults within a population to the specific factors that influence fault growth. Here we present size-frequency data from several distinct fault populations located within the Eastern California Shear Zone (ECSZ). Three of these populations, including a regional scale northeast-striking fault population, and two northeast-striking fault populations localized in northern Owens Valley and the Saline Range, have developed in response to dextral shear transfer between the large dextral fault zones of the ECSZ. We suggest these large dextral faults impose geometric limitations on the maximum size attainable by the intervening northeast-striking normal faults. These limitations are related to the horizontal spacing between the boundary fault zones, and are reflected in the size distributions of the northeast-striking fault populations. These limitations strongly influence patterns of strain distribution within the ECSZ, and help drive the redistribution of slip from the largest constrained faults resulting in an increase in the nucleation and growth of small faults within affected populations. Moreover, a fourth population of north-striking normal faults located within northern Owens Valley exhibits two distinct size distribution forms, power-law and exponential, which characterize distinct fault subsets. These fault subsets offset several age-distinct geomorphic markers, and thus provide a means to analyze changes in strain distribution through time. Our data suggest that the variable size-frequency distributions may be attributed, in part, to the amount of total strain accommodated by each of the fault subsets.

Introduction

Analysis of developing fault populations provides important insights into the

mechanisms controlling the spatial and temporal distribution of strain within the brittle

upper crust. In recent years, examination and characterization of a broad range of

experimental (e.g. Spyropoulos et al., 1999; Clifton et al., 2000; Ackermann et al., 2001),

numerical (e.g. Cladouhos and Marrett, 1996; Cowie and Scholz, 1992; Cowie et al., 1995; Cowie et al., 1998; Hardacre and Cowie, 2003), and natural (e.g. Wojtal, 1996; Ackermann and Schlische, 1997; Gupta and Scholz, 2000a; Scholz et al., 1993; Gross et al., 1997) fault populations has greatly expanded our understanding of how these mechanisms relate to changes in strain distribution. In particular, analyses of fault size-frequency distributions have been used to relate such changes to fault interaction and linkage (Cladouhos and Marrett, 1996; Wojtal, 1996; Gupta and Scholz, 2000a), mechanical layer composition (Davy et al., 1995) and geometry (Wojtal, 1994; Ackermann and Schlische, 1997; Ackermann et al., 2001; Gross et al., 1997), total strain (Spyropoulos et al., 1999, 2002; Gupta and Scholz, 2000a), and fault system geometry (Clifton et al., 2000). Of fundamental value, fault size-frequency distributions provide a straightforward means for characterizing the number and relative sizes of faults within a fault population. In the context of tectonically active regions, this information is useful for strain analysis, and for identifying potential physical constraints on structural and kinematic evolution. Despite the obvious implications for interpretations of tectonic framework, structural and kinematic history, and potential seismic risk (e.g. Clifton and Schlische, 2001), however, this information has been relatively underutilized in examinations of neotectonic settings.

Within the Eastern California Shear Zone (ECSZ) (Figure 5-1), the growing inventory of geologic and geodetic data indicates that strain rates change significantly over a range of temporal and spatial scales (e.g. Dokka and Travis, 1990; Dixon, et al., 2000; Rockwell et al., 2000; Kirby et al., 2006). Comparison of geologic slip rates inferred over markedly different time intervals for individual faults, as well as similar
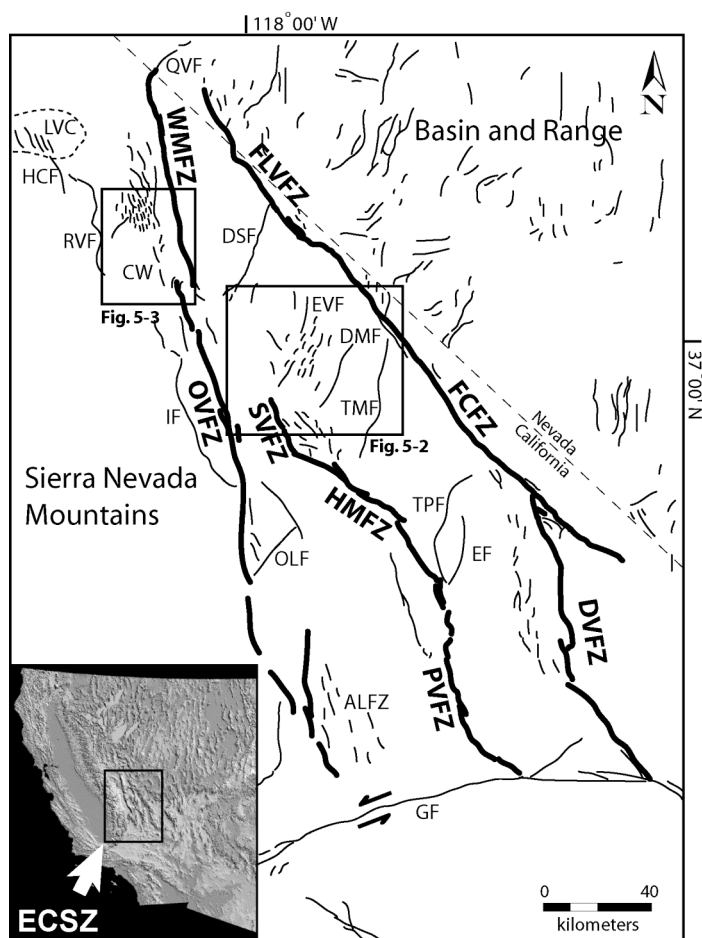
Figure 5-1. Map of Late Cenozoic faults of the Eastern California Shear Zone (ECSZ) north of the Garlock fault (GF) modified from the USGS Quaternary Fault and Fold Database (USGS, 2006). Northeast-striking normal faults within the greater ECSZ include the Emigrant (EF), Towne Pass (TPF), Tin Mountain (TMF), Dry Mountain (DMF), Eureka Valley (EVF), Deep Springs (DSF), Queen Valley (QVF), and Owens Lake (OLF) faults. Dextral fault zones of the ECSZ (bold dark traces) include the Death Valley (DVFZ), Furnace Creek (FCFZ), Fish Lake Valley (FLVFZ), Panamint Valley (PVFZ), Hunter Mountain (HMFZ), Saline Valley (SVFZ), Owens Valley (OVFZ), and White Mountain (WMFZ) fault zones. Black boxes denote the location of the Saline Range (Figure 5-2) and northern Owens Valley fault populations (Figure 5-3). ALFZ – Airport Lake fault zone; CW – Coyote Warp; HCF – Hilton Creek Fault; IF – Independence fault; LVC – Long Valley Caldera; RVF – Round Valley fault..

time intervals for adjacent faults, suggests that such changes occur through the redistribution of slip among existing fault networks (Reheis and Sawyer, 1997; Reheis and Dixon, 1996; Rockwell et al., 2000; Kirby et al., 2006). Cowie et al. (1998) discussed a feedback mechanism among fault populations whereby adjacent faults enhance or retard the activity of neighboring faults over seismic-interseismic ($<10^4$ yrs), as well as geologic timescales ($>10^4$-10^5 yrs). A fundamental implication of this model is that fault slip rates are not stable; rather they may vary significantly in space and time. Similarly, this model suggests that tectonically active regions, which are subject to relatively uniform regional stress, may exhibit marked variability in internal strain rates depending on where and when such rates are sampled. Such a model appears to be broadly consistent with observation in the ECSZ (e.g. Reheis and Sawyer, 1997; Rockwell et al., 2000; Kirby et al., 2006); however, the specific physical mechanisms that influence the distribution of slip there remain poorly understood. In particular, the relationship between strain distribution and constraints on fault growth within the ECSZ has received little attention.

Here we present fault length-frequency data from four distinct normal fault populations within the ECSZ (Figure 5-1) in an effort to elucidate potential spatial and temporal constraints on kinematic evolution. Three of these populations consist of northeast-striking west-dipping normal faults, which have developed in response to slip transfer between prominent zones of dextral shear. These populations appear at both regional (i.e. greater ECSZ; Figure 5-1) and local (i.e. within northern Owens Valley and the Saline Range; Figure 5-2 and 5-3) scales, and are considered here as three distinct, yet genetically related populations. Based on examination of fault size-frequency.
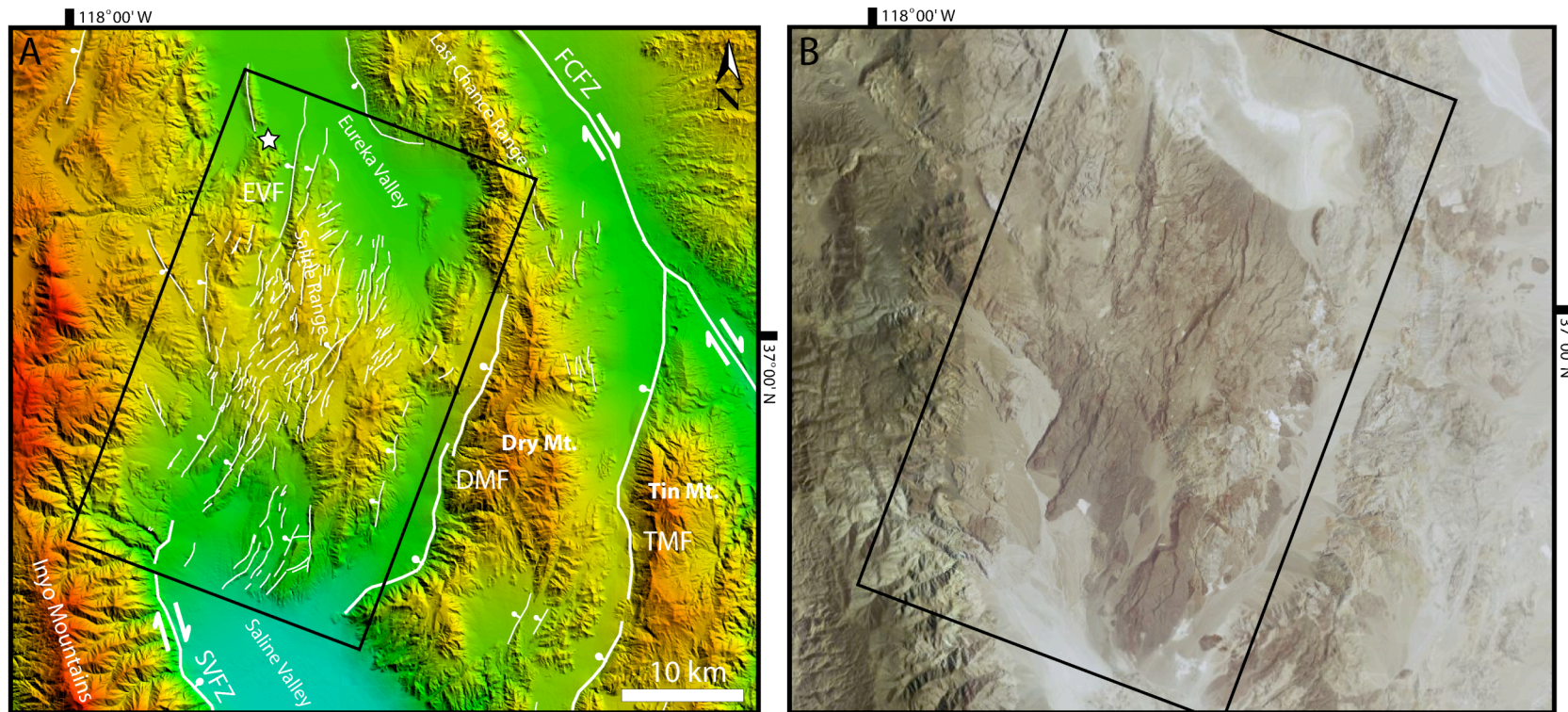
Figure 5-2. **(A)** USGS digital elevation model (DEM) of the Saline Range with a fault map overlay compiled from Ross (1967) Nelson (1971), and Sternlof (1988), and new mapping from USGS DOQQ. Star denotes location of the 1993 M 6.1 Eureka Valley, California earthquake (Peltzer and Rosen, 1995). Dark box denotes the extent of the Saline fault population sample area with dimensions of ~40 km x ~25 km. **(B)** Aerial image of the same area illustrates the exceptional exposure of faulting in this area. SVFZ – Saline Valley fault zone; FCFZ – Furnace Creek fault zone; DMF – Dry Mountain fault; TMF – Tin Mountain fault; EVF – Eureka Valley fault.
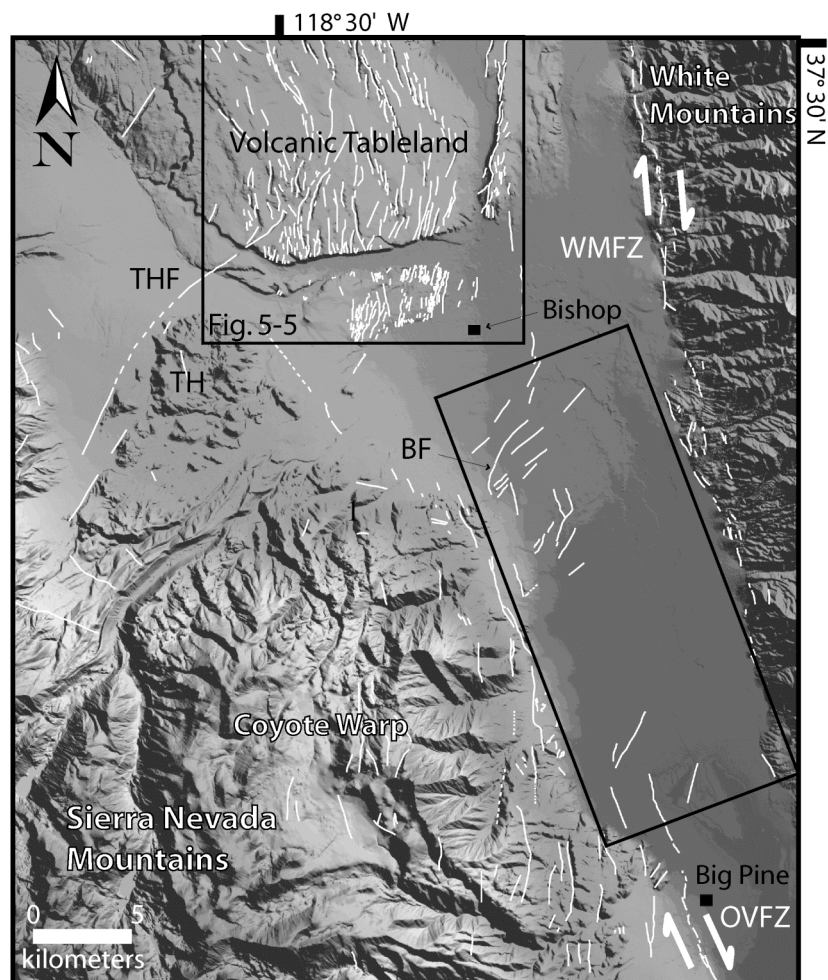
Figure 5-3. Map of Pleistocene faults of northern Owens Valley compiled from Bateman (1965), Bryant (1989), Beanland and Clark (1994), and new field and aerial photo mappping. Northeast-striking faults within Owens Valley, except for the Tungsten Hills fault (THF), are located within southern sample area denote by the northwest trending box. North-striking faults from the Volcanic Tableland and Owens River terraces are located in the northern sample area illustrated in Figure 5-6. OVFZ – Owens Valley fault zone; WMFZ – White Mountain fault zone. TH – Tungsten Hills; BF – Bishop fault

distributions, we suggest that faults within these populations reflect characteristic length scales, which are imposed by the horizontal spacing of the regional north-northwest striking dextral faults. We discuss the implications of such developmental limitation with regard to structural and kinematic evolution within the ECSZ. Furthermore, through examination of a fourth fault population in northern Owens Valley, we delve into temporal changes in strain accommodation as reflected by changes in fault size-frequency distributions. Several Middle to Late Pleistocene age geomorphic surfaces in this area provide a unique opportunity to explore the development of a single normal fault population though time. These surfaces, which preserve numerous north-striking normal faults, record several distinct intervals of fault development, and thus yield potential insight into the manner in which fault size-frequency distributions change through time.

Geologic Setting

Dextral shear within the ECSZ presently accounts for 25-30% of the relative motion associated with the Pacific-North American plate boundary (Dixon et al., 1995; Bennett et al., 1999; Dixon et al., 2000; Gan et al., 2000; McClusky et al., 2001; Miller et al., 2001; Oldow et al., 2001). North of the Garlock fault (Figure 5-1), shear is largely distributed on three north-northwest trending zones of interconnected dextral strike-slip faults: the Death Valley-Furnace Creek-Fish Lake Valley fault zones, the Panamint Valley-Hunter Mountain-Saline Valley fault zones, and the Owens Valley-White Mountain fault zones (Burchfiel et al., 1987; Beanland and Clark, 1994; Dixon et al., 1995; Savage and Lisowski, 1995; Reheis and Dixon, 1996; Reheis and Sawyer, 1997; Dixon et al., 2000; Miller et al., 2001; McClusky et al., 2001; Oswald and Wesnousky, 2002). While dextral shear is presently dominant throughout the region, deformation is

not strictly manifest as such; rather, several distinct extensional fault populations have developed additionally in response to the complex relationship between structure and kinematics. There are two mechanisms for modern-day extensional deformation within this dextral shear dominated region: 1) simple slip transfer between the tips of overlapping dextral faults (Oldow et al., 1994), and 2) slip partitioning whereby transtensional strain is preferentially decomposed into components of both normal and dextral shear (Zoback, 1989; Wesnousky and Jones, 1994; Oldow et al., 2001; Unruh et al., 2003).

The prevailing model for kinematic evolution within the ECSZ suggests that slip is transferred among the existing dextral fault zones via northeast-striking, northwest dipping normal faults (Dixon et al., 1995; Reheis and Dixon, 1996; Reheis and Sawyer, 1997; Lee et al., 2001b). This model is consistent with a generalized right-stepping en echelon dextral shear geometry, where the observed northeast-striking normal faults are analogous to releasing, or extensional steps, which aid in slip redistribution (Oldow et al., 1994; Lee et al., 2001b). The origin of each of the northeast-striking fault populations examined here, including the regionally extensive population of large (>20 km) normal faults, and two populations of more localized, small (<15 km) faults in Owens Valley and the Saline Range, is attributed to this model. The regional scale northeast-striking fault population is evident throughout the ECSZ (Figure 5-1), and includes such prominent faults as the Queen Valley (QVF), Deep Springs (DSF), Dry Mountain (DMF), Tin Mountain (TMF), and Towne Pass (TPF) faults. Each of these structures is associated with well-developed range and basin morphology oriented at a high angle to the regional trend of dextral shear.

North of Saline Valley, and extending from near the northern tip of the Saline Valley fault zone (SVFZ), a similarly oriented population of small normal faults is preserved across a broad basaltic plateau within the Saline Range (Figure 5-2) (Ross, 1967; Sternlof, 1988). The largest of these faults, measuring ~13 km in length, and exhibiting up to ~100 m of throw (vertical displacement), is the Eureka Valley fault (EVF), which exhibited minor surface rupture during the 1993, M 6.1 Eureka Valley earthquake (Massonnet and Feigl, 1995; Peltzer and Rosen, 1995). Given the overall orientation of faulting in this area, particularly with respect to the northern tip of the SVFZ, the Saline Range fault population has likely developed in response to dextral shear transfer from the SVFZ into Eureka Valley, and beyond to the Fish Lake Valley fault zone (FLVFZ) (Reheis and Dixon, 1996) (Figure 5-2).

The third population of northeast-striking normal faults is located within northern Owens Valley (Figure 5-3). This population consists of several northwest-dipping faults that largely outcrop within Late Pleistocene and Holocene fan and alluvial deposits. These faults have developed within a limited radius of the tip-overlap region of the OVFZ and the White Mountain fault zone (WMFZ), suggesting that the kinematic model proposed to describe the similarly styled regional faulting may also be applied to northern Owens Valley (Figure 5-3). While it has been suggested that a significant amount of dextral slip from the OVFZ is likely transferred to the FLVFZ via the nearby DSF (Figure 5-1) (Reheis and Dixon, 1996; Reheis and Sawyer, 1997), some amount of slip clearly continues northward on the WMFZ as evidenced by laterally offset Late Pleistocene markers (dePolo, 1989; Stockli et al., 2003; Schroeder, 2003; Kirby et al., 2006).

The fourth fault population discussed here reflects east–west extension within northern Owens Valley (Figure 5-3). This population consists of north-striking normal faults, which are broadly distributed across the medial portion of northern Owens Valley. These faults are evident within several distinct geomorphic markers within this area (Figure 5-3). The primary marker here, the Bishop Tuff (deposited ~760 ka; Sarna-Wojcicki, 2000), is well known for its exceptional exposure of normal faults (Bateman, 1965; Sheridan, 1975; Pinter, 1995; Pinter and Keller, 1995), and has been the focus of several previous studies concerning fault growth (e.g. Scholz et al., 1993; Dawers et al., 1993; Dawers and Anders, 1995; Ferrell et al., 1999). The average thickness of the Bishop Tuff, which varies with distance from its source at Long Valley Caldera, is estimated to be ~150 m (Gilbert, 1938). Elevation contours along the southern margin of the Volcanic Tableland (VT – the geographic place name for the extensive outcrop of Bishop Tuff within Owens Valley) indicate that it has a minimum thickness of ~120 m. Given the nature of the underlying lithology, which is inferred to be Early Pleistocene alluvium and unconsolidated air-fall ash (Bateman, 1965; Gilbert, 1938), faulting likely nucleated within the Bishop Tuff (Dawers et al., 1993; Dawers and Anders, 1995; Pinter, 1995). Faulting is largely distributed within the Bishop Tuff; however, several faults extend laterally beyond the southern margin of the VT into three distinct fluvial terrace units deposited by the Owens River. These units correlate to past episodes of Late Pleistocene glaciation (Pinter et al., 1994), and thus record much younger intervals of deformation than that of the VT.

Fault Size-Frequency Distributions

Fault size-frequency data are commonly displayed in graphical form using log-log

and log-linear space. Presentation in this manner facilitates both quantitative and qualitative analysis of the particular distribution form best characterizing the data, and also provides a means for the identification of potential sampling artifacts associated with a given dataset (e.g. Scholz et al., 1993; Pickering et al., 1995; Gupta and Scholz, 2000a; Ackermann et al., 2001). Fault populations typically exhibit either power-law or exponential size distributions (e.g. Ackermann et al., 2001). Power-law size distributions are commonly observed in low-strain environments, typical of distributed continental deformation, whereas exponential distributions are typically observed in regions of higher total strain, such as localized rift zones (e.g. Cowie, et al., 1994; Carbotte and Macdonald, 1994; Gupta and Scholz, 2000a; Spyropoulos et al., 2000).

Power-law fault size distributions reflect fractal, or self-similar, fault populations in which the constituent faults exhibit similar characteristics despite differences in the scale of observation. This type of distribution is described by the equation:

$$N(L) = aL^{-C}$$

where N(L) is the total number of faults with length greater than or equal to a specified value, L (e.g. Scholz and Cowie, 1990; Marrett and Allmendinger, 1992; Scholz et al., 1993; Pickering et al., 1995). The constant a, is related to the total number of faults within the dataset. The exponent C represents the slope of the equation that best fits the size distribution. This value provides a means to estimate the relative number of small faults versus large faults (e.g. Scholz and Cowie, 1990; Marrett and Allmendinger, 1992). Larger values of C suggest the data adhere to a relatively narrow size range, and that relatively small faults within a given population play a significant role in total strain accommodation. Conversely, small values of C indicate that most strain is

accommodated on few relatively large faults. The importance of strain accommodation on large versus small faults has implications for estimation of total strain given that the smallest size fraction, which are typically much more numerous, are often left unresolved due to sampling limitations (e.g. Scholz and Cowie, 1990; Marrett and Allmendinger, 1991, 1992; Walsh et al., 1991; Pickering et al., 1995).

Recent studies suggest that fault size-frequency distributions may change with time and/or total strain (e.g. Spyropoulos et al., 1999; Gupta and Scholz, 2000a; Ackermann et al., 2001). Dynamic fault size-frequency distributions reflect changes in patterns of strain distribution that arise as a consequence of spatial limitations imposed on developing fault populations (e.g. Gross et al., 1997; Wojtal, 1994, 1996; Cowie et al., 1995; Ackermann and Schlische, 1997; Ackermann et al., 2001; Clifton et al., 2000; Gupta and Scholz, 2000a). Such limitations are attributed to fault interactions (or correlations), which stem from fault-generated stress perturbations within the faulted medium (e.g. Sornette et al., 1990; Cowie et al., 1994; 1995; Ackermann and Schlische, 1997; Gupta and Scholz, 2000a), or to geometrical limitations associated with the dimensions of the faulted medium (e.g. Ackerman et al., 2001). In nature, the latter relates to compositional or structural heterogeneities, which define the geometric bounds of the mechanical layer. While fault interaction, in terms of imposed crustal stress heterogeneities, is commonly cited as the mechanism that initially gives rise to fractal or self-similar fault growth patterns, and thus power-law size distributions (e.g. Sornette et al., 1990; Cowie et al., 1994, 1995), spatial limitations imposed by the dimensions of the faulted medium are often cited for the subsequent breakdown of such growth patterns (e.g. Wojtal, 1996; Ackermann et al., 2001). The absence of a self-similar growth

pattern, due either to uncorrelated crack formation during the early stages of nucleation (Cowie et al., 1995), or to the suppression of fault interaction during latter growth stages (Ackermann et al., 2001), is reflected by the development of exponential size distributions.

The effects of geometric limitations on fault growth are well illustrated using experimental fault populations. Results from Ackermann et al. (2001), which are based on fault populations developed within experimental clay layers, indicate that the mechanical layer thickness exerts a first order control on observed size-frequency distributions. In their analysis, fault populations initially characterized by power-law distributions subsequently exhibit exponential distributions once the bounds of the mechanical layer become breached. The explanation: faults with vertical dimensions (down-dip) that span the thickness of the mechanical layer experience a breakdown in self-similar growth, whereby growth in the vertical sense is inhibited, while growth along-strike continues relatively unencumbered through tip propagation and/or linkage (Ackermann and Schlische, 1997; Ackermann et al., 2001). Variations in the geometric patterns of fault growth are indicative of fundamental changes in the manner in which faults accommodate strain. Changes in geometric growth patterns are reflected by increased fault aspect ratios (i.e. ratio of along-strike dimension to down-dip dimension; e.g. Nicol et al., 1996), changes in the shape of along-strike displacement profiles (e.g. Dawers et al., 1993), and ultimately, by a change from power-law to exponential fault size-frequency distributions (Ackermann et al., 2001).

Sampling Limitations

Several sampling limitations have implications for fault size analyses. Sampling

limitations often contribute to deviations, or artifacts, within fault datasets that are unrepresentative of the true size-frequency distribution characterizing a given population. The main such limitation stems from the dimension of sampling. Natural fault populations exist in three dimensions, yet the realm of observation is often limited to two dimensions (map-view), or even one dimension (traverse, scan-line or borehole). In this respect, faults that do not extend to the surface or line of observation will not be included in a given dataset (Figure 5-4) (Pickering et al., 1995; Ackermann et al., 2001). Moreover, faults that do not nucleate precisely at the surface of observation will exhibit surface traces that are under-representative of true fault length at depth (Ackermann et al., 2001). A further limitation lies in the resolution of the observation method. The size fraction that exists at or below the resolution limit will inevitably be under-sampled. In this regard, the distribution of the smallest size fraction in a given dataset typically reflects resolution limitations rather than the true distribution form. This effect, referred to as truncation, results in the characteristic flattening of the distribution curve for small objects (Pickering et al., 1995; Ackermann et al., 2001). Similarly, resolution limitations also apply to fault tips. Depending on the fault displacement gradient (related to the distance over which displacement dies out) this may lead to further underestimation of fault length. Lastly, the largest faults of a given population may not be located within a particular sample area, and even if they are, they may extend beyond the defined bounds of the sample area, and can thus only be partially sampled (Figure 5-4). This effect, referred to as censoring, is commonly cited for the characteristic "roll-over" region observed at the large end of size-distribution plots (e.g. Scholz et al., 1993, Burroughs and Tebbens, 2001).
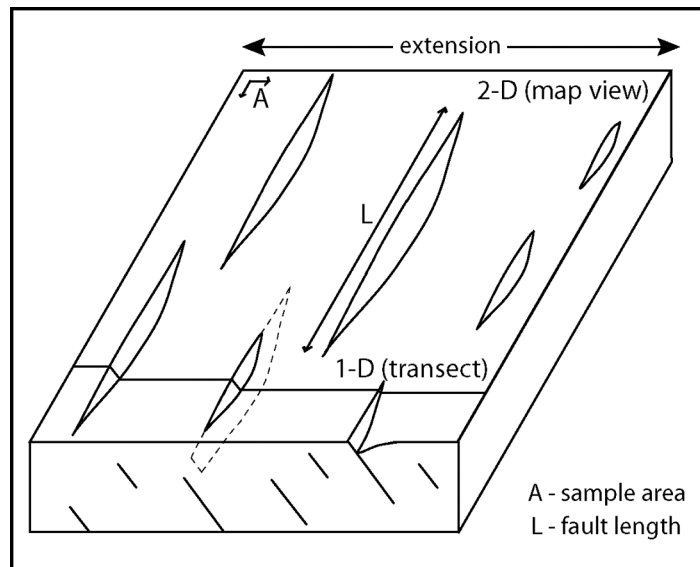
Figure 5-4. Diagram illustrating the limitations inherent in sampling fault populations. In map-view, sampling of faults that extend beyond the defined sample area will result in undersampling of actual fault length (censoring). Faults that do not extend to the surface of observation will result in undersampling of the population as a whole. Faults that do not nucleate at the surface of observation will appear smaller at the surface (dotted line illustatres how a large fault at depth may appear smaller at the surface). Transects, which are typically used to collect fault displacment data, may not sample the area of greatest fault displacement, resulting in underestimation of fault size. Transects will also not sample faults that lie below the surface of observation. For both methods, resolution limitations related to the size of the smallest observable displacement affect both small faults and fault tips (truncation).

Data and Methods

We collected fault length data using a two-dimensional (map-view) sampling method, whereby fault lengths were measured from compilations of mapped surface traces. Fault lengths for the regional northeast-striking normal fault population (Figure 5-1) were obtained from the Fault Activity Map of California by Jennings (1994) at a scale of 1:750,000. Despite the coarse scale, measured fault lengths are in agreement with those published in more focused contributions (e.g. Ross, 1967; Hall, 1971; Lee et al., 2001b; Lee et al., 2005). We interpreted fault lengths based on mapped surface traces, typically fault segments showing Mid to Late Pleistocene activity, with additional consideration given to adjacent footwall (range) morphology. While considerable emphasis is often placed on the most recent episodes of fault activity (i.e. Late Pleistocene fault scarps), incorporation of footwall morphology, in terms of lateral range extent, provides a more accurate assessment of long-term fault development and subsequent whole-fault geometry. We note that the sample area for this population specifically includes all faults so as to limit censoring of fault length.

For further analysis we compiled fault maps for both the Saline Range, located near the northern tip of the SVFZ (Figure 5-1 and 5-2) and northern Owens Valley, located near the northern tip of the OVFZ (Figure 5-1 and 5-3). The fault map for the Saline Range was compiled from Ross (1967), Nelson (1971), and Sternlof (1988), each at a scale of 1:62,500, with additional mapping conducted using one-meter USGS digital orthophoto quadrangles (DOQQ). The fault map for northern Owens Valley was compiled from Bateman (1965), Bryant (1989), and Beanland and Clark (1994), at scales of 1:62,500, 1:48,000, and 1:24,000, respectively. Additionally, in order to better define

fault geometry within Late Pleistocene alluvial deposits here, we conducted both field and aerial-photo mapping using 1:40,000 scale photographs. The finalized fault maps for each location were compiled digitally and checked for consistency with DOQQ base-maps. Fault lengths were then measured using ArcView.

Length data were collected for the Saline Range fault population (Figure 5-2), as well as two distinct fault populations within northern Owens Valley, including a northeast-striking fault set (southern sample area, Figure 5-3) and a north-striking fault set (northern sample area, Figure 5-3). Data from the north-striking population were further differentiated into four sub-populations based on exposure on four distinct Middle to Late Pleistocene age geomorphic surfaces including the VT and the Qt4, Qt3, and Qt2 terrace surfaces (Figure 5-5). For these populations, fault length is defined based on the continuity of surface exposure traces with additional consideration given to fault spacing and, where possible, fault displacement. Upon visual inspection, fault traces with relatively low separation to tip overlap ratios were generally considered to constitute a single fault. Such ratios are indicative of an advanced stage of interaction between faults, and an increased likelihood of linkage (e.g. Gupta Scholz, 2000b).

We note that the Fish Slough fault (FSF) is not included in our analysis (Figure 5-5). The FSF, which exhibits up to ~120 m of cumulative vertical displacement, represents a large array of hard-linked normal fault segments (dePolo, 1998; Ferrill et al., 1999). While the FSF does outcrop within the Bishop Tuff, it is inferred to have developed in response to slip at a much greater depth than the remainder of faults within the VT (Bateman, 1965). Furthermore, the sample area for the VT fault population was specifically limited to the southern half of its total exposure area in order to exclude three
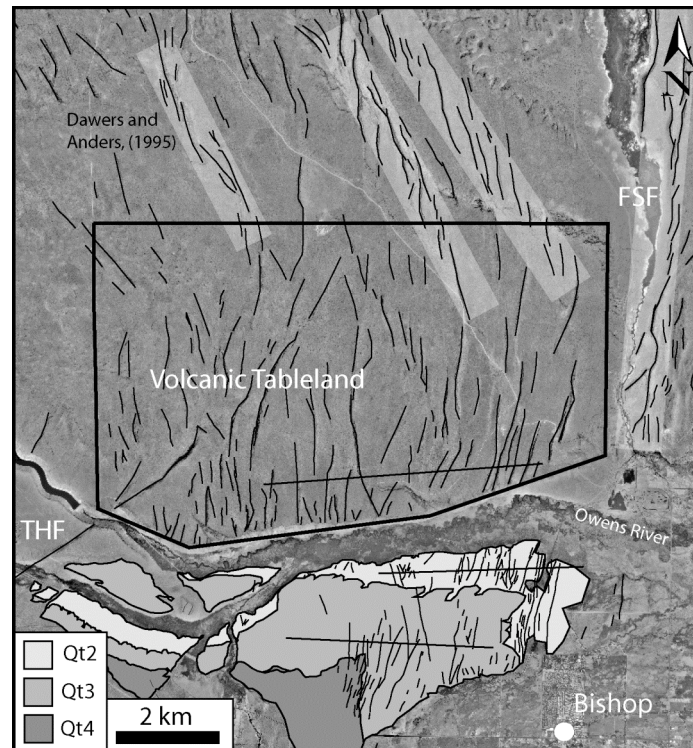
Figure 5-5. North-striking normal fault population developed in northern Owens Valley within the Volcanic Tableland, and three Late Pleistocene terrace units (from youngest to oldest: Qt2, Qt3, and Qt4). Fault data were collected from four sample areas. The sample areas for the terrace surfaces are defined by irregular surface exposure traces inclusive of the largest surface outcrop area. East-west lines denote locations of transects used to measure fault throw (vertical displacement) for use in strain calculation. Light shaded rectangles indicate potential oblique-slip fault arrays, which are excluded from the analysis. Note location of fault studied by Dawers and Anders (1995). FSF – Fish Slough fault; THF – Tungsten Hills fault.

prominent left-stepping en echelon fault arrays (Figure 5-5). Based on their en echelon geometry, and observations of focal mechanisms associated with the nearby 1986 Chalfant Valley earthquake, which exhibit some component of strike-slip (Smith and Priestly, 2000), these faults likely constitute oblique-slip arrays, and are thus representative of a different mode of stain accommodation than that observed for the remainder of the faults on the VT. Moreover, Dawers and Anders (1995) concluded, based on the summation of displacement from discontinuous (i.e. fault) and continuous (i.e. tilting) deformation, that the westernmost of these arrays (indicated in Figure 5-5) exhibits a displacement versus length ratio consistent with that of a single fault, suggesting it is in an advanced stage of linkage, and thus constitutes a single large fault. Despite this observation, however, some ambiguity remains concerning the extent of fault linkage in other areas of the VT (shaded white boxes; Figure 5-5). In this regard it is unclear whether these faults constitute single large faults or multiple medium to small sized faults. Based on this ambiguity, and the potential for oblique slip mechanisms, we exclude these faults from our analysis.

Results

Length data derived from the regional scale (i.e. greater ECSZ) fault population is presented in Figure 5-6A. The dataset is representative of the largest northeast-striking normal faults of the ECSZ, including the TPF, TMF, DSF, EF, DMF, OLF and QVF (Figure 5-1; Appendix G). Note that expansion of the dataset could only be achieved through the addition of faults with lengths less than that of the faults presented here. Each of the faults within the dataset is associated with relatively distinct valley and range morphology at the scale of observation, whereas faulting below the observed size range
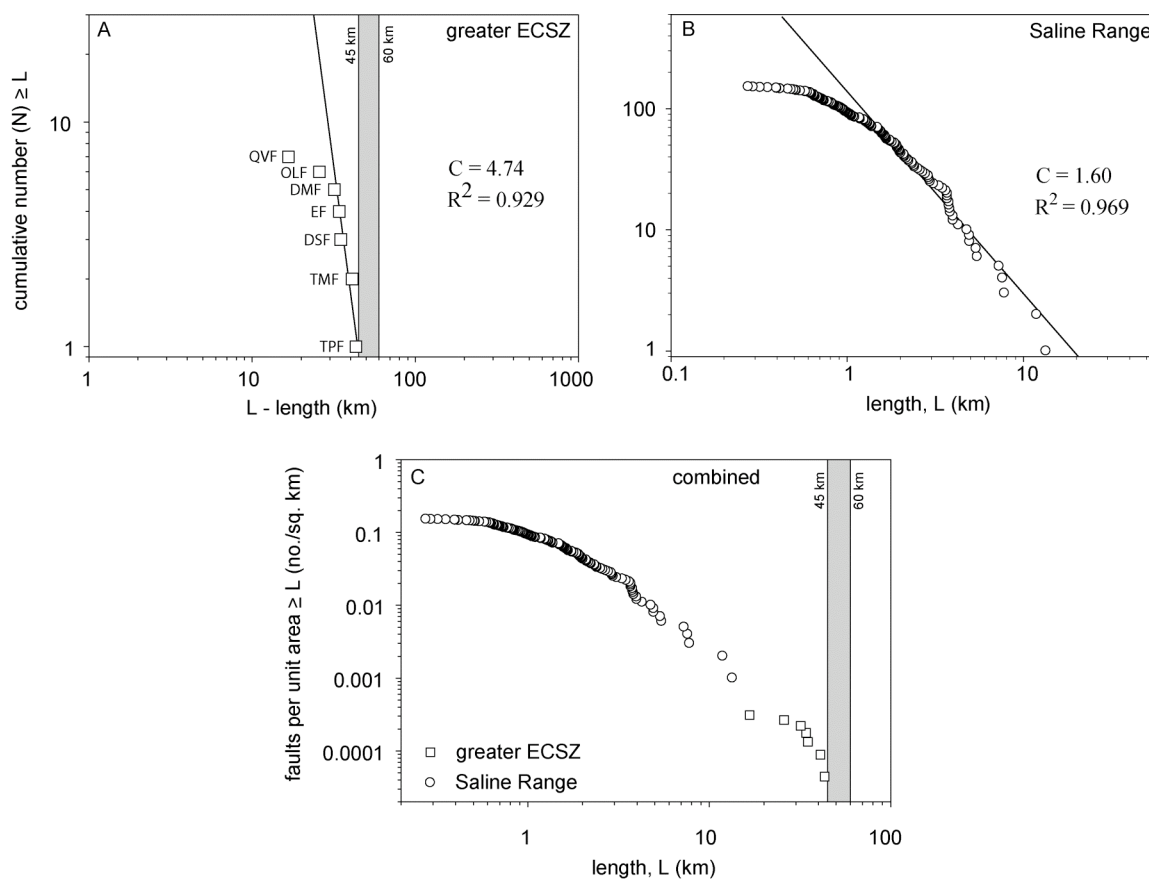
Figure 5-6. **(A)** Fault length data from the greater ECSZ plotted as cumulative number of faults vs. fault length. The cumulative number, N represents the number of faults with lengths greater than or equal to a given value of L. Shaded region illustrates the ~45-60 km range of strike perpendicular spacing between dextral fault zones within the ECSZ. **(B)** Fault length data from the Saline Range represented in the same manner as in Figure 5-6A. These data follow a power-law distribution with a slope of -1.60. **(C)** Combined plot of both datasets with cumulative number normalized by sample area. Normalizing the data by sample area yields an estimate of fault density, represented as the number of faults of a given size per unit area. Note the relatively consistent trend shared by each of the datasets. This suggests fault density is similar over the range of observational scales.

lacks such distinction. Estimated fault lengths range from ~17 to 43 km (Appendix G).
The largest faults in the dataset appear to follow a power-law distribution over less than
one order of magnitude, with an exponent of ~4.7. Dextral fault spacing (i.e. distance
measured perpendicular to strike between adjacent dextral faults) within the ECSZ, which
varies along strike between approximately ~45 km and ~60 km, is illustrated in Figure 5-
6A and 5-6C.

Length data for the Saline Range fault population are presented in Figure 5-6B.
The dataset consists of 152 faults ranging in length from ~0.3 to 13.4 km (Appendix G).
The data exhibit a power-law size distribution above the estimated resolution cutoff of
~1-2 km. The distribution of faults smaller than the resolution cutoff exhibits a slope that
gradually decreases towards zero with decreasing fault size (Figure 5-6B). A plot of
cumulative number of faults normalized by sample area indicates that both the regional
scale and Saline Range populations exhibit comparable relationships between fault length
and fault density (defined as the number of faults of a given size per unit area) despite
differences in the scale of observation (Figure 5-6C).

Length data from the northeast-striking normal fault population in northern
Owens Valley are presented in Figure 5-7. The dataset consists of 18 faults, including
several faults located near the northeastern margin of the Coyote Warp, as well as two
prominent faults located near the northern end of surface rupture associated with the 1872
Owens Valley earthquake, the Klondike Lake (KLF) and Klondike Springs (KSF) faults
(Beanland and Clark, 1994). In addition, the THF, which is located west of the town of
Bishop, California, is included in the dataset. Fault lengths range from ~0.7 to 13.7 km
(Appendix G). Despite the limited size of the dataset, and except for the two largest
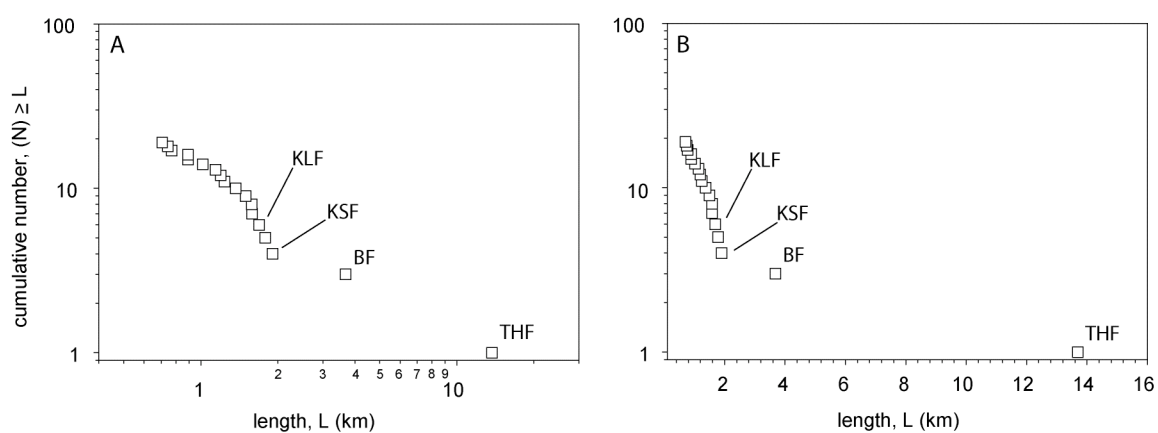
Figure 5-7. Cumulative number of faults vs. length for the NE-striking normal fault population within northern Owens Valley plotted in **(A)** log-log and **(B)** log-linear space. Fault below ~3 km in length approximate an exponential distribution. The out-lying data points (Tungsten Hills fault – THF; Bishop fault – BF) represent faults that are not subject to the same growth limitation as that imposed on the remainder of the population. The Klondike Lake (KLF) and Klondike Springs (KSF) faults mark the northern termination of surface rupture attributed to the 1872 Owens Valley earthquake (Beanland and Clark, 1994).

faults, the distribution of fault lengths appears to broadly conform to an exponential form. The graben width (i.e. spacing between the large range-bounding faults) in the southern portion of northern Owens Valley is ~10 km, while in the vicinity of the VT, the graben width increases nearly threefold to ~30 km (Figure 5-3).

The dataset for the north-striking normal fault population in Owens Valley includes a total of 258 faults (Figure 5-5). Individually, the defined sample areas for the VT, Qt4, Qt3, and Qt2 surfaces include 132, 15, 44, and 67 faults, respectively (Appendix G). Approximately 10 faults sampled on the VT are explicitly truncated by the northern defined boundary of the sample area; however, we note that a significantly higher number may have experienced physical truncation along the southern erosional margin of the VT (Figure 5-5). Furthermore, it is likely that several faults within the terrace units are also subject to similar truncation, as several faults appear to terminate at terrace erosional margins. This is especially true for the Qt4 terrace where more than half the existent faults appear to be censored at the erosional margin.

Fault length-frequency data for each of the north-striking normal fault subpopulations are illustrated in Figure 5-8. Fault lengths from the VT do not follow a power-law distribution in log-log space. The same dataset, however, clearly defines an exponential distribution when observed in the log-linear space. Faults from the Qt2 and Qt3 terrace surfaces follow linear distribution trends in log-log space, indicative of a power-law size distribution for faults greater than ~200 m in length. The values of C derived from the Qt2 and Qt3 datasets are -1.4 and -1.5, respectively. Fault length data from the Qt4 surface are considered overly diluted by sampling bias (i.e. censoring associated with erosional terrace margin) and thus do not lend to valid comparison with
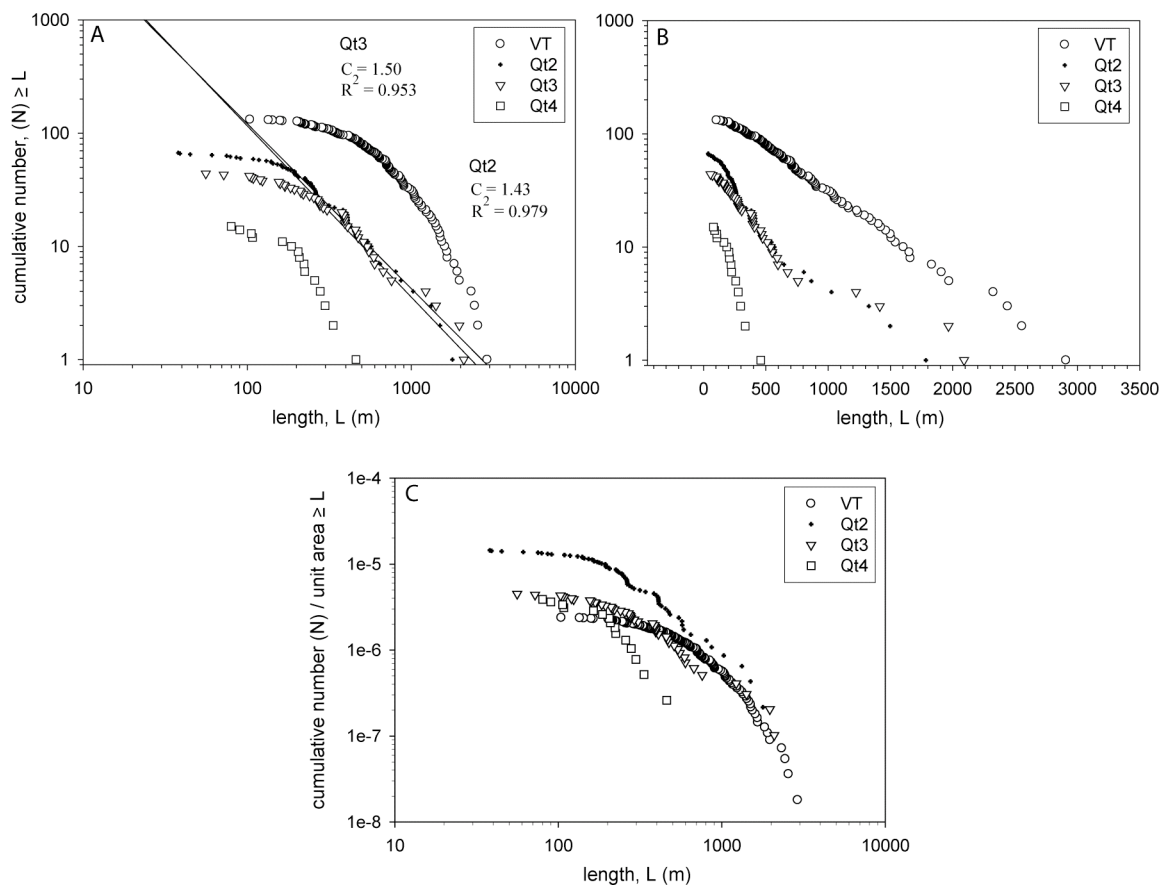
Figure 5-8. Cumulative number of faults vs. length for the north-striking fault population in northern Owens Valley plotted in **(A)** log-log and **(B)** log-linear space. Fault length data from the VT exhibit an exponential distribtion. Data from the Qt2 and Qt3 surfaces are better characterized by power-law distributions with slopes of -1.43 and -1.50, respectively. Data from Qt4 are overly diluted by censoring (much more than half the dataset extends beyond sample area), and are thus unrepesentative of a characteristic size distribution. **(C)** Cumulative number of faults normalized by sample area illustrates fault density.

the other fault subsets, which are much less affected by censoring. A combined plot of the each fault subset normalized by sample area provides a measure of fault density. The VT and Qt3 populations exhibit comparable densities over about an order of magnitude, however, the Qt2 population, departs from this trend with a higher overall density.

Discussion

A striking aspect of our fault size analysis is the correspondence between the range of observed fault lengths and the space allowable for along-strike fault propagation. The data presented here suggest that along-strike geometric limitations stemming from the spacing of sub-perpendicular boundary faults influence the development of the intervening fault networks. The largest northeast-striking normal faults of the ECSZ, and similarly oriented faults within northern Owens Valley, best illustrate this relationship.

Northeast-Striking Faults of the Greater ECSZ

The size distribution of the regional scale normal fault population examined here adheres to a relatively narrow length spectrum, as reflected by the high power-law exponent (C = 4.7). This implies that the largest size fraction of northeast-striking faults within the ECSZ cluster below a maximum value. We suggest the existent dextral fault zones, which are oriented obliquely to, and exhibit higher slip rates than, the northeast-striking normal fault population, represent structural heterogeneities that limit intervening fault growth. The boundary fault spacing, as measured perpendicular to the strike of the dextral fault zones, ranges from ~45 to 60 km from north to south, whereas the maximum observed fault length is ~43 km (Figure 5-6A). The spacing of the boundary fault zones places an upper limit on the maximum along-strike dimension that may be attained by faults developed within the extensional accommodation zones of the ECSZ. We expect

that well-developed structural (and thus kinematic) connections between the observed modes of faulting (dextral and normal) should be reflected by a fault length distribution that extends into, but not beyond the shaded region illustrated in Figure 5-6A.

We note that the data presented in Figure 5-6A are representative of the largest members of the fault population examined here. These data therefore do not suffer from censoring (i.e. fault size exceeds the dimensions of the sample area) as described by Pickering et al. (1995) and Ackermann et al. (2001). However, given the coarse scale of observation, and the potential of fault surface expression lagging fault development at depth, the data are likely subject to a sampling bias related to the under-measurement of fault length in the tip regions. Nonetheless, each fault sampled is equally subject to these effects; therefore the dataset as whole reflects internal consistency with respect to relative fault length. Thus, we suggest that the distribution exponent is unaffected by sampling bias.

The distribution of fault lengths from the regional scale population closely resembles, in a qualitative sense, the characteristic "roll-over" region observed in numerous fault-length distribution datasets. This region is representative of the largest members of a population, and is often characterized by a relatively steep slope in log-log space. While "roll-over" is commonly attributed to incomplete sampling of the largest faults within a population (e.g. Marrett and Allmendinger, 1992; Scholz, et al., 1993; Pickering, 1995; Ackermann et al., 2001), we attribute its occurrence here to the limitation imposed by the bounding fault system, where fault propagation is expected to terminate at the crosscutting dextral faults. Recall that, for this population, we defined a sample area that specifically includes the entire range of observable fault lengths. Also,

recall that resolution limitations at the fault tips are expected to affect each member equally, thus we may expect a shift in the dataset as a whole, rather than a change in the relative distribution. This overall conclusion is similar to that discussed by Cladouhos and Marrett (1996), who attributed "roll-over" to geometrical limitations imposed on the growth of the largest faults rather than sampling bias.

Northeast-Striking Faults in Owens Valley

Fault length data from the northeast-striking normal fault population within northern Owens Valley illustrate how boundary fault spacing, here in terms of graben width, influences fault growth (Figure 5-7). This population appears to broadly conform to an exponential distribution. Each of the faults is located exclusively within a relatively narrow portion of northern Owens Valley (southern sample area; Figure 5-3). This portion of the valley, located south of the town of Bishop, measures ~10 km between the Sierra Nevada and White Mountain range-fronts. This distance corresponds similarly to the tip-separation between the OVFZ and WMFZ, which have formed in close association with the structure of the range-front faults in this area. Given these well-established fault systems, we suggest that the graben width imposes a boundary condition limiting the maximum along-strike development of the intervening normal faults. In this regard the basin width here is analogous to the previously discussed dextral fault spacing observed for the greater ECSZ.

The two outlying data-points indicated in Figure 5-7 represent distinct departures from the overall exponential distribution. The most prominent outlier is the THF, which measures ~13.7 km along strike. The relatively large size of the THF with respect to the remainder of the fault population corresponds to a dramatic increase in the width of

northern Owens Valley. The increase in basin width is attributed to a large left step in the Sierran range-front locally known as the Coyote Warp (CW; Figure 5-3), whereby the bounding fault spacing consequently increases from ~10 km in the southern portion of the valley, to ~30 km in the vicinity of the VT. Because of the three-fold increase in basin width, the THF is not subject to the same geometric limitations, and therefore does not conform to the same distribution trend as that characterizing the remainder of the population. The second outlying fault in Figure 5-7 is the Bishop fault (BF). The BF is indeed located within the narrow portion of the valley (Figure 5-3), and is be expected to fall under the same limitations as its neighboring faults; however, we attribute its observed length to a change in strike such that it gradually merges with a north-striking normal fault segment located along the eastern margin of the Coyote Warp. In this regard, the BF does not strictly adhere to the limitations imposed on northeasterly trending fault propagation.

Despite these observations, it is important to note that evidence for northeast-striking normal faults on the eastern side of northern Owens Valley is conspicuously absent. The modern floodplain of the Owens River constitutes much of this area suggesting the consistent lack of observed faulting here may ultimately reflect Holocene migration of the Owens River and subsequent resurfacing of the Late Pleistocene deposits in which faulting is preserved. Thus, in the context of river migration, the dataset presented here, rather than indicative of a structural control on fault length, may simply reflect circumstantial truncation completely unrelated to any mechanisms of fault growth. The degree to which the data may be affected by such fluvial migration remains unclear. Nonetheless, we suggest the geometry of faulting within this portion of northern Owens

Valley cannot exceed the graben width of ~10 km.

Implications for Developing Fault Populations

Geometric limitations imposed on the along-strike propagation of faults have implications for patterns of strain distribution within actively deforming regions. Given a uniform regional strain rate, typical of plate boundary regions, patterns of strain distribution must change in response to growth restrictions preferentially imposed on the largest faults within a population. The cessation or inhibition of along-strike fault propagation leads to the accumulation of anomalous displacement with respect to length (e.g. Burgmann et al., 1994; Poulimenos, 2000; Gupta and Scholz, 2000a), and may further result in increased activity on smaller faults and/or the nucleation of new faults.

Results from an experimental (clay) oblique rift fault population discussed in Clifton and Schlische (2001) indicate that along-strike limitations in fault growth can indeed result in the nucleation of new faults. In their model, a characteristic length scale, which is dependent on the degree of rift obliquity, is imposed on a developing fault population by the bounds of the experimental rift zone. The nucleation of new faults due to spatial constraints on fault growth is best illustrated in a moderately oblique rift model. In this model, the rate of fault nucleation, though initially rapid, exhibits a marked decrease as the total number of faults through time reaches a plateau at a critical value of total strain. The decrease in nucleation rate reflects localization of strain onto the larger structures within the population (Clifton and Schlische, 2001). However, once these structures reach a maximum size, and can no longer continue to grow in length, (nor displacement) strain becomes de-localized resulting in a increase in the rate of nucleation of new faults and a subsequent change in the overall kinematic framework.

We suggest this mechanism may account for the development of the distributed normal fault population within the Saline Range (Figure 5-2). The size distribution exhibited by this population closely approximates a power-law distribution over about 1 order of magnitude (Figure 5-6B). Recall that power-law distributions typically characterize unconstrained fault populations. Because faults within the Saline Range do not exceed ~15 km in length, we suspect they are not yet constrained along-strike by the either the SVFZ or the Last Chance range-front fault along the eastern margin of Eureka Valley, which are separated by a distance of ~40 km. Furthermore, recent seismicity, as evidenced by the 1993, Eureka Valley earthquake, combined with the relatively subdued surficial expression of the EVF with respect to the substantially larger, yet genetically related DMF, TMF, and DSF, together suggest that faulting within the Saline Range may be a relatively recent occurrence. However, due the paucity of available slip rate data along the nearby DMF and TMF it is unclear whether significant temporal changes in slip have occurred along either of these faults. The DMF has an inferred Late Pleistocene slip rate of ~0.01 mm/yr (dePolo, 1998), suggesting it may be in a period of relative quiescence, or possible inactivity. Moreover, firm evidence for Late Pleistocene activity along the TMF is lacking. Given these relations, it is plausible that the initiation of faulting within the Saline Range is related the cessation of activity on one or more of the larger northeast-striking faults, which would be expected to result in a subsequent reorganization of slip loci.

In general, changes in patterns of strain distribution are expected to occur on timescales that are approximately equal to the lifespan of the largest constrained faults within a population. An important implication of this is that the timescales over which

fault networks experience major changes may be dependent upon the geometry of, and the strain rate imposed upon, faults that are subject to inherent limitations in growth. In this regard, we suggest that the northeast-striking normal faults examined here play a significant, yet relatively under-recognized, role in the reorganization of slip loci within the ECSZ. We suggest that once faults of this nature grow to a length that is equal to the boundary fault spacing they become inactive. This results in the redistribution of slip onto newer or smaller faults of similar orientation, which eventually repeat the cycle as they outgrow their associated boundary fault spacing. A cycle of normal fault development and subsequent death stemming from geometric constraints imposed by the larger more active dextral faults, is a possible mechanism for the observation that the regional scale northeast-striking faults young to the northwest, as proposed by Dixon et al. (1995) and discussed by Lee et al. (2001b).

Of broader implication, our results follow those of Ackermann et al. (2001) in suggesting that the innate heterogeneity of the Earth's crust imposes a measurable effect on developing fault populations, such that few, if any, natural populations will strictly adhere to a single scaling law through the entirety of their temporal evolution. Thus, it follows that the degree to which a fault population does adhere to predicted growth or scaling relationships depends on when (in geological time) the population is sampled. Cowie et al. (1995) suggested that this may explain the views of Scholz and Cowie (1990) and Marrett and Allmendinger (1992) and others, who used empirically derived scaling relations to reach conflicting conclusions concerning the importance of small faulting to overall strain accommodation. The work of Spyropoulos et al. (1999, 2002) and Gupta and Scholz (2000a) further supports the view that scaling relationships (e.g.

self-similar as reflected by power-law size distributions) are indeed scale limited.

North-Striking Faults in Owens Valley

Fault length data derived from the north-striking faults within northern Owens Valley reveal a dichotomy in fault size-frequency distributions exhibited within a single population. Faulting on the VT follows an exponential size distribution, whereas faulting within both the Qt2 and Qt3 surfaces appears best characterized by power-law distributions. We suggest two potential explanations for this observation: 1) the data reflect true variation in the fault size distribution through time, indicative of a fundamental change in the mode of strain accommodation, or 2) sampling biases overly dilute the data such that the true fault size distributions are masked through incomplete sampling of faults.

In a preliminary investigation, Scholz et al. (1993) present similar fault size-frequency data from the VT, and concluded that the population adheres to a general power-law distribution. Their conclusion is based on a comparison of fault subsets characterized at three successively smaller scales of observation (1:62,000, 1:24,000; and direct field observation). They suggest that the median sized fault length data from each subset is least affected by sampling bias, and thus together approximate a power-law distribution. They attribute observed deviations from the idealized power-law distribution, as exhibited by the largest and smallest size fractions in each of the data subsets, to sampling biases, and thus exclude these data from their interpretation. While their interpretation is useful for theoretical considerations of first-order scale invariance with regard to fault growth, they neglect the real physical limitations imposed on fault growth.

Each of the north-striking normal fault subpopulations analyzed here are constituents of a single larger fault population that has developed within a single tectonic, and arguably, lithologic environment. The lithologic contrast between the VT and the terrace units may contribute to the observed size distributions since the higher yield strength of the Bishop Tuff is expected to limit lateral fault growth more readily than that of relatively unconsolidated sediment (e.g. Cowie and Scholz, 1992). However, because the terrace units locally mantle the Bishop Tuff to depths as little as ~5 m, scarps located in this area likely reflect faulting within the underlying tuff. Furthermore, it is unlikely the thin sediment veneer has much effect on the transmission of deformation to the surface. On this basis, we suggest that lithologic contrasts between the faulted units may be ruled out as a possible explanation for the observed distributions.

Our preferred interpretation is based on differences in the estimated total strain accommodated by faulting within each of the surfaces. Extension estimates derived from east-west transect lines (Figure 5-5) indicate the VT has undergone ~1.6% strain over the length of the transect, whereas the Qt2 and Qt3 transects yield strains of ~0.1% and ~0.4%, respectively (Chapter 4). These results, in the context of the observed fault size distributions, suggest there may be a distribution transition related to a critical strain threshold. This interpretation is bolstered by several previous investigations that link an increase in total strain to observed transitions in fault size-frequency distributions from power-law to exponential (e.g. Gupta and Scholz, 2000a; Ackermann et al., 2001; Spyropoulos et al., 1999, 2002).

Ackermann et al. (2001) observed that adjustments in the thickness of an experimental mechanical layer (clay) moderate the value of total strain at which a size-

distribution transition is expected to occur. Recall that when faults reach the bounds of the mechanical layer they experience a breakdown in self-similar scaling resulting in a change in the size distribution from power-law to exponential. By reducing the mechanical layer thickness, developing faults reach the geometrical bounds of the faulted medium sooner in time or strain. Of particular interest, the results of Ackermann et al. (2001) show that a decrease in the thickness of the mechanical layer reduces the value of total strain at which the distribution transition occurs. The implication of this result is that transitions in fault size-distributions may occur in relatively low strain environments given a thin enough mechanical layer. The Bishop Tuff, with an estimated average thickness of ~150 m, approximates a relatively thin mechanical layer, however it remains unclear to what extent this thickness could reduce the strain threshold required for a transition in the fault size distribution. Nonetheless, given the correlation between relatively low strains (~0.1% and ~0.4%) across the Qt2 and Qt3 with the power-law length distributions, and the comparatively high strain (~1.6%) across the VT with the exponential distribution, we suggest that the observed fault patterns may reflect temporal variations in the strain accommodation related to the thickness of the Bishop Tuff.

Fault size distribution transitions can be explained in terms of fault density, which is related to both strain and mechanical layer thickness (e.g. Spyropoulos et al., 1999). Fault density within a population is expected to increase with increasing strain through the nucleation of new faults, as well as through the propagation of existing faults; both of which lead to an increase in fault length per unit area. Results from experimental (Spyropoulos et al., 1999) and natural (Gupta and Scholz, 2000a) fault populations, however, show that the rate at which fault density increases levels off such that it attains

a steady, or possibly a reduced value, once a critical value of strain in reached. This is expected to occur once faults within a population grow to a point where they begin to interact over a broad area through stress shadowing. Note that fault development, whether through the nucleation new faults or the propagation of existing faults, is retarded in areas of stress shadowing (e.g. Ackermann and Schlische, 1997). Stress shadowing, which scales with fault size, increases in areal extent with increasing strain, and thus continually reduces the space available for fault nucleation and tip propagation (Spyropoulos et al., 1999). With increasing strain, fault growth occurs increasingly through the coalescence of existing segments, rather than through nucleation or tip propagation. Thus, for fault populations where stress shadowing becomes dominant, the rate of increasing fault density is expected to decrease (e.g. Spyropoulos et al., 1999; Gupta and Scholz, 2000a). Conversely, fault populations that have yet to reach a point where fault interaction is dominant (i.e. before a critical strain threshold is reached) should exhibit lower fault densities, which will increase with increasing strain.

As strain approaches a critical threshold where fault density attains a maximum value, the rate of fault nucleation decreases (due to the increased area of stress shadow from an increase in the number and size of faults). Similarly, as fault sizes increase, so too does coalescence of existing fault segments, resulting in more intermediate to large sized faults within the population relative to small sized faults. Thus, at lower strains, a fault size distribution responds primarily to the addition of small faults through nucleation, while at higher strains a fault size distribution responds to a reduction in the relative number of small faults (inhibited nucleation due to stress shadowing), and an increase in the number of intermediate sized faults due to coalescence (Spyropoulos et

al., 1999). The result is a gradual change in the size distribution from power-law to exponential with increasing strain.

Given the observation of larger faults on the VT, it is assumed the fault population there is in a much later stage of development than those on the Qt3 and Qt2 surfaces. While it can be argued that censoring at the erosional margins of the Qt3 and Qt2 terraces may artificially limit the size of the largest observable faults on these surfaces terraces, and thus make any general comparison of maximum fault length invalid for inferring a relative stage of development, the ranges of vertical displacement from each surface (VT: 2.4-37.4 m; Qt3: 2.8-6.2 m; Qt2: 0.8-2.6 m; Appendix E), which were sampled in transect, further validate our assumptions for the relative development stages of the observed population. The correspondence between the age of the VT (~760 ka; Sarna-Wojcicki) and the Qt2 terrace (21 ± 3.3 ka; Chapter 4) with observed displacements there (i.e. older surface, greater displacement), and thus estimated strain, are indicative of contrasting time periods of fault growth, and thus fault development.

Because faulting on the VT is in a latter stage of development, faults there are much more likely to be subject to interaction through stress shadowing, and possible bounding by the mechanical layer (recall the VT has an estimated thickness of ~150 m). If this is indeed the case, we expect fault density on the VT to exceed that of the Qt3 and Qt2 surfaces. However, from Figure 5-8C is becomes clear that no firm relationship between fault density and strain can be ascertained. Fault density on the VT is less than that of the Qt2 surface, whereas it is very similar to that of the Qt3 surface over approximately an order on magnitude. If the VT has reached a critical strain threshold such that fault density has stabilized, and since the strain associated with Qt2 is likely

well below this threshold, as evidence by its much lower strain accommodation (~0.1%

for the Qt2 vs. ~1.6% for the VT), we would expect the VT to have a higher fault density

than both the Qt3 and Qt2 surfaces. We note it is conceivable that the VT has reached a

critical strain threshold, such that its fault density has actually decreased below that of the

developing terrace populations. Nonetheless, we would expect the Qt3 and Qt2 surfaces

to exhibit similar fault densities, given their comparable strain values. From Figure 5-8C,

it is clear they do not. We conclude, given the irregularity of the defined sample areas,

and the uneven spatial distribution of faulting (specifically along the western portion of

the Qt3 terrace sample area; Figure 5-5), that the anomalous fault densities exhibited by

the VT and terrace populations are biased, and do not reflect true density.

The second possible explanation for the observed fault size distributions is related

to sampling bias, which may distort the true nature of the data. From Figure 5-5 it is

clear that, in many instances, faulting within each of the terrace surfaces extends to the

erosional margins of those surfaces. In this regard, it may be argued that censoring of

fault lengths impact the particular size distribution. However, because censoring at the

margins of a sample area reduces the number of large faults, and presumably relegates

them to the small or medium size range, we would expect a fault population censored at

the large size fraction to exhibit a more pronounced exponential distribution. By

removing the largest faults (which are more likely to experience physical truncation at the

erosional margins than small faults) from a size distribution, and placing their reduced

remnants back into the distribution, the total number of fault remains the same, yet the

size-range of the data is reduced. Removal of the largest faults causes the size

distribution to shorten along the x-axis (i.e. reduced size range) resulting in a steepening

of the slope characterizing the overall distribution, less the lowest size fraction, which is biased by resolution limitations. By adding medium to small sized faults (i.e. the remnants of the large censored faults) to a size distribution, the number of faults within these size classes increases, causing those portions of the distribution to move upward, or "bulge" along the y-axis. This effect is similar to that described by Spyropoulos et al. (1999) where the coalescence of small faults and the subsequent formation of intermediate sized faults results in an upward expansion of that size class. Here the resulting distribution, after simultaneous shortening along the x-axis and upward "bulging" of the middle-small size range results in a more pronounced exponential size distribution. Because the Qt3 and Qt2 maintain a power-law distribution, despite the tendency of censoring to promote an exponential distribution, we suggest these two populations are indeed power-law. We base this assertion on the idea that, given an initially exponential distribution of faults subject to an "exponential-distribution inducing" process, the distribution should remain exponential.

Conclusion

Shear in continental settings may give rise to complex fault networks with variable orientation and sense of slip. In such settings, secondary faulting (normal) developed in response to dextral slip transfer is subject to limitations in along-strike growth that are imposed by the spacing of the primary bounding faults (dextral). Secondary faulting within the ECSZ is manifest at both local and regional scales as northeast-striking normal faults, and can be characterized by a single distribution despite differences in scale. At the regional scale, the largest size-fraction of faults, in terms of length, clusters below an upper size limit, which is imposed by the primary bounding

dextral fault zones. We suggest this is indicative of a characteristic length scale. At the local scale, there is a correlation between secondary (normal) fault length and boundary fault spacing, such that a larger graben width, in turn, accommodates the development of larger faults.

Geometric limitations imposed on the growth of developing faults plays a significant role in patterns of strain distribution. Such limitations may result in marked deviations from idealized models of faults growth such that observed scaling relations do not hold at all scales. The correlation between observed fault size and along-strike growth potential (i.e. space allowable for along-strike growth) suggests that conceptual models of fault growth, which provide the fundamental basis for interpreting brittle deformation, will benefit from the incorporation of site-specific details of crustal structure. Furthermore, our data suggest that, given the inherent heterogeneity of the Earth's crust, particularly in terms of lateral variations, scaling relations observed for natural populations are expected to have upper bounds.

Geometric limitations drive evolution within fault networks through the redistribution of slip onto newer, smaller, or more favorably oriented faults. Slip redistribution (i.e. kinematic evolution) is expected to occur over a timescale that is equal to the lifespan of a given constrained fault. This timescale is a function of the physical space allotted for fault growth and the strain rate imposed on that fault. Within the ECSZ, this observation may account for the relatively rapid reorganization of slip loci as observed in geologic slip rate (e.g. Reheis and Sawyer, 1996; Kirby et al., 2006) and paleoseismic data (e.g. Rockwell et al., 2000). We suggest that characterization of constrained faults will benefit past reconstructions, as well as future predictions of

development for evolving fault networks.

Size-frequency distributions observed for faults that offset several distinct geomorphic surfaces highlight potential temporal variations in patterns of natural strain accommodation. Faulting within younger surfaces (Qt2 and Qt3), which accommodate relatively low total strain (< 0.5%), are characterized by power-law size-frequency distributions, whereas faulting within the oldest surface (VT), which accommodates a higher strain (~1.6%), exhibits an exponential distribution. This observation may indicate that distribution transitions from power-law to exponential may occur at a much lower strain than previously observed for a natural fault population (e.g. ~8%, Gupta and Scholz, 2000a).

Chapter 6

Conclusions

Summary

This study provides new insights into the structural and kinematic evolution of northern Owens Valley, California, and its role within the greater Eastern California Shear Zone (ECSZ). Each of the three research contributions contained within this work (Chapters Three, Four, and Five) examines a particular aspect of tectonism where previous work is either incomplete or altogether absent. Discussed below are brief summaries of these chapters, the broader implications of their findings, and the state of current problems that remain unaddressed and require future attention.

Chapter Three presents a new model for the structural evolution of northern Owens Valley, focusing specifically on the Coyote Warp, and the relationship between the Birch Mountain fault (BMF) and the Owens Valley fault zone (OVFZ). In this model, fault dip and the spacing between the conjugate normal faults defining the range-fronts along northern Owens Valley indicate that conjugate fault failure and eventual asymmetry, through fault intersection within the brittle upper crust, is a viable explanation for the development of the unique structure of the Sierran range-front associated with this area.

Chapter Four presents evidence of a previously unrecognized, yet significant change in the extensional strain rate within northern Owens Valley since Mid-Pleistocene

time. This change compares well with other observed slip rate changes within the area over a similar time period, suggesting that regional tectonic forcing may be key to explaining these observations. Furthermore, results from this study contribute to a broad based extensional geologic slip budget that compares well with estimates of geodetically-determined rates of present-day strain accumulation.

Chapter Five presents an analysis of length-frequency distributions from several distinct fault populations, which suggests that boundary or master fault spacing within the ECSZ may play a significant role in the evolution of the existing fault network by limiting the space available for along-strike growth of secondary normal faults. This observation implies that slip redistribution within the ECSZ occurs over timescales similar to those over which individual secondary faults remain active. Furthermore, a transition in the length-frequency distribution observed among fault subsets from a single large fault population indicates that a critical strain threshold, which may be related to mechanical layer thickness, significantly influences the distribution of crustal strain within northern Owens Valley. While previous analyses have come to a similar conclusion, there are very few studies where such observations among natural fault populations are documented.

Implications

The interpretations and conclusions drawn from Chapters Three and Five contribute to a broader understanding of the mechanisms that influence the distribution of crustal strain within tectonically active regions. Chapter Three utilizes a novel approach for interpreting the evolution of crustal-scale normal fault systems, especially those associated with well-developed range and basin morphology. The application of this

model extends beyond the scope of this particular study, in that it may be utilized in any extensional setting in order to make predictions of fault relationships at depth.

Chapter Five outlines the application of fault size-frequency analyses in an examination of neotectonic framework, with particular focus on how bimodal (in terms of strike) fault networks are expected to develop. While this application is here limited to the ECSZ, this type of analysis can be extended to a variety of setting where along-strike fault development may be inhibited. This type of analysis may also yield insights into seismic risk assessment by providing a means to predict limitations in along-strike fault growth. If it can be assumed that seismic rupture along a given fault will stay confined to that fault, them limitations imposed on fault development have consequences for the maximum sized earthquake expected to occur on that fault.

Results from Chapter Five suggest that the origin of the distributed northeast-striking fault population within the Saline Range may be attributed to slip redistribution from nearby structures that have reached their boundary fault spacing and have thus become inactive. While it remains unclear whether the slip histories associated with these larger structures supports this assertion, this idea may be relevant to the debate over the geodetic and geologic dextral slip discrepancy within the ECSZ. If indeed large numbers of small northeast striking normal faults have nucleated within the ECSZ in order to accommodate dextral slip transfer, they may account for a portion of the "missing" geologic slip associated with this discrepancy. It would thus be prudent to further explore these distributed populations in an effort derive a slip budget for inclusion with existent geologic rates.

Results from Chapter Four contribute to the growing body of geologic and

geodetic evidence suggesting that fault slip rates with the ECSZ vary over relatively short temporal and spatial scales. A significant implication of these observations is that the overall fault network within the ECSZ is in a relatively early stage of development, where fault-defined crustal blocks essentially jostle for positioning as strain attempts to localize on a single through-going structure. Such a structure would be analogous to the San Andreas fault system on which essentially all of the relative plate motion associated with the Pacific-North American plate boundary that lies west of the Sierra Nevada Mountains is accommodated.

This interpretation of the ECSZ is rooted in a concept inherent in the development of all fault populations: strain localization. Developing fault populations universally exhibit an initial growth stage that is largely characterized by along-strike growth of relatively numerous, discrete, non-interacting faults. This early developmental stage is phased out as faults begin to interact and link. Faults within a population where interaction and eventual linkage becomes dominant are expected to exhibit variable growth patterns depending on where or when fault slip rates are sampled. In an idealized setting, fault linkage combined with the inhibited development of newer or smaller faults by the stress shadows cast by larger faults, essentially drives localization of strain onto relatively few structures within a population. If indeed the present tectonic framework of the ECSZ is representative of a transitional stage tending towards strain localization, it is expected that a through-going dextral shear structure similar to the San Andreas Fault system will eventually develop within the region.

Future Work

Continued research focused on a broad range of geological problems, as well as

more in-depth geologic and geodetic based characterization of deformation rates within this region are key to further advancing and refining our understanding of the ECSZ. These problems will require a broad range of geological expertise and an extended effort.

One problem in particular lies in the chronology of geomorphic features. Such features provide key insight into the rates of deformation within tectonically active regions, however, there is an overall lack of an established and reliable chronology for pertinent features within the region. While recent advances in analytical dating methods have alleviated this problem in some areas, there remains extensive work in cataloguing important features within northern Owens Valley and the greater ECSZ. The continued application of cosmogenic radionuclide and optically stimulated luminescence age dating techniques to relevant geomorphic surfaces will prove beneficial to this end.

In terms of characterizing deformation, several faults within the ECSZ, specifically some of the largest northeast-striking normal faults require more in depth study, including the Dry Mountain and Tin Mountain faults. Knowledge of the slip histories associated with these faults is crucial both to understanding their role in the large-scale developing fault network, and to testing current models of kinematic evolution with the ECSZ. In general, a more complete model for kinematic evolution requires knowledge of multiple slip rates spanning several timescales for each of the significant faults. Moreover, such slip histories are required at various locations for individual faults, particularly for large faults where large variations in slip are expected to occur throughout the length of the fault depending on where a rate is sampled.

Another problem that needs to be further addressed within Owens Valley, as well as in other portions of the ECSZ, is a more in-depth review of the relationship between

range-front normal faulting and dextral shear. It is generally accepted that the large normal faults in these areas predate the onset of dextral shear, however, there is relatively little published study that compares and contrasts fault geometry or slip rates. In particular it is unclear whether these systems have undergone coordinated variations in slip through time. In this regard, a focused effort to further catalogue fault slip rates in these areas is critical. In general, it appears that the early extension provided a structural template for the distribution of present-day shear, with the large dextral faults utilizing weakened crustal pathways established by early extension. In the case of the OVFZ, where deformation at the surface appears to be apportioned between pure normal and dextral fault planes it is unclear whether the dextral shear has reactivated normal fault planes at depth, or has developed its own through-going structure. A more complete sampling of fault slip rates within this area coupled with a predictive rheologic model of the crust may help resolve this issue.

In terms of the BMF and the OVFZ, it would be useful to coordinate a more in-depth structural and geochronometric study in order to provide a chronology for the extensive basaltic cones and flows associated with the Big Pine Volcanic field, and to examine the relationship of these features with nearby faults. Recall that this area corresponds to the relatively narrow spacing between the BMF and the OVFZ, as well as to the southern limit of distributed west-dipping normal faults. In several cases vents from the basaltic cones, including Crater Mountain, Red Mountain and the Fish Springs cone, correspond to visible fault traces, strongly suggesting that these features are related. If the extensive west-dipping faults do provide the primary conduits for the emplacement of the volcanic features within the Big Pine Volcanic field, and if these features cluster in

age, then a significant structural event might be inferred, possibly related to the interpretations expressed in Chapter Three of this work.

In general, while a great deal can be learned from field-based studies with the ECSZ, it is nearly impossible to test conceptual models of past evolution, or predictions of kinematic development. In this regard it may be useful to implement experimental analogue models tailored specific to the ECSZ in order reconstruct some of the pertinent geologic or geodetic based observations made there. In particular, it would be useful to construct an experimental model designed specifically to simulate the kinematic evolution of the ECSZ. Such a model would require, at the most basic level, recreating the stress field history of this region, specifically extension followed by dextral shear. This could provide potential insights into how the extensional template influenced overprinted dextral shear within the ECSZ. Does shear becomes distributed amongst the existing normal fault networks? Is dextral slip homogeneous throughout? Does slip transfer occur? If so, does shear eventually tend towards localization on a single through-going structure? Answers to these questions and many more would be beneficial to our understanding of the ECSZ.

Appendix A

Scarp Displacement Versus Length Profiles and Cross-Strike Displacement Profiles from Selected West-Dipping Faults and Terraces within Northern Owens Valley
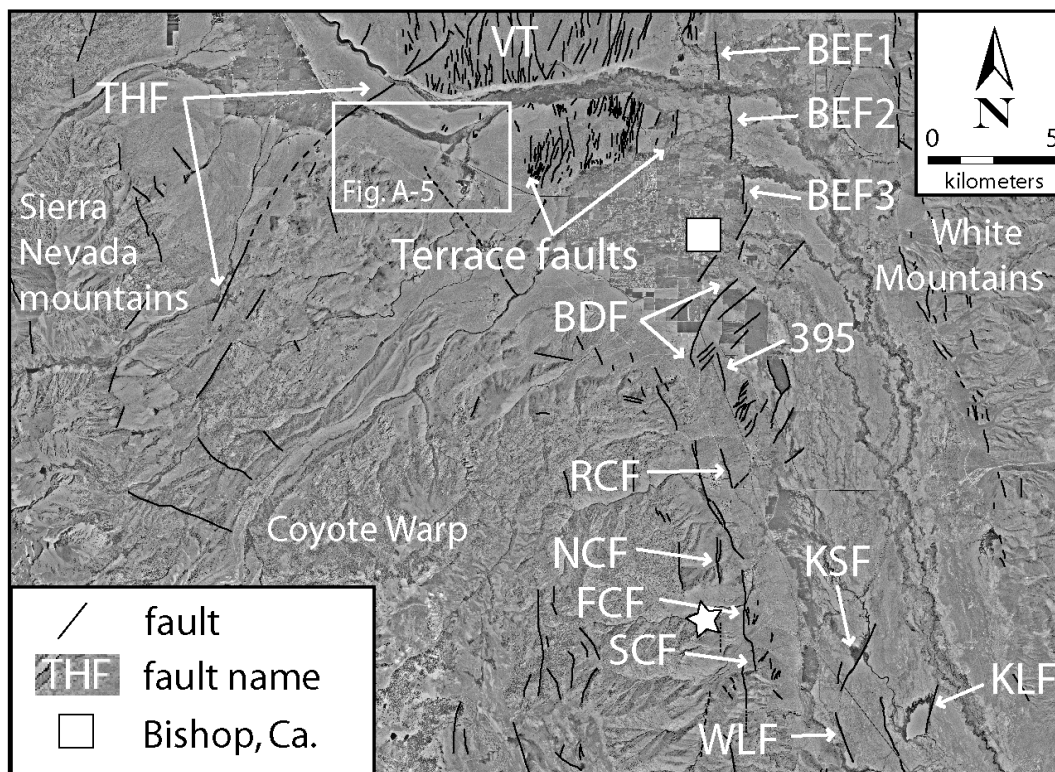
Figure A-1. Location map for surveyed faults and terrace surfaces. Location of Figure A-5 is indicated by white box. Star denotes location of the Freeman Canyon terrace profile (see Figure A-6). Terrace fault profiles are presented in Figure 4-2. 395 – 395 fault; BEF1-3 – Bishop East faults 1 though 3; BF – Bishop fault; FCF – Freeman Canyon fault; FSF – Fish Springs fault; KLF – Klondike Lake fault; KSP – Klondike Spring fault; OVFZ – Owens Valley fault zone; RCF – Rawson Canyon fault; RVF – Round Valley fault; THF – Tungsten Hills fault; SCF – Shannon Canyon fault; WLF – Warren Lake fault; White Mountains fault zone.
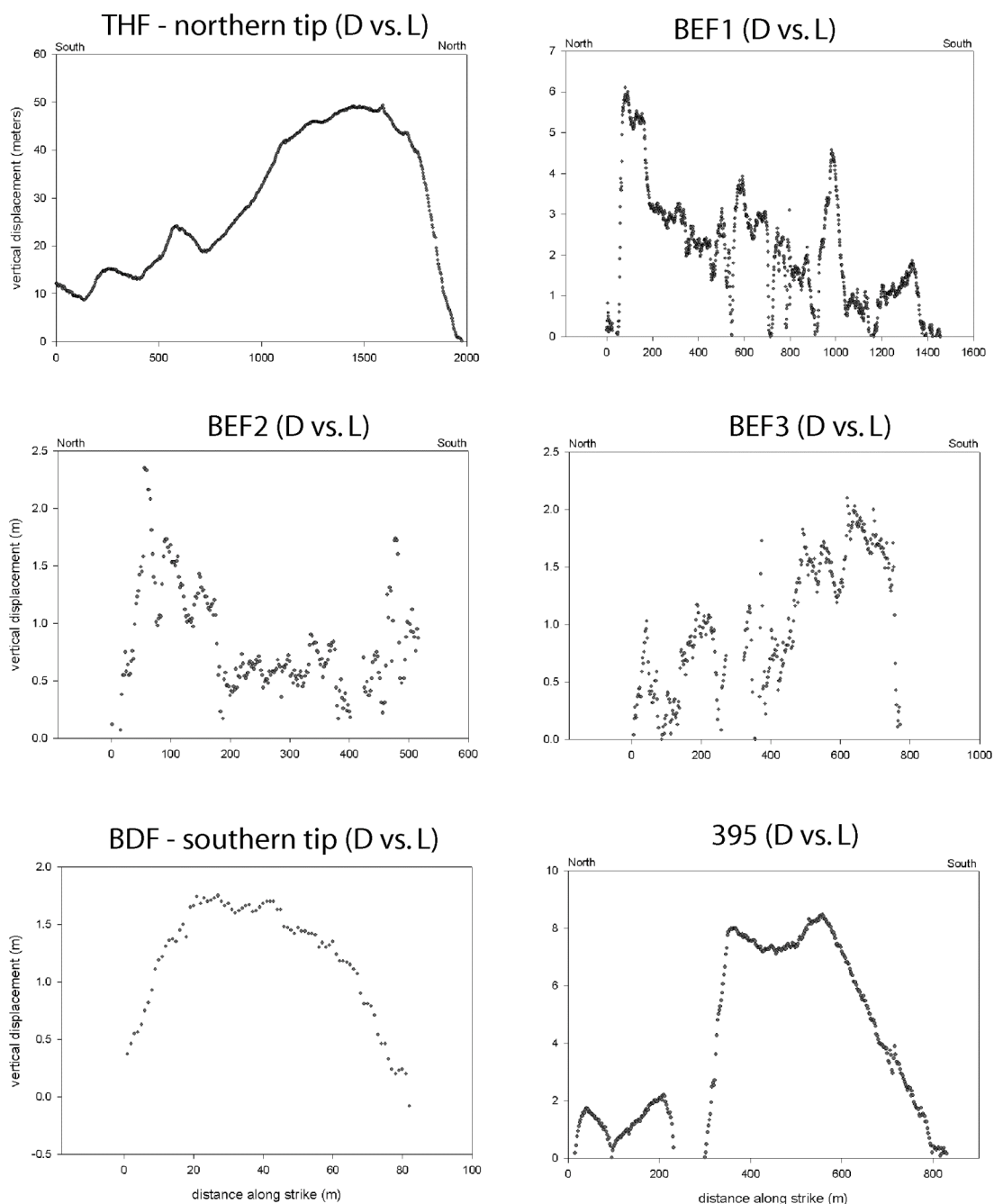
Figure A-2. Along-strike displacement versus length profiles for selected faults within northern Owens Valley. See Figure A-1 for fault locations.
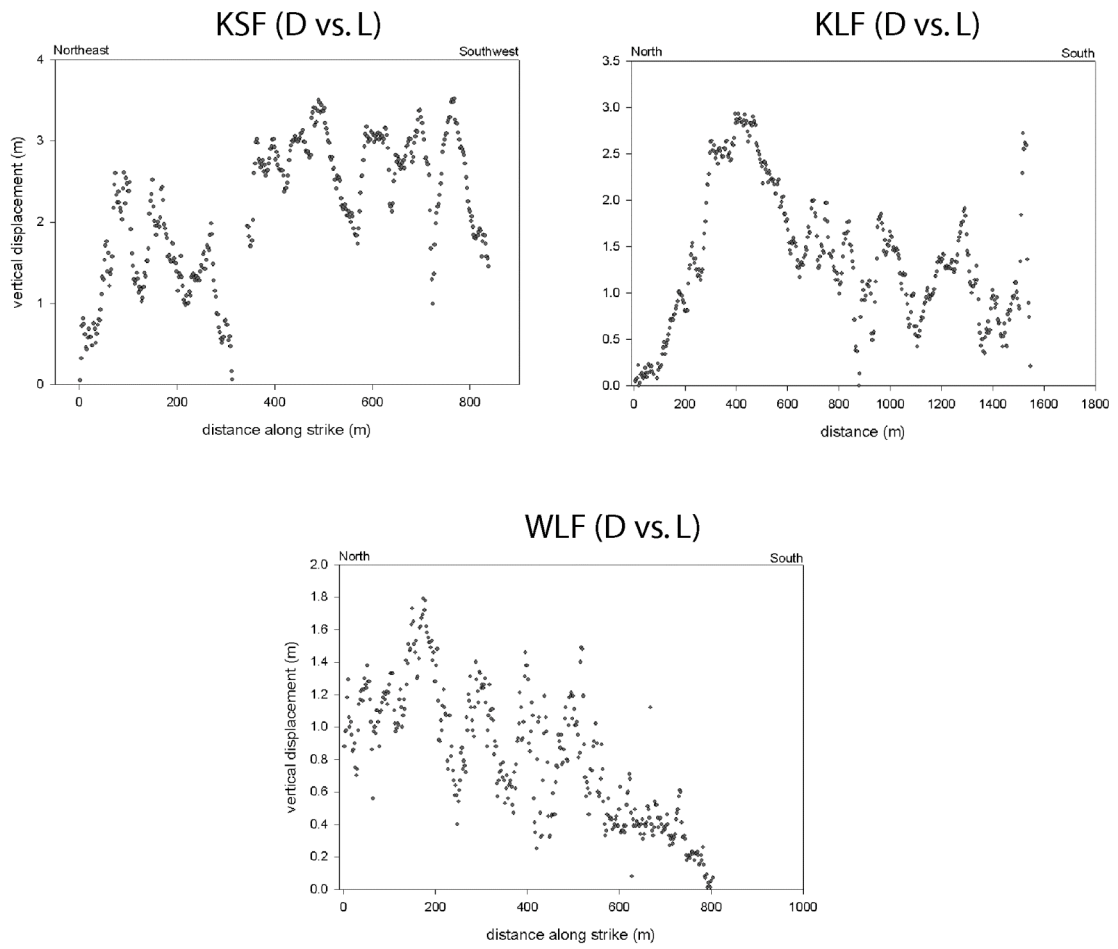
Figure A-2. (cont.)
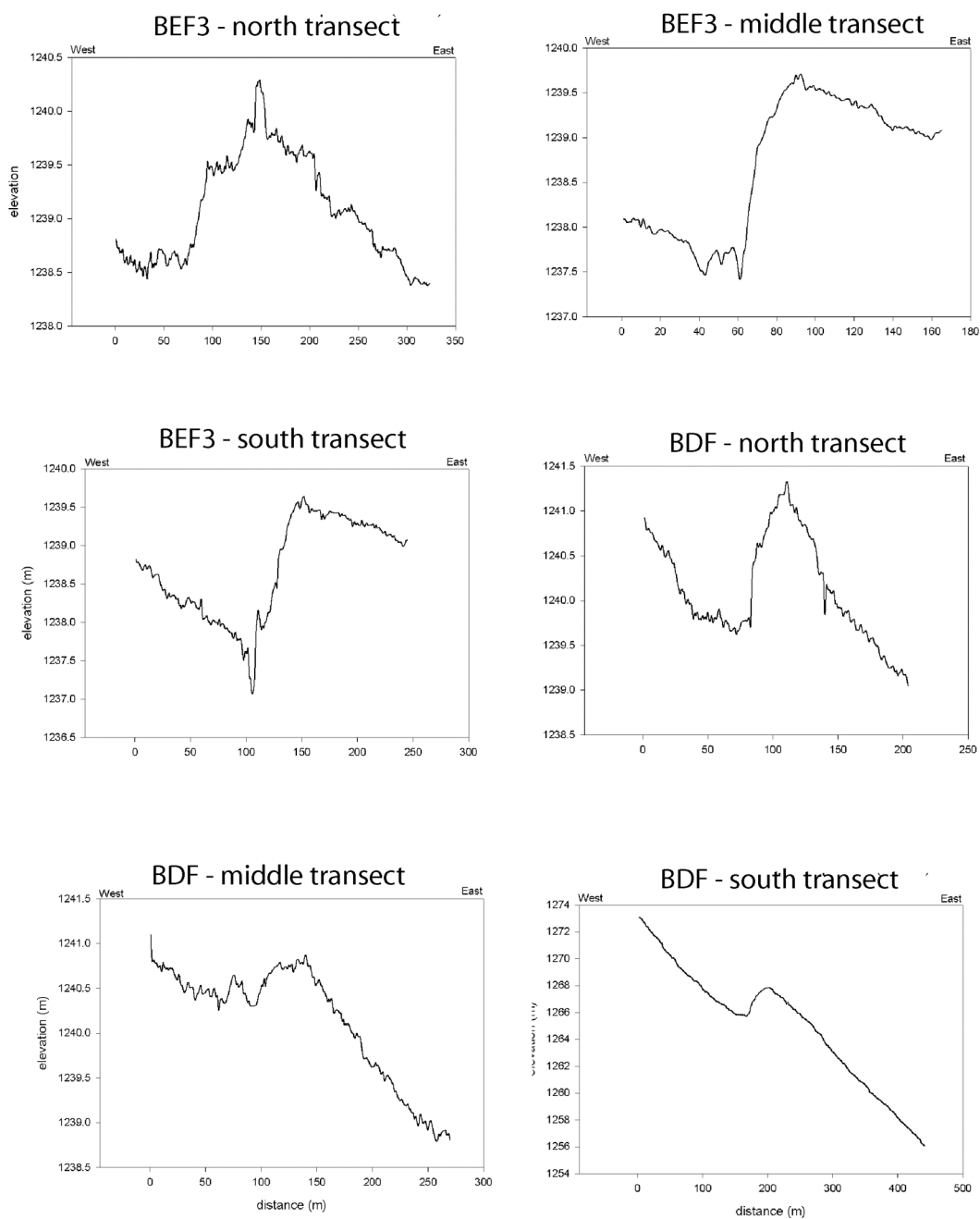
Figure A-3. Cross-strike displacement profiles for selected faults within northern Owens Valley. Multiple transects were obtained for each fault. See Figure A-1 for fault locations.
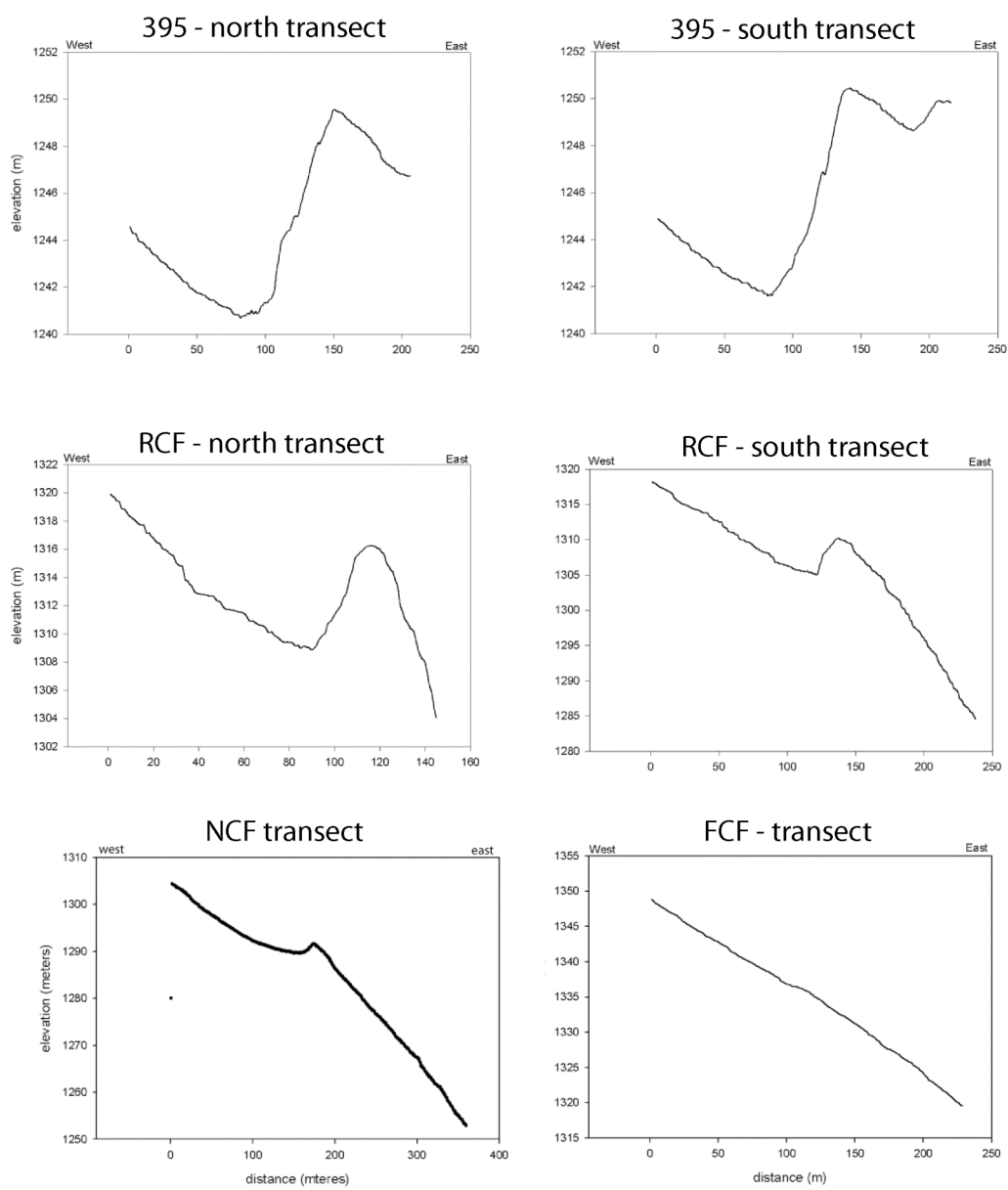
Figure A-3. (cont.)
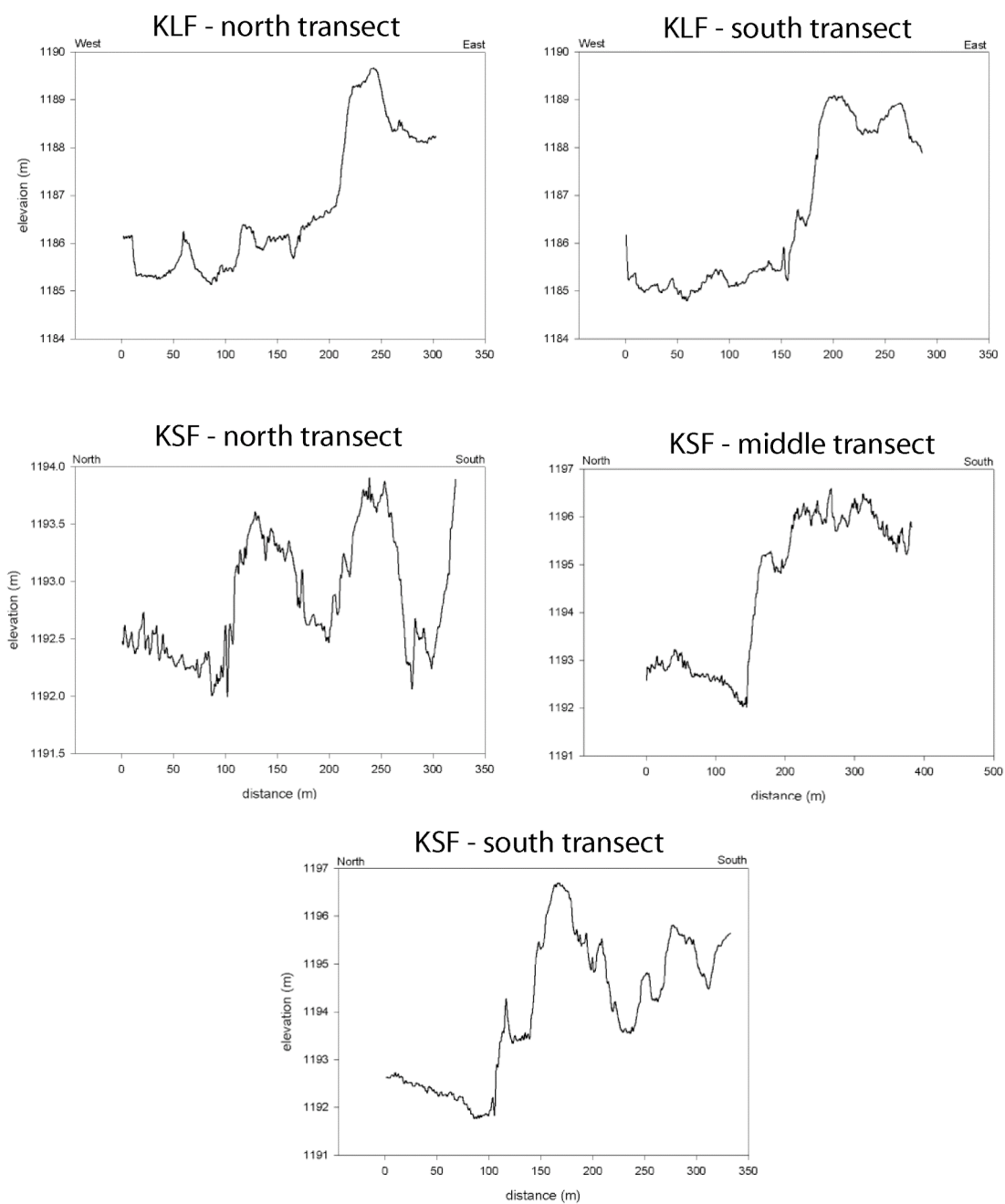
Figure A-3. (cont.)
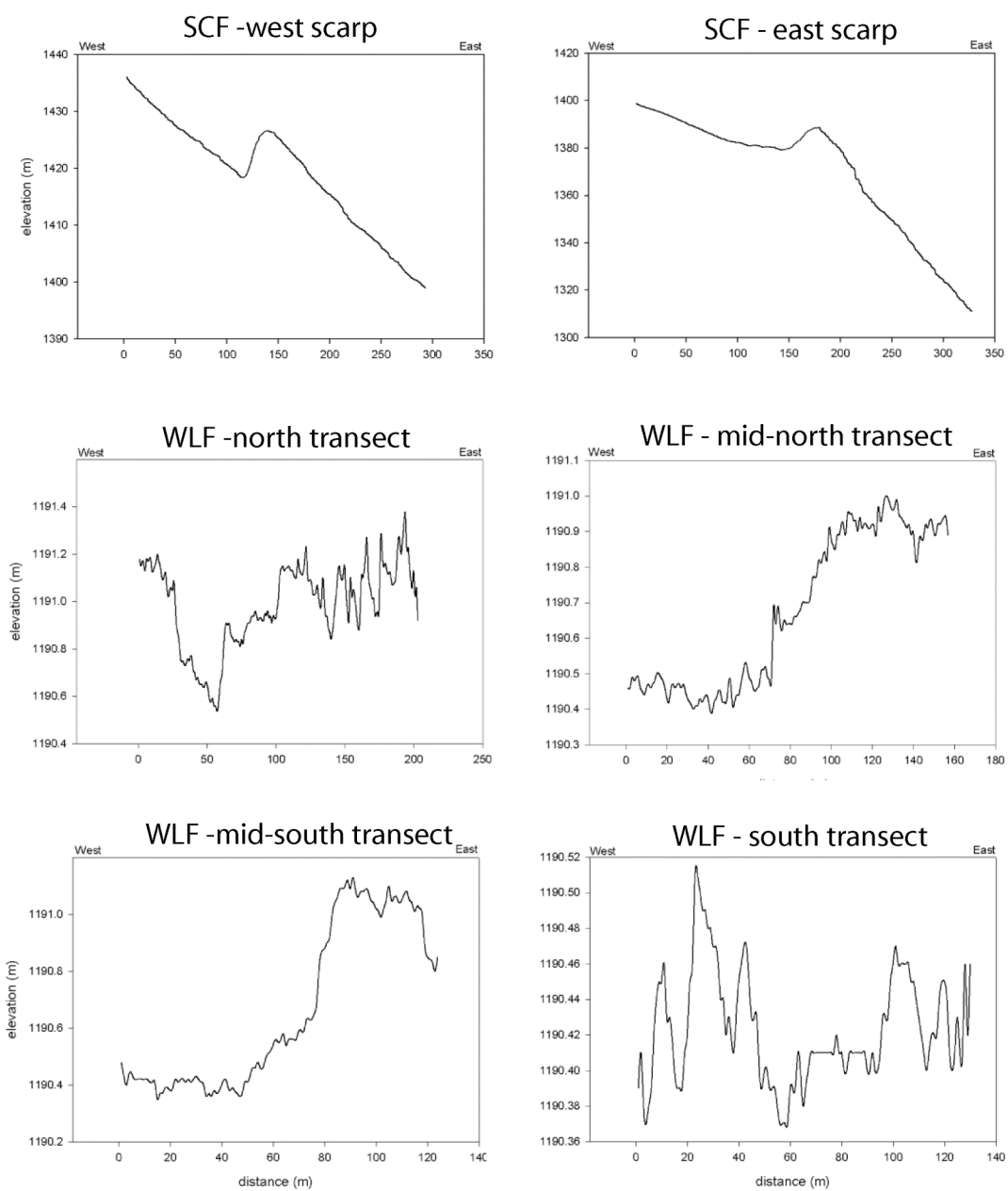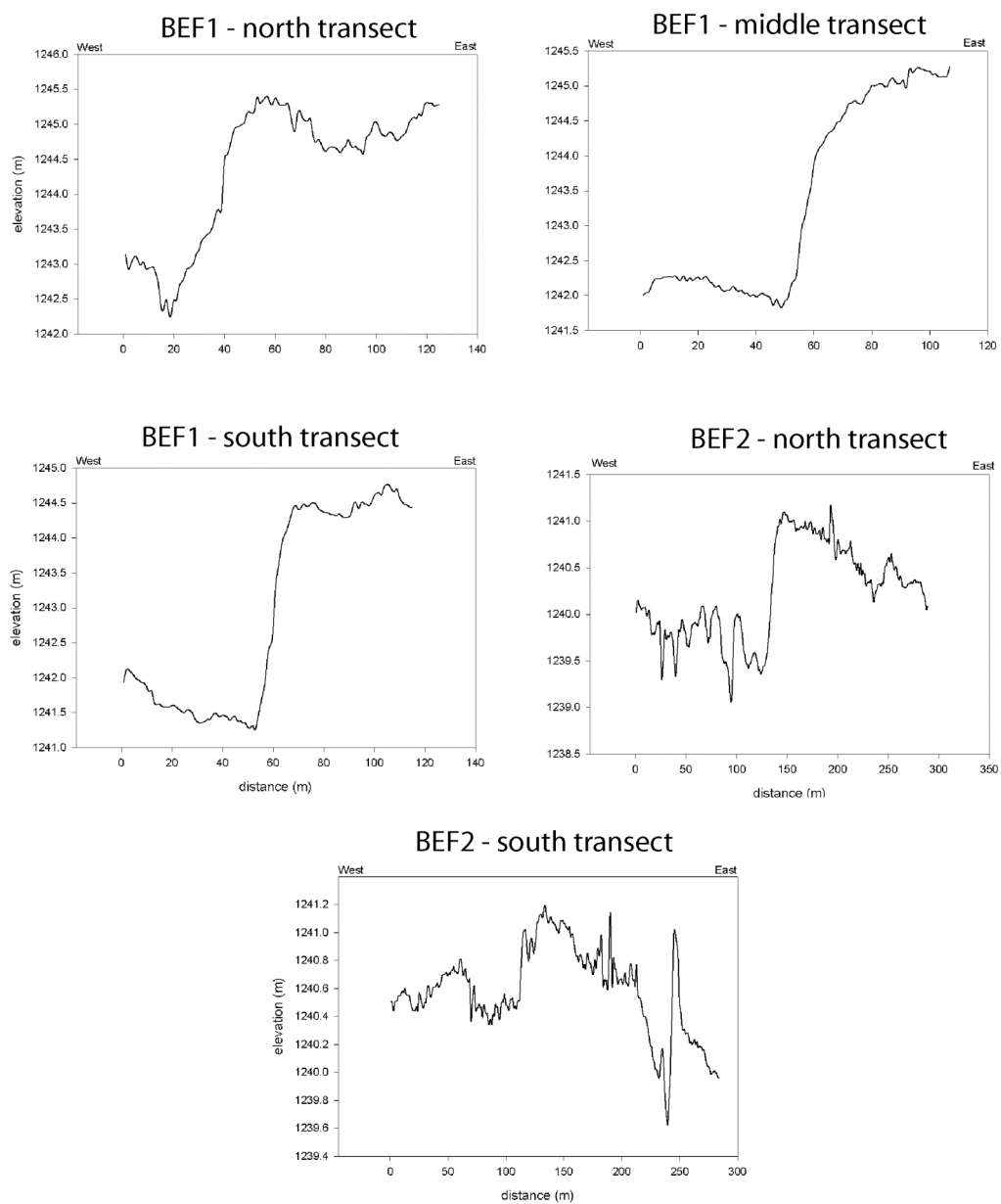
Figure A-3. (cont.)
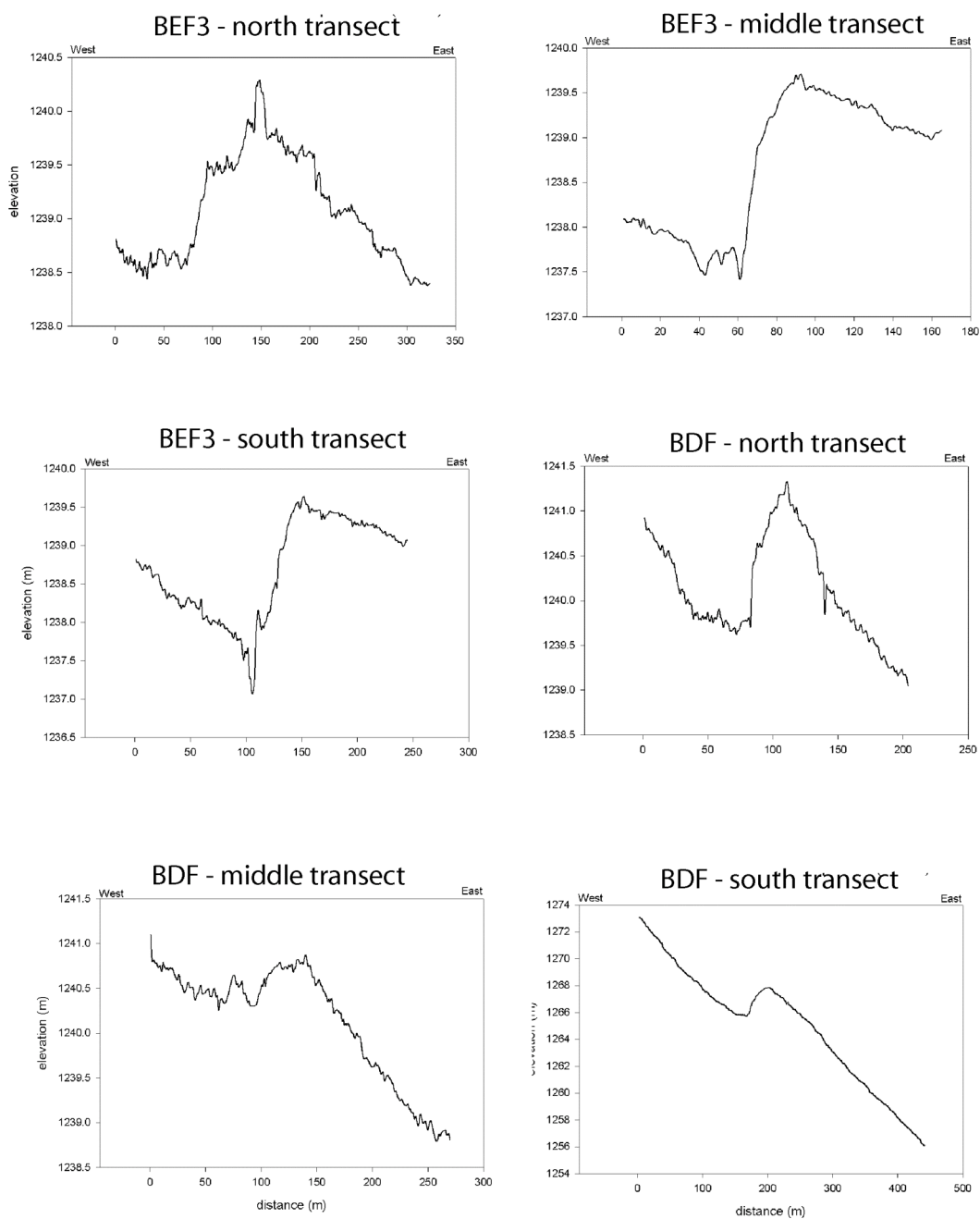
Figure A-3. (cont.)
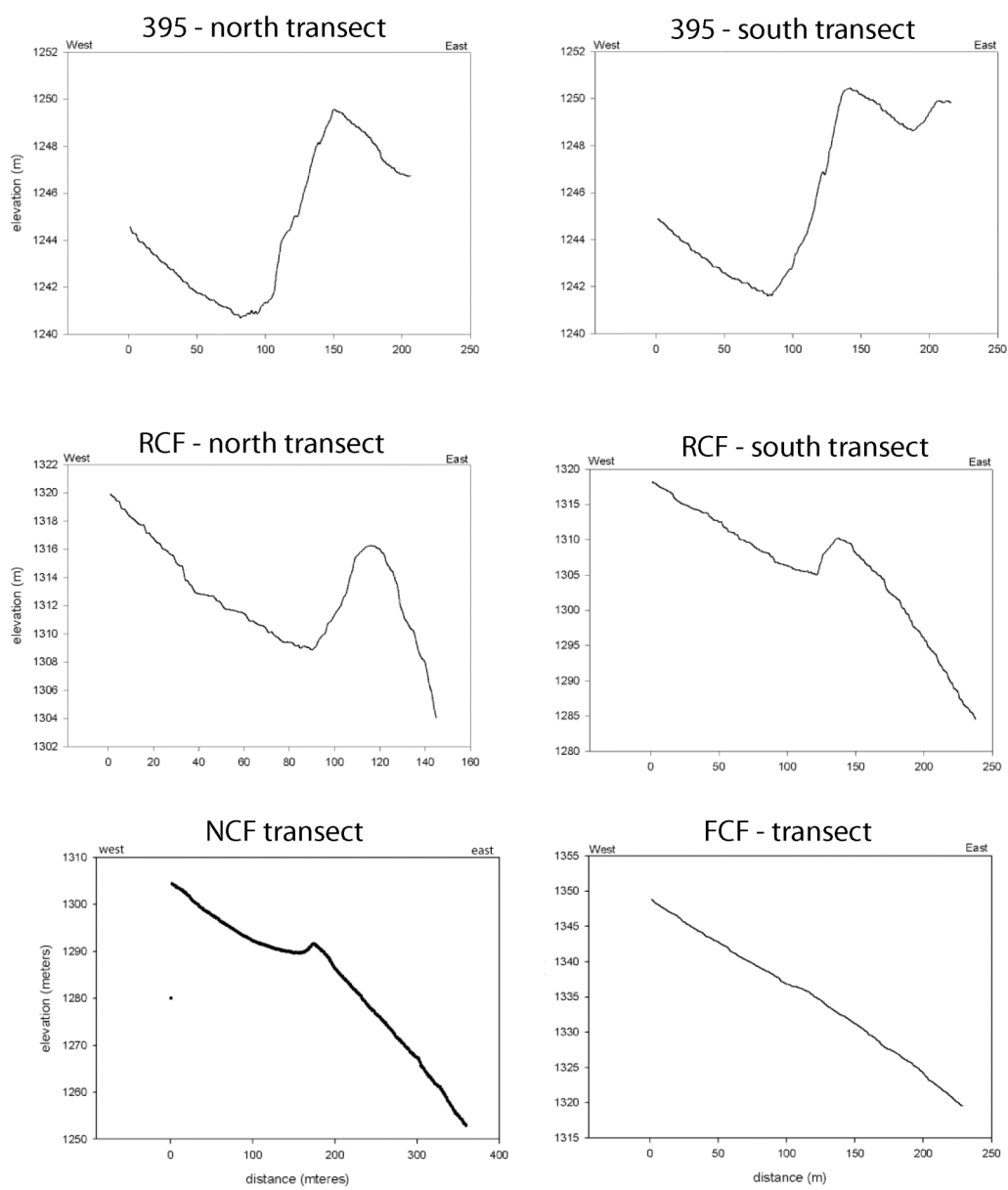
Figure A-3. (cont.)
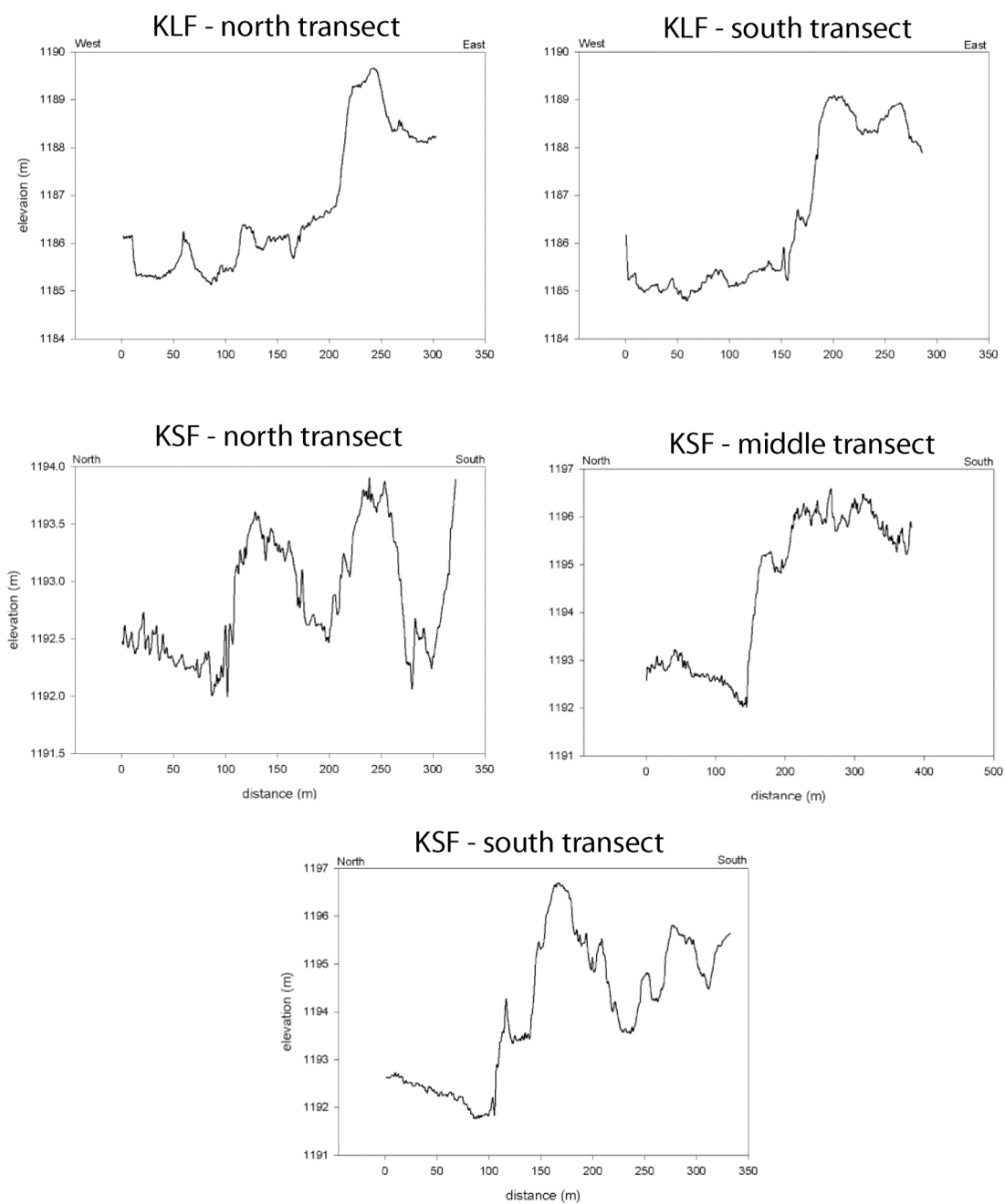
Figure A-3. (cont.)
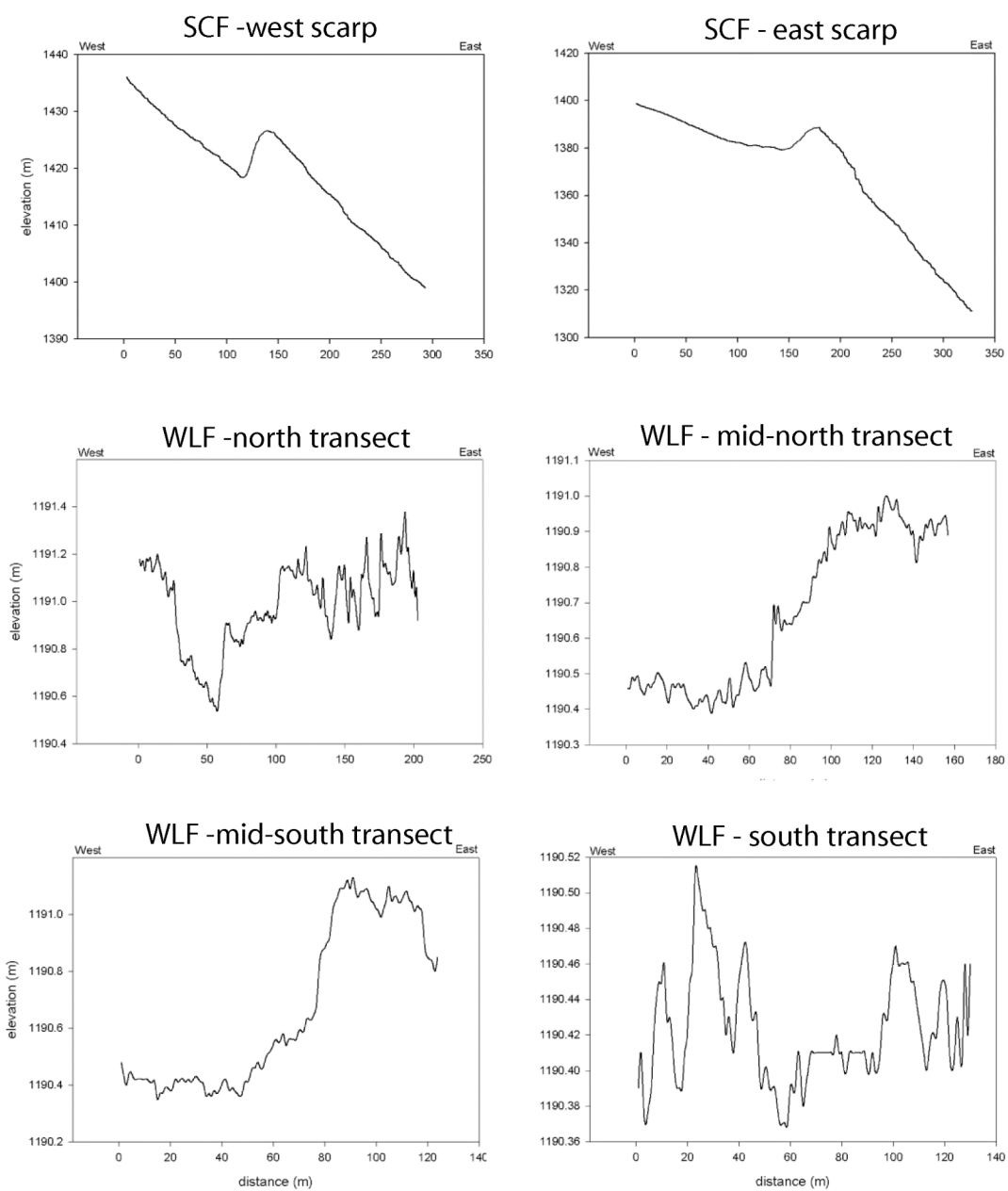
Figure A-3. (cont.)

Figure A-3. (cont.)
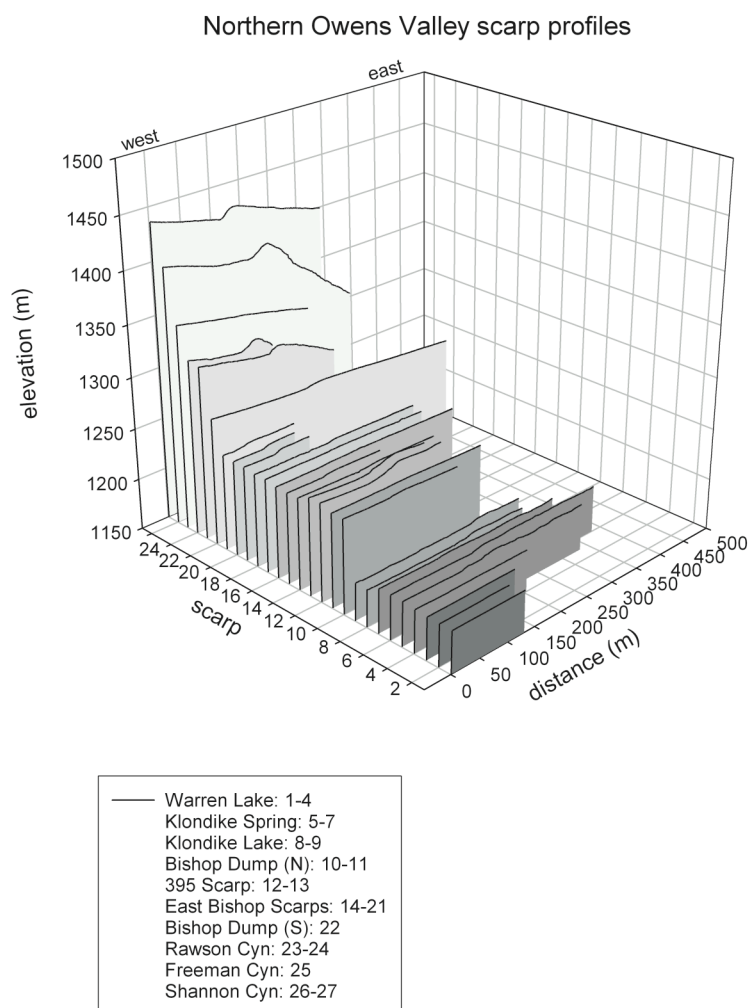
Figure A-4. Compilation of cross-strike scarp profiles from Figure A-3. See Figure A-1 for fault locations.
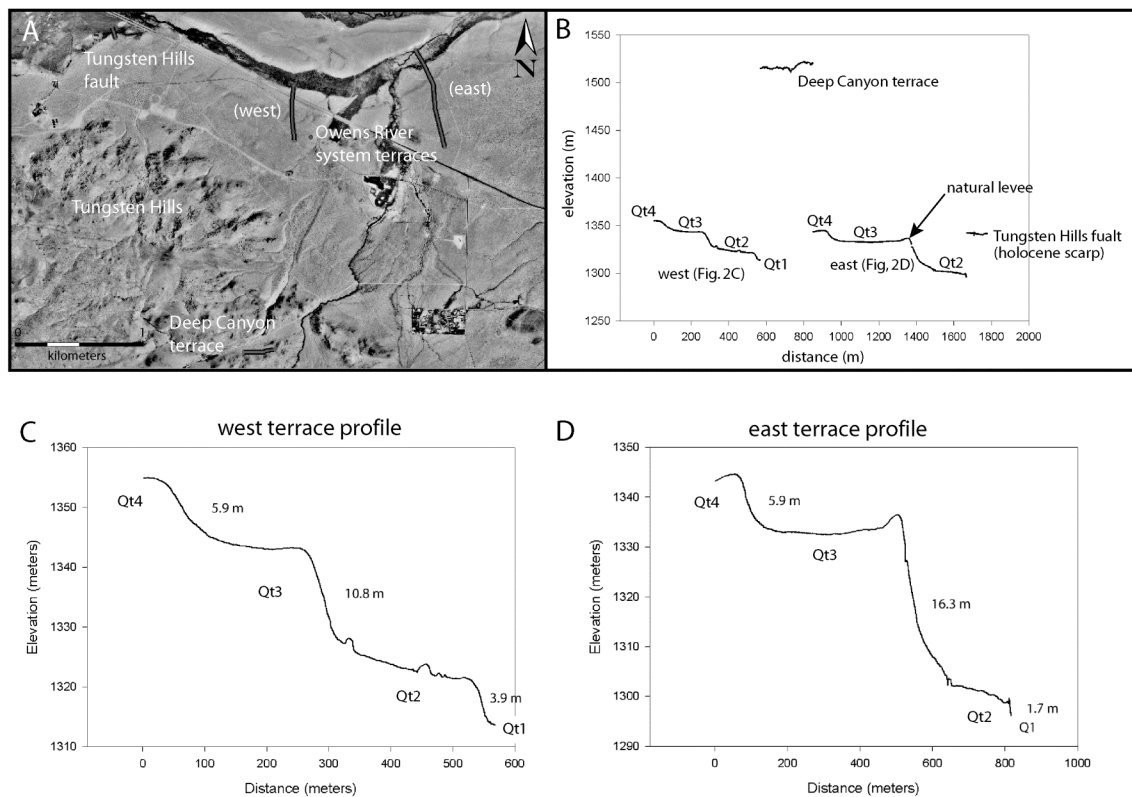
Figure A-5. (A) Location of Owens River terrace profiles. See Figure A-1 for site location. Profile locations indicated by heavy grey lines. **(B)** DPGS elevation profiles for a Holocene scarp associated with the Tungsten Hills fault, the Deep Canyon terrace, and two portions of the Owens River terraces. **(C)** Western terrace profile. **(D)** Eastern terrace profile.
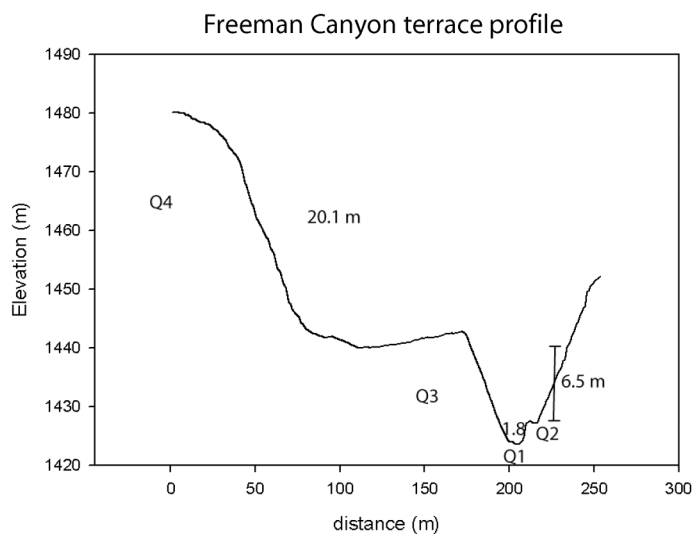
Figure A-6. DPGS transect of Freeman Canyon terraces. See Figure A-1 for site location

Appendix B

Optically Stimulated Luminescence (OSL) Age Dating

Optically stimulated luminescence (OSL) age dating is based on the measurement of electrons released from crystal matrix flaws upon exposure to light. Electrons within sediment (typically quartz sand grains) become excited, and thus jump to higher energy states when they are exposed to natural radiation emitted from nearby radioisotopes within sediment. In some instances, flaws within the crystal matrix of individual sediment grains trap the energetic electrons. The trapped electrons are extricated from these flaws through the addition of small amounts of energy, typically through exposure to light. Electrons that are trapped and then released (zeroed) in this manner emit a small amount of energy in the form of light as they return to their original energy state. By measuring both the intensity of emitted light (a proxy for the paleo-dose) from a sample, and the in situ radiation (a measure of the dose rate) to which the sample was exposed throughout burial, the time elapsed since a given sediment sample was deposited and buried can be determined (Burbank and Anderson, 2001). However, it must be assumed that the sample in question contained no trapped electrons at the time of its burial. If present at the time of burial, this "inheritance" will result in the measurement of a higher paleo-dose and subsequently a longer estimate for the duration of burial.

The validity of the above assumption hinges on the interpretation of the transport history for a given sample. For instance, sediment readily exposed to light during transport as either suspended or eolian flux will be much less likely to exhibit an inheritance than sediment transported within the bedload. Over the course of its history, from its incorporation within the parent material, to erosion, transport, deposition, and possible re-erosion and re-deposition, a given quartz grain may experience several cycles of electron accumulation and subsequent zeroing.

A further assumption must be made regarding the saturation of a sample. Samples exposed to an exceptionally high dose rate for a short period of time, or alternately, a low dose rate for an exceedingly long period of time may become saturated with excited and trapped electrons such that no further electrons will accumulate. Saturation places an upper age limit for the application of OSL dating of sediment. Even with typical dose rates, saturation limits the measurable age to ~1 Myr (Burbank and Anderson, 2001).

Results obtained from four OSL samples from northern Owens Valley are presented in Table B-1. The age obtained from the Deep Canyon sample is used in Appendix C in a discussion of drainage development associated with the Tungsten Hills fault. The ages obtained for the Owens River terrace samples (OV-OSL-04-01 and OV-OSL-04-02) are used in Chapter 4 to determine the rate of extension across the Qt2 terrace surface. A discussion of the ages returned by these two samples is presented in Appendix F. The age returned by the BEF-04-01 sample confirms the age of a Holocene terrace surface offset by a fault located east of Bishop (BEF-1) (Figure 2-4; Chapter 2).

Table B-1. Equivalnet dose (D_e) data, dose rates and OSL ages for 180-212 μm quartz

Sample	U (ppm)	Th (ppm)	K (%)	Rb (ppm)	H_2O content[2] (%)	Cosmic dose-rate[3] (mGya^{-1})	Total dose-rate (mGya^{-1})	N^1	Median D_e ± 1σ (Gy)	Modeled D_e ± 1 relative s.e. (Gy)	Age (ka)
OV-0SL-04-01	1.79±0.18	10.88±0.54	3.03±0.15	125.3±12.5	0.29	0.192	4.30±0.23	23	103.5±36.8	90.4±13.2	21.0±3.3 §
OV-0SL-04-02	7.66±0.77	17.77±0.89	2.72±0.14	116.6±11.6 6	0.23	0.192	5.86±0.31	28	51.1±24.7	36.5±10.2	6.2±1.8 §†
Deep Canyon	1.28±0.13	6.61±0.33	4.16±0.21	129.0±12.9	0.22	0.154	4.95±0.28	42	57.1±31.5	49.9±4.4	10.1±1.1 §
BEF-04-01	2.66±0.27	11.63±0.58	3.10±0.16	116.4±11.6 4	0.15	0.218	4.66±0.24	31	48.4±14.2	33.5±4.4	7.2±1.0 †

Notes:

1. Number of accepted D_e replicates.

2. Percent moisture compared to dry weight. Uncertainty is taken as 5%.

3. Cosmic dose-rate calculated assuming constant burial depth using method described in Prescott and Hutton (1994). Uncertainty is taken as 5%.

§ Ages calculated using D_e derived from Finite Age Model (FAM) and a single component solution (Galbraith, 1999).

† Ages calculated using D_e derived from FAM and first component solution (Galbraith, 1999).

‡ Age calculated using median D_e with 1σ error.

Appendix C

Influence of Fault Development on Drainage Evolution within Northern Owens Valley

Introduction

Several active faults within northern Owens Valley traverse drainages of the Sierra Nevada Mountains. As such, faulting has significantly influenced local drainage patterns by redirecting stream and debris discharge from the mountain front. Prominent examples of this exist along the western margin of the Tungsten Hills, the eastern margin of the Coyote Warp, and in the vicinity of the town of Bishop. Here I document several of these examples.

The Tungsten Hills and Deep Canyon

The Tungsten Hills are draped with an extensive network of abandoned drainage channels (Figure C-1). Deep Canyon, the largest of these paleo-drainage channels, is characterized as a prominent bedrock canyon exhibiting more than ~200 m of vertical incision as measured from the current bedrock channel to the adjacent bedrock highs within the Tungsten Hills. The considerable depth of Deep Canyon combined with the lack of an active perennial stream suggests the canyon once accommodated some greater amount of stream flow than at present. Many prominent wind gaps in the vicinity of Deep Canyon indicate that, throughout its development, the course of stream flow has changed several times. The culmination of this development was the complete abandonment of the canyon.

The upstream extent of Deep Canyon, located within the western portion of the Tungsten Hills, is comprised of two prominent bedrock forks: a northern fork and a southern fork, which each project upstream to the currently active channels of Horton and McGee Creeks, respectively (Figure C-1). Given their orientation with respect to Deep Canyon, these two creeks are the most probable sources of paleo-flow across the
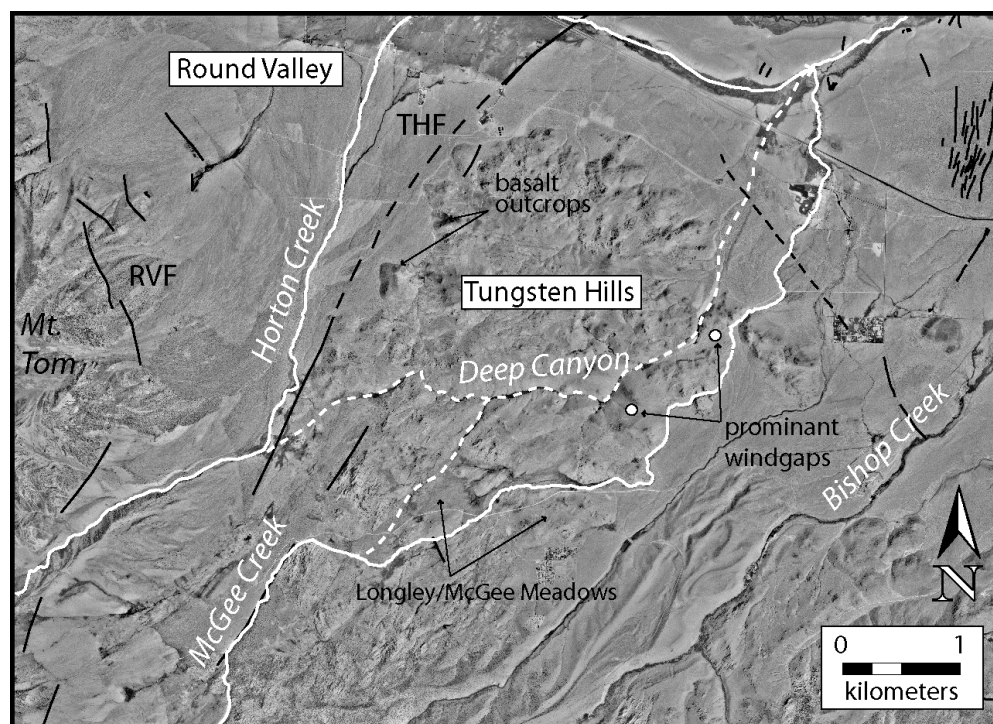
Figure C-1. The development of the Tungsten Hills fault (THF) has influenced the drainage pattern of both Horton and McGee Creeks. Deep Canyon once provided the primary outlet for drainage across the Tungsten Hills prior to stream diversion. Several windgaps located within the Tungsten Hills indicate the course of Deep Canyon has changed several times throughout its development. A prominent basalt dike located along the western margin of the Tungsten Hills dips ~60° to the west. The dike exploited the relative structural weakness associated with the THF, and thus likely defines its attitude.

Tungsten Hills. Moreover, given the width of the southern fork, which is almost three times that of the northern fork, McGee Creek was likely the dominant contributor to paleo-flow.

The modern active drainage patterns of both McGee and Horton Creeks also provide an indication that they each previously coursed via Deep Canyon. The catchment basin presently drained by Horton Creek is situated in a minimally glaciated hanging-valley located between Mt. Tom and Basin Mountain (Figure 2-2, Chapter 2). Horton Creek flows approximately northeast from the Sierran range-front to the western margin of the Tungsten Hills. The upper portion of Horton Creek projects in line with a small alluviated embayment within the Tungsten Hills, which heads the northern fork of Deep Canyon (Figure C-1). Small abandoned alluvial channels are preserved throughout this embayment, which narrows to the east from a relatively broad, alluviated plain, to the constricted bedrock channel of the north fork of Deep Canyon. Intriguingly, the point where Horton Creek reaches the projected surface trace of the THF, the active stream channel turns abruptly to the north. The coincidence of these features suggests Horton Creek once contributed discharge through Deep Canyon; however, due to relative uplift across the THF outpacing stream incision, flow was diverted northward around the Tungsten Hills.

While Horton Creek was completely diverted around the THF footwall block, McGee Creek appears to have incised at such a pace that it was able to continue its course across the developing fault (Figure C-1). The catchment for Magee Creek is situated between Mt. Basin and Mt. Humphreys from which it flows to the northeast towards the southwestern portion of the Tungsten Hills. McGee Creek follows the

southern-most surface trace of a small segment of the THF for a short distance, and then turns east across the fault (Figure 2-2, Chapter 2). Several meters of bedrock incision are apparent very near where the creek crosses the inferred fault trace. Downstream of the fault, McGee Creek flows into a small perched alluvial valley (Longley/McGee Meadows), which exhibits relatively low internal relief (Figure C-1). There is little evidence for recent bedrock incision within the valley, as much of the underlying bedrock is mantled with a veneer of Late Pleistocene alluvium (Bateman, 1965).

Several young, abandoned channels within Longley/McGee Meadows indicate this area is experiencing some degree of unequilibrium with respect to its drainage pattern (Figure C-1). The abundance of alluvial cover, and its relatively low elevation gradient with respect to much of the surrounding drainage and alluvial passages within in, and around the Tungsten Hills, suggests that the base level to which McGee creeks responds is presently experiencing a relative rise, similar to that already experienced by Horton Creek. Such a change in base level may be attributed to relative uplift of the THF footwall block, the resulting decrease in stream gradient, and the subsequent promotion of alluvial aggradation. Given its relatively low discharge, it is doubtful McGee Creek will retain its present course across the THF. Continued uplift along the THF will likely contribute to the deflection of McGee Creek such that it eventually joins with Horton Creek.

Deep Canyon Stratigraphy

Stratigraphic relationships within Deep Canyon provide a relative, though limited, chronology of recent drainage evolution across the Tungsten Hills, and by inference, yield potential insight into the development of the THF (Figure C-2). The presence of
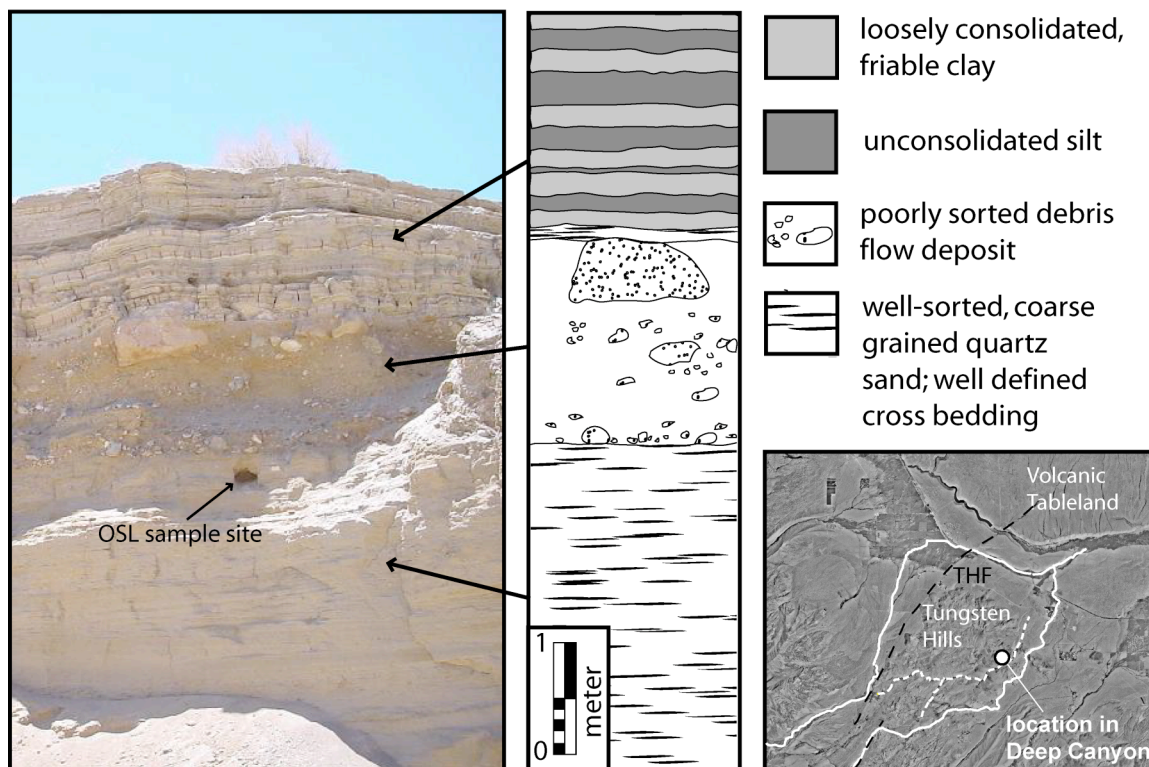
Figure C-2. Stratigraphic section from Deep Canyon exhibits three distinct stratigraphic units indicative of three separate depositional regimes. The lower unit, consisting of well-sorted coarse-grained quartz sand, reflects perennial stream activity active during an earlier period when Horton and/or McGee Creeks fed into Deep Canyon. A sample from this unit submitted for OSL analysis returned an age of 10.1 ± 1.1 ka. This age approximates the abandonment age of Deep Canyon by early perennial stream activity. The middle unit is composed of poorly sorted debris flow units suggestive of periodic activity. This unit likely reflects a transitional stage, when Horton and McGee creeks utilized Deep Canyon during periods of exceptionally high discharge. The upper unit of finely laminated silt and clay layers was deposited during historical times after construction of an earthen dam used to support mining activity.

two primary stratigraphic units within Deep Canyon, a fluvial unit and a debris flow unit,

reflects a distinct change in the drainage processes that have acted within the canyon.

The lower of the two main units is composed entirely of well-sorted, relatively coarse-

grained, quartz sand, which was derived from the surrounding granodioritic bedrock of

the Tungsten Hills and Sierra Nevada mountains. Cross-bedding within this unit is

visible within several outcrops with inclusions of heavily calcified detrital plant material.

Given similar stratigraphic observations in presently active nearby drainages, this unit

likely reflects an earlier, though relatively recent, period of perennial stream activity. A

sediment sample taken from this unit near its contact with the overlying

debris flow unit returned an OSL age of 10.1 ±1.1 ka (Figure C-2 and Table B-1,

Appendix B). Based on the stratigraphic location of the sample, we suggest this age

approximates the abandonment age of Deep Canyon by the perennial stream. However,

it remains unclear whether such abandonment is due to fault development or to a decrease

in fluvial output linked to climatic fluctuations, such as those associated with the waning

stages of glaciation. We note that the contact between the lower fluvial sand unit and the

upper debris flow unit is very sharp and unconformable, suggesting a rapid shift from one

depositional environment to the other. Based on this observation, it seems probable that

this shift may have been related to seismic activity along of the THF. However, without

a paleoseismic record for the THF, it is unlikely the observed depositional shift can be

assigned to a discrete seismogenic event.

The upper debris flow upper unit consists of very poorly sorted angular and

stream rounded clasts ranging in size from silt to meter scale boulders. Much of this

material comes from the adjacent Sierra Nevada as opposed to from within the Tungsten

Hills. This unit reflects several episodes of debris flow advances deposited during the intermittent reactivation of Deep Canyon as a viable drainage pathway. The debris flow advances initiated some time after ~10 ka. Moreover, based on the observation of a thin capping layer (~2 m thick) of alternating silt and highly laminated clay (deposited subsequent to the construction of an earthen retaining dam used to support early-mid century mining activity), debris flows likely continued within Deep Canyon as late as a century ago. This inference is supported by the observation of a fully intact *Artemisia tridentate* (Great Basin Sage Brush) that has roots extending down into the lower debris flow unit, and its branches extending into, and locally disturbing the laminar sedimentation processes active during deposition of the silt and clay layers.

Coyote Warp Drainages

The eastern margin of the Coyote Warp exhibits several moderate sized alluvial fan units, which extend transverse to the grain of range-font faulting. Many of the west-dipping faults along the Coyote Warp displace these Late Pleistocene fan units resulting in marked changes in local drainage patterns. Prominent examples of this interaction occur at Rawson Canyon, Keough Canyon, and Shannon Canyon (Figure 2-2, Chapter 2).

The fan oldest fan surface associated with Rawson Canyon is displaced vertically at two locales by two overlapping, west-dipping normal fault segments (RCF, Appendix A). Each of the fault scarps has deflected Rawson Creek (Figure C-3). Several incised channels are preserved within the footwall of the eastern scarp. These serve as primary indicators for paleo-flow across the fault prior to diversion. Furthermore, the fan surface exhibits several small, yet distinct water gaps visible in the scarp crest along-strike.

Keough Canyon is located south of Rawson Canyon, near the fault-controlled
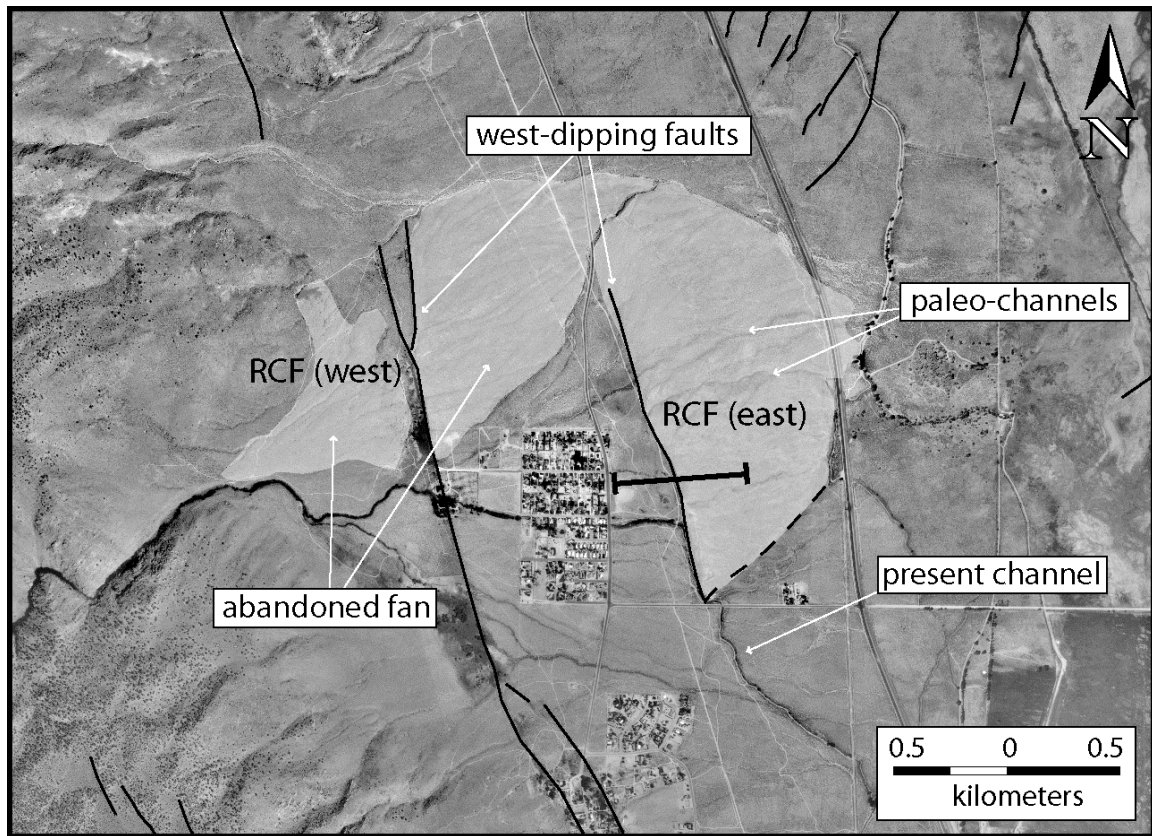
Figure C-3. The Rawson Canyon Fault (RCF) consists of two west-dipping fan segments that displace a Late Pleistocene fan surface. Activity along this fault has diverted Rawson Creek several times during its development.

Keough Hot Springs. Recent faulting at the mouth of the canyon has clearly influenced

the drainage pattern of Keough Wash (Figure C-4). The oldest preserved fan unit in this

area is displaced by ~2 m by the west-dipping Keough Canyon fault (KCF), which

has juxtaposed the older unit against a younger fan unit located on the hangingwall

(Appendix A). No age constraints beyond this relative distinction were obtained for these

fan units, and thus an inferred fault slip rate was not derived.

The southern portion of the KCF forms an alluvial scarp that is clearly visible in

this area. Within the scarp footwall there is a prominent beheaded paleo-channel

suggesting flow once coursed due east from the bedrock canyon (Figure C-4). However,

drainage has since been diverted to the north through a bedrock channel, which has been

incised through the scarp, as well as to a lesser extent, around the scarp to the south.

Considering the bedrock exposure of the northern channel it is judged to be the

predominant route for drainage in this area, however, no perennial stream was observed

to confirm this inference. North of the incised channel, the fault scarp changes from an

alluvial scarp to a purely bedrock scarp. The footwall is composed of granodiorite

similar to that in the adjacent range, and exhibits a pervasive joint set similar to that

observed within much of the bedrock exposure along the Coyote Warp.

Bishop Creek drainage

Intra-valley faulting in the vicinity of the town of Bishop has influenced the

drainage patterns of both Owens River and Bishop Creek (Figure 2-4, Chapter 2).

Several small, west-dipping normal fault segments, primarily those labeled Bishop East

faults 1-3 (BEF 1-3), have contributed to offsetting a Holocene age terrace deposit, and

have resulted in marked channel incision and diversion (Bateman, 1965). A sediment
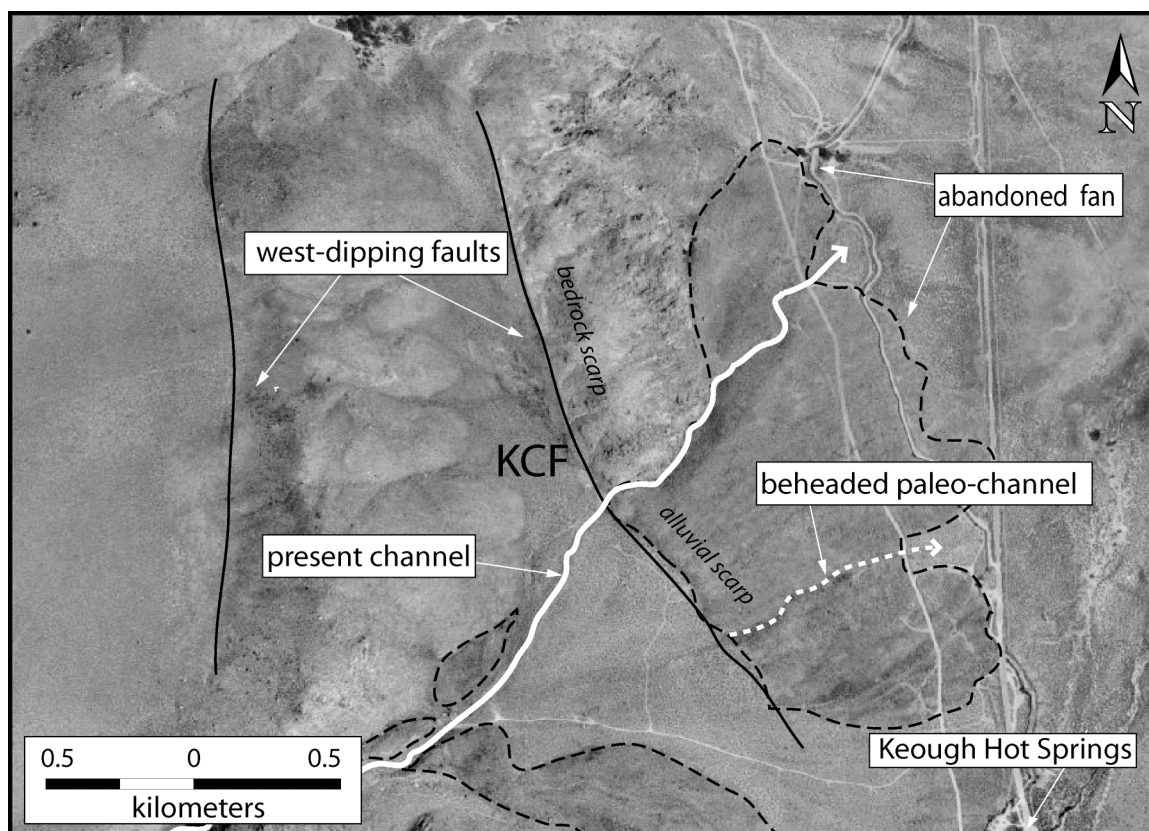
Figure C-4. The west-dipping Keough Canyon fault (KCF) vertically displaces a Late Pleistocene fan surface at the mouth of Keough Canyon. Activity along this fault has resulted in the uplift and abandonment of the fan surface, which preserves evidence of paleo-drainage across its upper surface. The scarp consists of bedrock to the north and fan material to the south.

sample obtained from the footwall of the BEF-1, and submitted for OSL analysis returned an age of 7.2 ± 1.0 ka, thus confirming Holocene age of the terrace (Figure 2-4 and Table B-1, Appendix B).

The terrace unit in this area is locally mantled with extensive eolian sand deposits; however, several small paleo-drainage channels are still visible within its upper surface. Several of the currently active drainage channels of Bishop Creek appear in stark contrast to the surrounding terrace units due to differences in vegetation cover. These active channels have maintained a relatively stable water table for vegetation growth through successful breachment of the developing scarps. The channels have subsequently been confined to vertical incision at their respective breach points, as opposed to lateral meandering. The development of faulting in this area has also contributed to the confinement of the Owens River to its established channel. Such confinement is apparent near the northern tip of the BEF 1, where relatively few meander belts are observed. The appearance of this portion of Owens River lies in contrast to that of the remainder of its course, where extensive meandering is observed within the surrounding alluvial cover.

Appendix D

Bishop Fault Cross-Section and Stratigraphic Section Unit Descriptions

Presented here is the method for documenting the Bishop Fault cross-section illustrated in Figure 2-6 (Chapter 2), as well as a brief descriptions of the sedimentary units present. The outcrop described here was created with a bulldozer along the southernmost excavation pit wall in the Inyo County Bishop-Sunland Municipal landfill. The cross-section was oriented perpendicular to the fault strike of north-northeast. A wire mesh was fixed to the outcrop in order to provide scale (Figure D-1). The outcrop was sketched and photographed in detail (Figure D-2 and D-3). Samples representative of each of the varied lithologic components were obtained for later description.

The section is cut by two fault planes (Figure D-3 and 2-C, Chapter 2). Three distinct sedimentary units have been juxtaposed by activity along these fault planes. The oldest unit (left side, Figure 2-6; Chapter 2) is composed primarily of fine to coarse-grained quartz sand. Cross bedding is prevalent throughout a coarse sand layer in the lower part of the unit. This layer is interspersed with pockets of reworked ash and lenticular lenses of well-sorted pebble sized pumice clasts. Towards the upper part of the unit, lithology becomes more variable with a small discontinuous layer of partially consolidated light brown silt with biotite inclusions. The entirety of this unit is interpreted to be primarily of fluvial origin likely related to an outwash channel of Bishop Creek where similar deposits exist within the active channel and depositional banks. It in unclear whether the occurrence of pumice clasts within this unit reflects contemporaneous stream and volcanic activity, or reworking of a previously deposited pumice unit.

The middle section (center, Figure 2-6, Chapter 2) is composed almost entirely of unconsolidated fine sand with inclusions of biotite. Where locally consolidated, the

lithology changes color to a darker shade. Depositional structure is wholly unrecognizable within this unit, however, inclusions of coarse to medium oxidized sand lenses indicate the unit may have been subjected to post depositional deformation and alteration. This unit is interpreted to represent a transitional fluvial deltaic period, possibly a transition zone where Bishop Creek drained into one of the many pluvial lakes evident from core data (Bateman, 1965; Hollet et al., 1991)

The youngest section (right, Figure 2-6; Chapter 2) is composed of alternating layers of consolidated light brown clay and poorly sorted, partially lithified and oxidized grus deposits. Relatively intact clasts of weathered granite cobbles and coarse angular gravels are interspersed throughout the grus layer. This unit represents a progradational fan unit similar to the present day upper exposed surface. The clay layer likely reflects on-lapping of a pluvial depositional regime, or possibly, syntectonic depositional bedding that may have accumulated through periodic fault damming of Bishop Creek.
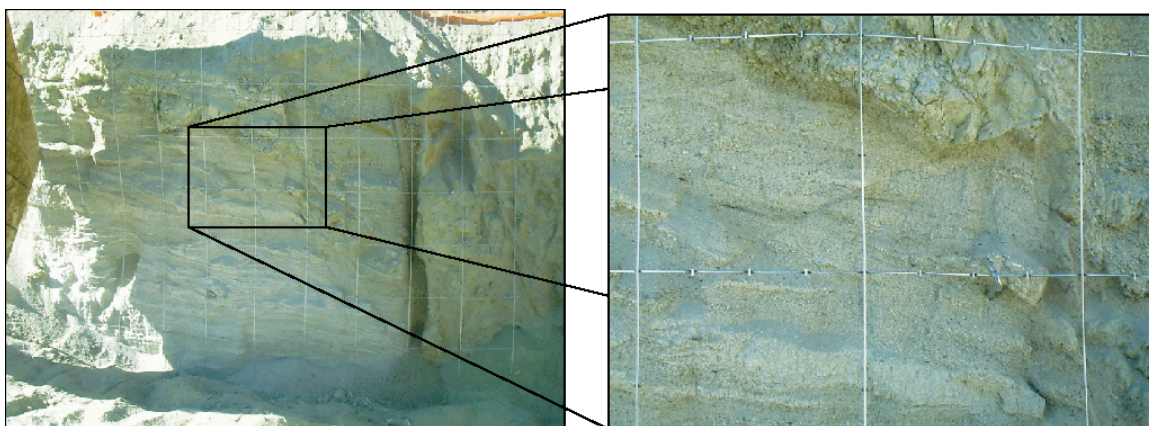
Figure D-1. Photographs of the Bishop fault outcrop. A wire mesh was used for scale during documentation.

Figure D-2. Initial field sketch of the Bishop fault cross section.

Figure D-3. Photographs of the main fault plane of the Bishop fault (view is in cross-section).

Appendix E

Fault Throw and Heave Derived from DGPS Transects of the Volcanic Tableland and Owens River Terraces

fault	half-offset (m)	throw (m)	heave 60° dip (m)	heave 70° dip (m)
tuff-1	6.4	12.8	7.39	4.66
tuff-2	3.7	7.4	4.27	2.69
tuff-3	15.2	30.4	17.55	11.06
tuff-4	2.5	5	2.89	1.82
tuff-5	18.7	37.4	21.59	13.61
tuff-6	7.4	14.8	8.54	5.39
tuff-7	7.2	14.4	8.31	5.24
tuff-8	1.9	3.8	2.19	1.38
tuff-9	1.6	3.2	1.85	1.16
tuff-10	2.3	4.6	2.66	1.67
tuff-11	5.4	10.8	6.24	3.93
tuff-12	5.9	11.8	6.81	4.29
tuff-13	1.2	2.4	1.39	0.87
tuff-14	10.1	20.2	11.66	7.35
tuff-15	7.6	15.2	8.78	5.53
tuff-16	1.7	3.4	1.96	1.24
tuff-17	6.9	13.8	7.97	5.02
tuff-18	9.8	19.6	11.32	7.13
tuff-19	3.8	7.6	4.39	2.77
Q3-1	2	4	2.31	1.46
Q3-2	2.6	5.2	3.00	1.89
Q3-3	1.6	3.2	1.85	1.16
Q3-4	2.4	4.8	2.77	1.75
Q3-5	1.5	3	1.73	1.09
Q3-6	2.2	4.4	2.54	1.60
Q3-7	1.8	3.6	2.08	1.31
Q3-8	3.1	6.2	3.58	2.26
Q3-9	2.3	4.6	2.66	1.67
Q3-10	1.4	2.8	1.62	1.02
Q2-1	0.9	1.8	1.04	0.66
Q2-2	0.5	1	0.58	0.36
Q2-3	0.4	0.8	0.46	0.29
Q2-4	0.5	1	0.58	0.36
Q2-5	0.7	1.4	0.81	0.51
Q2-6	1	2	1.15	0.73
Q2-7	1.3	2.6	1.50	0.95
Q2-8	0.4	0.8	0.46	0.29
Q2-9	0.6	1.2	0.69	0.44
Q2-10	0.5	1	0.58	0.36

transect	# of faults	cumulative throw (m)	average throw (m)	throw range(m)
Volcanic Tableland	19	238.6	12.6	2.4 - 37.4
Qt3	10	41.8	4.2	2.8 - 6.2
Qt2	10	13.6	1.4	0.8 - 2.6

Table E-1. Fault throw and heave derived from DPGS transects of the Volcanic Tableland and Owens River terraces. Half-offset is equal to half of the total throw (vertical displacement). Heave is calculated based on throw and specified dip angle. See Figures 4-1 and 4-2 (Chapter 4) for fault locations.

Appendix F

Methods and Data for Optically Stimulated Luminescence (OSL) Age Dates Derived for the Qt2 Terrace Surface in Northern Owens Valley

Two fine-grained sediment samples from the Qt2 surface (Figure 4-1A; Chapter 4) were submitted for OSL analysis. Results are displayed in Table F-1. Despite the close proximity of these samples (~2 m), they exhibit significantly different ages. Sample OV-OSL-04-01 provides our preferred age used in the strain calculations in Chapter 4. Below is an explanation for why sample OV-OSL-04-02 is disregarded.

Sample OV-OSL-04-01 has a consistent luminescence behavior and there is no evidence of partial bleaching. The equivalent dose (D_e) data were modeled using Galbraith (2006) finite age modeling technique and a single component was chosen as the best fit. Sample OV-OSL-04-02 exhibits distributed behavior and a two-component finite age model has been chosen as the best fit (Figure F-1). The cause of the range in D_e values for this sample may be due to the presence of the Bishops Ash rhyolitic tuff within these samples: OV-OSL-04-02 has very high uranium and thorium concentrations relative to OV-OSL-04-01 and dose heterogeneity within and around the sample may account for the elevated annual dose rate for this sample. The dose rates from the environmental radiation due to U, Th, K and Rb were measured using ICP-MS (Table F-1). Due to the above reasons, OV-OSL-04-02 was not used in the strain rate calculations.

The OSL sample processing and luminescence measurements using the single aliquot regeneration protocol (e.g. Murray and Wintle, 2000, 2003) are described here with radial plots that illustrate the distribution of the luminescence data (Figure F-1). Two samples, OV-OSL-04-01 and OV-OSL-04-02 were prepared in the St. Andrews luminescence laboratory. Unsieved wet samples were weighed and dried and a 180-212 μm size range extracted and treated to HCl and H_2O_2 until carbonates and organics were dissolved. The sediment was density separated and the <2.70 $g.cm^{-3}$ fraction was etched

in 40% HF for 80 minutes to dissolve feldspars and remove a few microns from the

surface of the quartz grains to minimize the luminescence due to ionization by external

alpha particles. Small quartz aliquots of (2-3 mm diameter) quartz grains were dispensed

onto stainless steel discs. OSL measurements using the SAR protocol (Murray and

Wintle, 2000, 2003) were made using a Risø TL/OSL-DA-15 reader. Luminescence

from the quartz grains was stimulated with both blue-green light (420 nm – 550 nm) from

a filtered halogen lamp (Bøtter-Jensen, 1997) and detected using a 9635QA

photomultiplier tube and Hoya U-340 filters. The standard sequence for the two samples,

after pre-heat and dose recovery tests, included a preheat temperature of $240^{o}C$ and an

infrared (IR) stimulation preceding the blue-green stimulation (Wallinga et al., 2002). In

addition to monitoring the luminescence sensitivity to preheat temperature and

establishing that the quartz from both samples passed a dose recovery test, SAR

measurements were only accepted if aliquots passed the recycling (within a ratio of 0.9-

1.1) and recuperation (<5%) tests. The equivalent dose (D_e) data are presented in radial

plots in Figure F-1. OV-OSL-04-01 has a fairly consistent luminescence behavior and

there is no evidence of partial bleaching. The data were modeled using Galbraith (2006)

finite age modeling techniques.

Table F-1. Equivalnet dose (D_e) data, dose rates and OSL ages for 180-212 μm quartz

Sample	U (ppm)	Th (ppm)	K (%)	Rb (ppm)	H_2O content[2] (%)	Cosmic dose-rate[3] (mGya^{-1})	Total dose-rate (mGya^{-1})	N[1]	Median D_e ± 1σ (Gy)	Modeled D_e ± 1 relative s.e. (Gy)	Age (ka)
OV-0SL-04-01	1.79±0.18	10.88±0.54	3.03±0.15	125.3±12.5	0.29	0.192	4.30±0.23	23	103.5±36.8	90.4±13.2	21.0±3.3 [§]
OV-0SL-04-02	7.66±0.77	17.77±0.89	2.72±0.14	116.6±11.6 6	0.23	0.192	5.86±0.31	28	51.1±24.7	36.5±10.2	6.2±1.8 [§†]

Notes:

1. Number of accepted D_e replicates.

2. Percent moisture compared to dry weight. Uncertainty is taken as 5%.

3. Cosmic dose-rate calculated assuming constant burial depth using method described in Prescott and Hutton (1994). Uncertainty is taken as 5%.

§ Ages calculated using D_e derived from Finite Age Model (FAM) and a single component solution (Galbraith, 1999).

† Ages calculated using D_e derived from FAM and first component solution (Galbraith, 1999).

‡ Age calculated using median D_e with 1σ error.
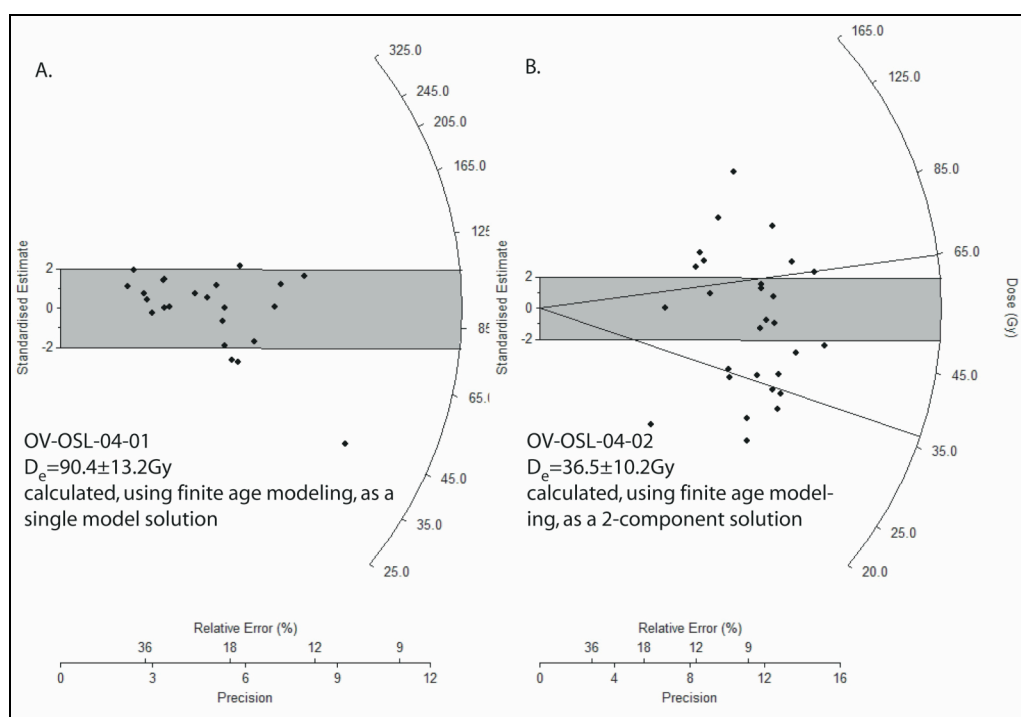
Figure F-1. Radial plot of equivalent dose (D$_e$) for OSL samples **A)** OV-OSL-04-01 and **B)** OV-OSL-04-02.

Appendix G

Fault Length Data Used in Chapter 5

Regional NE striking fault population	Number	Length (km)
TPF - Towne Pass fault	1	43
TMF - Tin Mountain fault	2	41
DSF - Deep Springs fault	3	35
EF - Emigrant fault	4	34
DMF - Dry Mountain fault	5	32
OLF- Owens Lake fault	6	26
QV - Queen Valley fault	7	17

Northen Owens Valley NE striking fault population	Number	Length (m)
THF - Tungsten Hills fault	1	13700
BF - Bishop Fault	2	3230
	3	1905
	4	1784
	5	1691
	6	1585
	7	1579
	8	1497
	9	1367
	10	1239
	11	1195
	12	1141
	13	1019
	14	890
	15	890
	16	771
	17	744
	18	707

Saline Valley NE striking fault population	Number	Length (m)
EVF - Eureka Valley fault	1	13412
	2	11873
	3	7794
	4	7609
	5	7263
	6	5463
	7	5382
	8	4945
	9	4941
	10	4771
	11	4271
	12	3986
	13	3979

Table G-1. Fault length data from the three northeast-striking fault populations within the ECSZ.

Saline Valley NE striking fault population	Number	Length (km)
	14	3839
	15	3814
	16	3778
	17	3777
	18	3702
	19	3698
	20	3697
	21	3627
	22	3481
	23	3320
	24	3085
	25	2954
	26	2919
	27	2900
	28	2878
	29	2779
	30	2681
	31	2589
	32	2516
	33	2407
	34	2393
	35	2342
	36	2329
	37	2234
	38	2212
	39	2159
	40	2113
	41	2113
	42	2096
	43	2014
	44	1987
	45	1980
	46	1971
	47	1936
	48	1918
	49	1917
	50	1909
	51	1873
	52	1856
	53	1797
	54	1748
	55	1744
	56	1672
	57	1663
	58	1647
	59	1635
	60	1634
	61	1605

Table G-1. (cont.)

Saline Valley NE striking fault population	Number	Length (km)
	62	1581
	63	1571
	64	1558
	65	1550
	66	1532
	67	1506
	68	1494
	69	1492
	70	1484
	71	1378
	72	1375
	73	1348
	74	1345
	75	1339
	76	1305
	77	1294
	78	1273
	79	1272
	80	1248
	81	1241
	82	1185
	83	1182
	84	1175
	85	1102
	86	1085
	87	1058
	88	1053
	89	1048
	90	1039
	91	1019
	92	1010
	93	1000
	94	983
	95	971
	96	970
	97	956
	98	955
	99	945
	100	934
	101	916
	102	915
	103	898
	104	890
	105	874
	106	854
	107	841
	108	835
	109	828

Table G-1. (cont.)

Saline Valley NE striking fault population	Number	Length (km)
	110	822
	111	818
	112	810
	113	789
	114	773
	115	771
	116	739
	117	737
	118	732
	119	721
	120	720
	121	705
	122	700
	123	691
	124	684
	125	675
	126	657
	127	652
	128	651
	129	650
	130	648
	131	645
	132	631
	133	623
	134	622
	135	614
	136	613
	137	594
	138	579
	139	578
	140	542
	141	514
	142	510
	143	497
	144	480
	145	461
	146	415
	147	398
	148	396
	149	354
	150	320
	151	292
	152	274

Table G-1. (cont.)

Number	Tableland (m)	Qt2 (m)	Qt3 (m)	Qt4 (m)
1	2909	1785	2091	460
2	2556	1498	1966	334
3	2441	1327	1415	298
4	2326	1027	1224	279
5	1971	866	758	258
6	1910	805	675	224
7	1832	646	598	222
8	1660	584	591	208
9	1652	573	552	205
10	1604	570	539	186
11	1541	545	511	164
12	1507	482	475	108
13	1500	470	466	106
14	1464	452	457	90
15	1423	427	409	80
16	1405	412	394	
17	1352	410	394	
18	1332	409	390	
19	1293	408	388	
20	1240	398	377	
21	1231	384	307	
22	1166	341	291	
23	1157	315	278	
24	1116	290	276	
25	1112	281	273	
26	1073	272	269	
27	1052	264	255	
28	1050	264	240	
29	1042	263	220	
30	1031	262	213	
31	1015	260	210	
32	986	257	194	
33	956	252	184	
34	906	250	170	
35	902	246	168	
36	899	244	159	
37	891	235	156	
38	878	231	124	
39	867	227	120	
40	864	225	109	

Table G-2. Fault length data (in meters) from the Volcanic Tableland, and the Owens River terraces: Qt2, Qt3, and QT4. Fault lengths are listed in descending order.

Number	Tableland (m)	Qt2 (m)	Qt3 (m)
41	846	206	106
42	844	203	103
43	796	196	72
44	785	195	56
45	784	195	
46	761	194	
47	752	184	
48	739	178	
49	738	173	
50	736	165	
51	729	164	
52	710	161	
53	710	153	
54	707	144	
55	707	141	
56	703	140	
57	702	131	
58	691	118	
59	670	109	
60	646	91	
61	639	86	
62	635	79	
63	631	75	
64	629	61	
65	615	45	
66	610	39	
67	605	38	
68	592		
69	577		
70	566		
71	561		
72	552		
73	544		
74	543		
75	536		
76	523		
77	522		
78	517		
79	513		
80	498		

Table G-2 (cont.)

Number	Tableland (m)	Number	Tableland (m)
81	491	121	223
82	489	122	216
83	485	123	213
84	483	124	211
85	474	125	210
86	468	126	207
87	462	127	202
88	459	128	164
89	456	129	159
90	441	130	143
91	432	131	135
92	431	132	104
93	425		
94	418		
95	416		
96	386		
97	371		
98	361		
99	358		
100	351		
101	350		
102	343		
103	336		
104	332		
105	330		
106	330		
107	317		
108	315		
109	308		
110	295		
111	288		
112	286		
113	263		
114	257		
115	255		
116	255		
117	252		
118	247		
119	228		
120	226		

Table G-2 (cont.)

LIST OF REFERENCES:

Ackermann, R.V., and Schlische, R.W., 1997, Anticlustering of small normal faults around larger faults: Geology, v. 25, p. 1127-1130.

Ackermann, R.V., Schlische, R.W., and Withjack, M.O., 2001, The geometric and statistical evolution of normal fault systems: an experimental study of the effects of mechanical layer thickness on scaling laws: Journal of Geophysical Research, v. 23, p. 1803-1819.

Anders, M.H., and Schlische, R.W., 1994, Overlapping faults, intrabasin highs, and the growth of normal faults: Journal of Geology, v. 102, p. 165-180.

Argus, D.F., and Gordon, R.G., 1991, Current Sierra Nevada-North America motion from very long baseline interferometry: Implications for the kinematics of the western United States: Geology, v. 19, p. 1085-1088.

Atwater, T., 1970, Implications of plate tectonics for the Cenozoic evolution of the western North America: Geological Society of America Bulletin, v. 81, p. 3513-3536.

Atwater, T., and Stock, J., 1998, Pacific North America plate tectonics of the Neogene southwestern United States: An update: International Geology Review, v. 40, p. 375-402.

Bachman, S.B., 1978, Pliocene-Pleistocene break-up of the Sierra Nevada-White-Inyo Mountains and formation of Owens Valley: Geology, v. 6, p. 461-463.

Bacon, S.N., Pezzopane, S. K., and Burke, B., 2003, Paleoseismology of the Owens Valley fault and latest Quaternary stratigraphy in Owens Valley near Lone Pine, eastern California: U.S. Geological Survey, Final Technical Report, National Earthquake Hazard Reduction Program, 42 pp.

Bateman, P.C., 1965, Geology and tungsten mineralization of the Bishop district, California: U.S. Geological Survey Professional Paper, v. 470, p. 208 p.

Beanland, S., and Clark, M.M., 1994, The Owens Valley fault zone, eastern California, and surface faulting associated with the 1872 earthquake: U.S. Geological Survey Bulletin, p. 30.

Bennett, R., Davis, J., and Wernicke, B., 1999, Present-day pattern of Cordilleran deformation in the western United States: Geology, v. 27, p. 371-374.

Bennett, R., Wernicke, B., Davis, J., Elosegui, P., Snow, J., Abolins, M., House, M., Stirewalt, G., and Ferrill, D., 1997, Global positioning system constraints on fault slip rates in the Death Valley region, California and Nevada: Geophysical Research Letters, v. 24, p. 3073-3076.

Benson, L.V., Burdett, J.W., Kashgarian, M., Lund, S.P., Phillips, F.M., and Rye, R.O., 1996, Climatic and hydrologic oscillations in the Owens Lake Basin and adjacent Sierra Nevada, California: Science, v. 274, p. 746-749.

Berry, M.E., 1990, Soil-Geomorphic analysis of late-Quaternary glaciation and faulting, eastern escarpment of the central Sierra Nevada, California [Ph.D. thesis], University of Colorado, Boulder.

—, 1994, Soil-Geomorphic analysis of Late-Pleistocene glacial sequences in the McGee, Pine, and Bishop Creek drainages, east-central Sierra Nevada: Quaternary Research, v. 41, p. 160-175.

—, 1997, Geomorphic analysis of late Quaternary faulting on Hilton Creek, Round Valley and Coyote warp faults, east-central Sierra Nevada, California, USA: Geomorphology, v. 20, p. 177-195.

Bierman, P.R., and Gillespie, A.R., 1994, Evidence suggesting that methods of rock-varnish cation-ratio are neither comparable nor consistently reliable: Quaternary Research, v. 41.

Birkeland, P.W., Berry, M.E., and Swanson, D.K., 1991, Use of soil catena field data for estimating relative field ages of moraines: Geology, v. 19, p. 281-283.

Bischoff, J.L., and Cummins, K., 2001, Wisconsin glaciation of the Sierra Nevada (79,000-15,000 yr B.P.) as recorded by rock flour in sediments of Owens Lake, California: Quaternary Research, v. 55, p. 14-24.

Blackwelder, E., 1932, Pleistocene glaciation in the Sierra Nevada and Basin Ranges: Geological Society of America Bulletin, v. 42, p. 865-922.

Bøtter-Jensen, L., 1997, Luminescence techniques: instrumentation and methods: Radiation Measurements, v. 27, p. 749-758.

Bryant, W., 1984, Evidence of recent faulting along the Owens Valley, Round Valley, and White Mountains fault zones, Inyo and Mono Counties, California Division of Mines and Geology Open-File Report OFR84-54SAC.

Burchfiel, B.C., Hodges, K.V., and Royden, L.H., 1987, Geology of Panamint Valley-Saline Valley pull-apart system, California: Palinspastic evidence for low-angle geometry of a Neogene Range-Bounding fault: Journal of Geophysical Research, v. 92, p. 10422-10426.

Burgmann, R., Pollard, D.D., and Martel, S.J., 1994, Slip distributions on faults: effects of stress gradients, inelastic deformation, heterogeneous host-rock stiffness, and fault interaction: Journal of Structural Geology, v. 16, p. 1675-1690.

Burroughs, S.M., and Tebbens, S.F., 2001, Upper-truncated power-laws in natural systems: Pure and Applied Geophysics, v. 158, p. 741-757.

Bursik, M.I., and Gillespie, A.R., 1993, Late-Pleistocene glaciation of Mono Basin, California: Quaternary Research, v. 39, p. 24-35.

Butler, P.R., Troxel, B.W., and Verosub, K.L., 1988, Late Cenozoic history and styles of deformation along the southern Death Valley fault zone, California: Geological Society of America Bulletin, v. 100, p. 402–410.

Chamberlain, C.P., and Poage, M. A., 2000, Reconstructing the paleotopography of mountain belts from the isotopic composition of authigenic minerals: Geology, v. 28, p. 115-118.

Cladouhos, T.T., and Marrett, R., 1996, Are fault growth and linkage models consistent with power-law distributions of fault length: Journal of Structural Geology, v. 18, p. 281-293.

Clark, D.H., and Gillespie, A.R., 1997, Timing and significance of late-glacial and Holocene cirque glaciation in the Sierra Nevada, California: Quaternary International, v. 38-39, p. 21-38.

Clifton, A.E., and Schlische, R.W., 2001, Nucleation, growth, and linkage of faults in oblique rift zones: Results from experimental clay models and implications for maximum fault size: Geology, v. 29, p. 455-458.

Clifton, A.E., Schlische, R.W., Withjack, M.O., and Ackermann, R.V., 2000, Influence of rift obliquity on fault-population systematics: results of experimental clay models: Journal of Structural Geology, v. 22, p. 1491-1509.

Cowie, P., Malinverno, A., Ryan, W., and Edwards, M., 1994, Quantitative fault studies on the East Pacific Rise: A comparison of sonar imaging techniques: Journal of Geophysical Research, v. 99, p. 15,205-15,218.

Cowie, P.A., and Scholz, C.H., 1992, Physical explanation for the displacement-length relationship of faults using a post-yield fracture mechanics model: Journal of Structural Geology, v. 14, p. 1133-1148.

Cowie, P.A., Sornette, D., and Vanneste, C., 1995, Mutifractal scaling properties of a growing fault population: Geophysical Journal International, v. 122, p. 457-469.

Cowie, P.A., 1998, A healing-reloading feedback control on the growth rate of seismogenic faults: Journal of Structural Geology, v. 20, p. 1075-10087.

Davy, P., Hansen, A., Bonnet, E., and Zhang, S., 1995, Localization and fault growth in layered brittle-ductile systems: Implications for deformation of the continental lithosphere: Journal of Geophysical Research, v. 100, p. 6281-294.

Dawers, N.H., Anders, M.H., and Scholz, C.H., 1993, Growth of normal faults: displacement-length scaling: Geology, v. 21, p. 1107-1110.

Dawers, N.H., and Anders, M.H., 1995, Displacement-length scaling and fault linkage: Journal of Structural Geology, v. 17, p. 607-614.

Densmore, A., Dawers, N., Gupta, S., Allen, P., and Gilpin, R., 2003, Landscape evolution at extensional relay zones: Journal of Geophysical Research v. 108, doi:10.1029/2001JB001741.

dePolo, C.M., 1989, Seismotectonics of the White Mountain fault system, eastern California and western Nevada [M.S. thesis]: Reno, University of Nevada.

—, 1998, A reconnaissance technique for estimating the slip rate of normal-slip faults in the Great Basin, and application to faults in Nevada, U.S.A. [Ph.D. thesis]: Reno, University of Nevada.

Dixon, T., Miller, M., Farina, F., Wang, H., and Johnson, D., 2000, Present-day motion of the Sierra Nevada block and some tectonic implications for the Basin and Range province, North American Cordillera: Tectonics, v. 19, p. 1-24.

Dixon, T., Norabuena, E., and Hotaling, L., 2003, Paleoseismology and Global Positioning System: Earthquake-cycle effects and geodetic versus geologic fault slip rates in the Eastern California shear zone: Geology, v. 31, p. 55-58.

Dixon, T.H., Robaudo, S., Lee, J., and Reheis, C., 1995, Constraints on present-day Basin and Range deformation from space geodesy: Tectonics, v. 14, p. 755-772.

Dokka, R.K., and Travis, C.J., 1990, Role of the Eastern California Shear Zone in accommodating Pacific-North America plate motion: Geophysical Research Letters, v. 17, p. 1323-1326.

—, 1990, Role of the Eastern California Shear Zone in accommodating Pacific-North America plate motion: Geophysical Research Letters, v. 17, p. 1323-1326.

Ferrill, D.A., Stamatakos, J.A., and Sims, D., 1999, Normal fault corrugation: implications for growth and seismicity of active normal faults: Journal of Structural Geology, v. 21, p. 1027-1038.

Galbraith, R.F., 2006, Statistics for fission track analysis. Chapman and Hall/CRC. 219 pp.

Gan, W., Svarc, J., Savage, J., and Prescott, W., 2000, Strain accumulation across the Eastern California Shear Zone at latitude 36 degrees 30 ' N: Journal of Geophysical Research, v. 105, p. 16229-16236.

—, 2000, Strain accumulation across the Eastern California Shear Zone at latitude 36 degrees 30 ' N: Journal of Geophysical Research-Solid Earth, v. 105, p. 16229-16236.

Gilbert, C.M., 1938, Welded tuff in eastern California: Geological Society of America Bulletin, v. 49, p. 1829-1862.

Gillespie, A.R., 1982, Quaternary glaciation and tectonism in the southeastern Sierra Nevada [Ph.D. thesis]: Pasadena, California, California Institute of Technology, 697 p.

—, 1988, Letter to the editor in response to article by Dorn et al.: Quaternary Research, v. 30, p. 102-103.

—, 1991, Quaternary subsidence in Owens Valley, California, in Proceedings of the White Mountain Research Station symposium, fall 1989: Los Angeles, White Mountain Research Station, p. 356-382.

Gross, M.R., Gutierrez-Alonso, G., Bai, T.X., Wacker, M.A., Collinsworth, K.B., and Behl, R.J., 1997, Influence of mechanical stratigraphy and kinematics on fault scaling relations: Journal of Structural Geology, v. 19, p. 171-183.

Gupta, A., and Scholz, C.H., 2000a, Brittle strain regime transition in the Afar depression: Implications for fault growth and seafloor spreading: Geology, v. 28, p. 1087-1090.

—, 2000b, A model of normal fault interaction based on observations and theory Journal of Structural Geology, v. 22, p. 865-879.

Hall, W.E., 1971, Geology of Panamint Butte Quadrangle, Inyo County, California: U.S. Geological Survey Bulletin, v. 1229, p. 67.

Hamilton, W.B., and Meyers, W.B., 1966, Cenozoic tectonics of the western United States: Review of Geophysics, v. 4, p. 509-549.

Hardacre, K.M., and Cowie, P.A., 2003, Controls on strain localization in a two-dimensional elastoplastic layer: Insights into size-frequency scaling of extensional fault populations: Journal of Geophysical Research, v. 108, 2529, doi:10.1029/2001JB001712.

Hollett, K.J., Danskin, W.R., McCaffrey, W.F., and Walti, C.L., 1991, Geology and water resources of Owens Valley, California, in Hydrology and soil-plant relations in Owens Valley, California:, U.S. Geological Survey, Water-Supply Paper 2370, p. 77.

Izett, G.A., and Obradovich, J.D., 1994, 40Ar/39Ar age constraints for the Jaramillo normal subchron and the Matuyama-Brunhes geomagnetic boundary: Journal of Geophysical Research, v. 99, p. 2925-2934.

Jackson, J.A., and McKenzie, D., 1983, The geometrical evolution of normal fault systems: Journal of Structural Geology, v. 5, p. 471-482.

Jackson, J.A., and White, N.J., 1989, Normal faulting in the upper continental crust: observations from regions of active extension: Journal of Structural Geology, v. 11, p. 15-36.

Jackson, J.A., and Leeder, M., 1994, Drainage systems and the development of normal faults: an example from Pleasant Valley, Nevada Journal of Structural Geology, v. 16, p. 1041-1059.

James, L.A., Harbor, J., Fabel, D., Dahms, D., and Elmore, D., 2002, Late Pleistocene glaciations in the northeastern Sierra Nevada, California: Quaternary Research, v. 57, p. 409-419.

Jennings, C.W., 1994, Fault activity map of California: California Division of Mines and Geology, Sacramento, scale 1:750,000.

Kirby, E., Burbank, D.W., Reheis, M., and Phillips, F., 2006, Temporal variations in slip rate of the White Mountain Fault Zone, Eastern California: Earth and Planetary Science Letters, v. 248, p. 153-170.

Koehler, P.A., and Anderson, R.S., 1995, Thirty thousand years of vegetation changes in the Alabama Hills, Owens Valley, California: Quaternary Research, v. 43, p. 238-248.

Larson, P.H., 1988, Relay structures in a Lower Permian basement involved extension system, East Greenland: Journal of Structural Geology, v. 10, p. 3-8.

Le, K., Lee, J., Owen, L., and Finkel, R., 2005, "Late Pleistocene to Holocene extension along the eastern Sierra Nevada, California", Geological Society of America Penrose Conference: Kinematics and Geodynamics of Intraplate Dextral Shear in the Eastern California and Western Nevada: April 21-26: Mammoth Lakes, California.

Lee, J., Stockli et al., D., Schroeder, J., Tincher, C., Bradley, D., and Owen, L., 2005, "Fault slip transfer in the Eastern California Shear Zone/Walker Lane Belt", Geological Society of America Penrose Conference: Kinematics and Geodynamics of Intraplate Dextral Shear in the Eastern California and Western Nevada: April 21-26: Mammoth Lakes, California.

Lee, J., Rubin, C., and Calvert, A., 2001b, Quaternary faulting history along the Deep Springs fault, California: Geological Society of America Bulletin, v. 113, p. 855-869.

Lee, J., Spencer, J., and Owen, L., 2001a, Holocene slip rates along the Owens Valley Fault, California: Implications for the recent evolution of the Eastern California Shear Zone: Geology, v. 29, p. 819-822.

Lubetkin, L.K.C., and Clark, M.M., 1988, Late Quaternary activity along the Lone Pine fault, eastern California: Geol. Soc. of Amer. Bull., v. 100, p. 755-766.

Malservisi, R., Furlong, K., and Dixon, T., 2001, Influence of the earthquake cycle and lithospheric rheology on the dynamics of the Eastern California shear zone: Geophysical Research Letters, v. 28, p. 2731-2734.

Marrett, R., and Allmendinger, R.W., 1991, Estimates of strain due to brittle faulting: sampling of fault populations: Journal of Structural Geology, v. 13, p. 735-738.

—, 1992, Amount of extension on "small" faults: An example from the Viking graben: Geology, v. 20, p. 47-50.

Massonnet, D., and Feigl, K., 1995, Satellite radar interferometric map of the coseismic deformation field of the M 6.1 Eureka Valley, California, earthquake of May 17, 1993: Geophysical Research Letters, v. 22, p. 1541-1544.

McClusky, S., Bjornstad, S., Hager, B., King, R., Meade, B., Miller, M., Monastero, F., and Souter, B., 2001, Present day kinematics of the Eastern California Shear Zone from a geodetically constrained block model: Geophysical Research Letters, v. 28, p. 3369-3372.

McLeod, A.E., Dawers, N.H., and Underhill, J.R., 2000, The propagation and linkage of normal faults: insights from the Strathspey-Brent-Statfjord fault array, northern North Sea: Basin Research, v. 12, p. 263-284.

Mensing, S.A., 2001, Late-glacial and early Holocene vegetation and climate change near Owens Lake, eastern California: Quaternary Research, v. 55, p. 57-65.

Miller, M., Johnson, D., Dixon, T., and Dokka, R., 2001, Refined kinematics of the Eastern California shear zone from GPS observations, 1993-1998: Journal of Geophysical Research, v. 106, p. 2245-2263.

Murray, A.S., and Wintle, A.G., 2000, Luminescence dating of quartz using an improved single-aliquot regenerative-dose protocol: Radiation Measurements, v. 32, p. 57-73.

—, 2003, The single aliquot regenerative dose protocol: potential for improvements in reliability: Radiation Measurements, v. 37, p. 377-381.

Nelson, C.A., 1971, Geologic map of the Waucoba Spring quadrangle, Inyo County, California, U.S. Geological Survey, Geologic Quadrangle Map GQ-921, scale 1:62,500.

Nicol, A., Watterson, J., Walsh, J.J. & Childs, C., 1996, The shapes, major axis orientations and displacement patterns of fault surfaces: Journal of Structural Geology, v. 18, p. 235-248.

Oldow, J., 2003, Active transtensional boundary zone between the western Great Basin and Sierra Nevada block, western US cordillera: Geology, v. 31, p. 1033-1036.

Oldow, J.S., Aiken, C.L.V., Hare, J.L., Ferguson, J.F., and Hardyman, R.F., 2001, Active displacement transfer and differential block motion within the central Walker Lane, western Great Basin: Geology, v. 29, p. 19-22.

Oldow, J.S., Kohler, G., and Donelick, R.A., 1994, Late Cenozoic extensional transfer in the Walker Lane strike-slip belt, Nevada: Geology, v. 22, p. 637-640.

Oswald, J.A., and Wesnousky, S.G., 2002, Neotectonics and Quaternary geology of the Hunter Mountain fault zone and Saline Valley region, southeastern California: Geomorphology, v. 42, p. 255-278.

Peacock, D.C.P., and Sanderson, D.J., 1991, Displacements, segment linkage and relay ramps in normal fault zones: Journal of Structural Geology, v. 13, p. 721-733.

Peltzer, G., Crampe, F., Hensley, S., and Rosen, P., 2001, Transient strain accumulation and fault interaction in the Eastern California shear zone: Geology, v. 29, p. 975-978.

Peltzer, G., and Rosen, P., 1995, Surface displacement of the 17 May 1993 Eureka Valley, California, earthquake observed by SAR interferometry: Science, v. 268, p. 1333-1336.

Phillips, F.M., Zreda, M.G., Smith, S.S., Elmore, D., Kubik, P.W., and Sharma, P., 1990, Cosmogenic chlorine-36 chronology for glacial deposits at Bloody Canyon, eastern Sierra Nevada California: Science, v. 248, p. 1529-1532.

Phillips, F.M., Zreda, M.G., Benson, L.V., Plummer, M.A., Elmore, D., and Sharma, P., 1996, Chronology for fluctuations in late Pleistocene Sierra Nevada glaciers and lakes: Science, v. 274.

Pickering, G., Bull, J.M., and Sanderson, D.J., 1995, Sampling power-law distributions: Tectonophysics, v. 248, p. 1-20.

Pinter, N., Keller, E.A., and West, R.B., 1994, Relative dating of terraces of the Owens River, Northern Owens Valley, California, and Correlation with Moraines of the Sierra Nevada: Quaternary Research, v. 42, p. 266-276.

Pinter, N., and Keller, E.A., 1995, Geomorphological analysis of neotectonic deformation, northern Owens Valley, California: Geologische Rundschau, v. 84, p. 200-212.

Pinter, N., 1995, Faulting on the Volcanic Tableland, Owens Valley, California: Journal of Geology, v. 103, p. 73-83.

—, 1995, Faulting on the Volcanic Tableland, Owens Valley, California: Journal of Geology, v. 103, p. 73-83.

Porinchu, D.F., MacDonald, G.M., Bloom, A.M., and Moser, K.A., 2003, Late Pleistocene and early Holocene climate and limnological changes in the Sierra Nevada, California, USA inferred from midges (Insecta, Diptera, Chironomidae): Palaeogeography, Palaeoclimatology, Palaeoecology, v. 198, p. 403-422.

Poulimenos, G., 2000, Scaling properties of normal fault populations in the western Corinth graben, Greece: implications for fault growth in large strain settings: Journal of Structural Geology, v. 22, p. 307-322.

Prescott, J.R., and Hutton, J.T., 1994, Cosmic ray contribution to dose rates for luminescence and ESR dating: Large depths and long-term time variations: Radiation Measurements, v. 23, p. 497-500.

Reheis, C., and Sawyer, T., 1997, Late Cenozoic history and slip rates of the Fish Lake Valley, Emigrant Peak, and Deep Springs fault zones, Nevada and California: Geological Society of America Bulletin, v. 109, p. 280-299.

Reheis, C., and Sawyer, T.L., 1997, Late Cenozoic history and slip rates of the Fish Lake Valley, Emigrant Peak, and Deep Springs fault zones, Nevada and California: Geological Society of America Bulletin, v. 109, p. 280-299.

Reheis, M., and Dixon, T., 1996, Kinematics of the Eastern California shear zone: Evidence for slip transfer from Owens and Saline Valley fault zones to Fish Lake Valley fault zone: Geology, v. 24, p. 339-342.

Rockwell, T., Lindvall, S., Herzberg, M., Murbach, D., Dawson, T., and Berger, G., 2000, Paleoseismology of the Johnson Valley, Kickapoo, and Homestead Valley faults: Clustering of earthquakes in the eastern California shear zone: Bulletin of the Seismological Society of America, v. 90, p. 1200-1236.

Ross, D.C., 1967, Geologic map of the Waucoba Wash quadrangle, Inyo County, California: U.S. Geological Survey, Geologic Quadrangle Map GQ-612, scale 1:62500.

Sarna-Wojcicki, A.M., Pringle, M.S., and Wijbrans, J., 2000, New Ar-40/Ar-39 age of the Bishop Tuff from multiple sites and sediment rate calibration for the Matuyama-Brunhes boundary: Journal of Geophysical Research-Solid Earth, v. 105, p. 21431-21443.

Sauber, J., Thatcher, W., Solomon, S.C., and Lisowski, M., 1994, Geodetic slip rate for the eastern California shear zone and the recurrence time of Mojave desert earthquakes: Nature, v. 367, p. 264-266.

Savage, J.C., Lisowski, M., and Prescott, W.H., 1990, An apparent shear zone trending north-northwest across the Mojave Desert into Owens Valley, Eastern California: Geophysical Research Letters, v. 17, p. 2113-2116.

Savage, J.C., and Lisowski, M., 1995, Strain accumulation in Owens Valley: Bulletin of the Seismological Society of America, v. 85, p. 151-158.

Schlische, R.W., and Anders, M. H. , 1996, Stratigraphic effects and tectonic implications of the growth of normal faults and extensional basins: Geological Society of America, Special Paper 303.

Scholz, C.H., and Cowie, P.A., 1990, Determination of total strain from faulting using slip measurements: Nature, v. 346, p. 837-839.

Scholz, C.H., Dawers, N.H., Yu, J.-J., Anders, M.H., and Cowie, P.A., 1993, Fault growth and fault scaling laws: preliminary results: Journal of Geophysical Research, v. 98, p. 21951-21961.

Scholz, C.H., 1997, Size distributions for large and small earthquakes: Bulletin of the Seismological Society of America, v. 87, p. 1074-1077.

—, 2000, The Mechanics of Earthquakes and Faulting: Cambridge University Press, Cambridge, England, 439 pp.

Scholz, C.H., and Contreras, J.C., 1998, Mechanics of continental rift architecture: Geology, v. 26, p. 967-970.

Schroeder, J.M., Lee, J., Owen, L., and Finkel, R., 2003, Pleistocene dextral fault slip along the White Mountains fault zone, California: Geological Society of America Abstracts with Programs, v. 35, p. 346.

Sharp, R.P., and Bierman, J. H., 1963, Additions to the classical sequence of Pleistocene glaciations, Sierra Nevada, California: Geological Society of America Bulletin, p. 1079-1086.

Sharp, R.P., and Glazner, A. F., 1997, Geology Underfoot in Death Valley and Owens Valley: Missoula, Montana., Mountain Press Publishing Company.

Sheridan, M.F., 1975, Tectonic displacement in the Bishop Tuff: California Geology, v. 28, p. 107-108.

Small, E.E., and Anderson, R.S., 1995, Geomorphically driven late Cenozoic rock uplift in the Sierra Nevada, California: Science, v. 270, p. 277-281.

Smith, K.D., and Priestley, K.F., 2000, Faulting in the 1986 Chalfant, California, sequence: local tectonics and earthquake source parameters: Bulletin of the Seismological Society of America, v. 90, p. 813-831.

Sornette, A., Davy, P., and Sornette, D., 1990, Growth of fractal fault patterns Physical Review Letters, v. 65, p. 2266-2269.

Spyropoulos, C., Griffith, W.J., Scholz, C.H., and Shaw, B.E., 1999, Experimental evidence for different strain regimes of crack populations in a clay model: Geophysical Research Letters, v. 261081-1084.

Spyropoulos, C., Scholz, C.H., and Shaw, B.E., 2002, Transition regimes for growing crack populations: Physical Review E, v. 65, p. -.

Stein, R.S., and Barrientos, S. E., 1985, Planar high angle faulting in the Basin and Range: geodetic analysis of the 1983 Borah Peak, Idaho, earthquake: Journal of Geophysical Research, v. 90, p. 11,355-11,366.

Sternlof, K.R., 1988, Structural style and kinematic history of the active Panamint-Saline extensional system, Inyo county, California [M.S. thesis]: Cambridge, Massachusetts Institute of Technology.

Stockli et al., D.F., Dumitru, T.A., McWilliams, M.O., and Farley, K.A., 2003, Cenozoic tectonic evolution of the White Mountains, California and Nevada: Geological Society of America Bulletin, v. 115, p. 788-816.

Taylor, G.F., 1934, Scarp ramp in northern Owens Valley: Geological Society of America Proceedings of 1933, p. 309.

Taylor, T., 2002, Origin and structure of the Poverty Hills, Owens Valley Fault Zone, Owens Valley, California [M.S. thesis], Miami University, Oxford, Ohio.

Thatcher, W., Foulger, G.R., Julian, B.R., Svarc, J., Quilty, E., and Bawden, G.W., 1999, Present-day deformation across the basin and range province, western United States: Science, v. 283, p. 1714-1718.

U.S. Geological Survey and California Geological Survey, Quaternary fault and fold database for the United States, accessed Oct. 19, 2006, from USGS web site: http//earthquakes.usgs.gov/regional/qfaults/.

Unruh, J., Humphrey, J., and Barron, A., 2003, Transtensional model for the Sierra Nevada frontal fault system, eastern California: Geology, v. 31, p. 327-330.

Unruh, J.R., 1991, The uplift of the sierra Nevada and implications for late Cenozoic epeirogeny in the western Cordillera: Geological Society of America Bulletin, v. 103, p. 1395-1404.

van den Bogaard, P., and Schirnick, C., 1995, 40Ar/39Ar laser probe ages of Bishop Tuff quartz phenocrysts substantiate long-lived silicic magma chamber at Long Valley, United States Geology, v. 23, p. 759-762.

Wallinga, J., 2002, On the detection of OSL age overestimation using single-aliquot techniques: Geochronometria, v. 21, p. 17-26.

Walsh, J.J., Watterson, J., and Yielding, G., 1991, The importance of small-scale faulting in regional extensional: Nature, v. 351, p. 391-393.

Wells, D.L., and Coppersmith, K.L., 1994, New empirical relationships among magnitude, rupture width, rupture area, and surface displacement: Bulletin of the Seismological Society of America, v. 84, p. 974-1002.

Wesnousky, S.G., 2005, The San Andreas and Walker Lane fault systems, western North America: transpression, transtension, cumulative slip and the structural evolution of a major transform plate boundary: Journal of Structural Geology, v. 27, p. 1505-1512.

Wesnousky, S.G., and Jones, C.H., 1994, Oblique slip, slip partitioning, spatial and temporal changes in the regional stress field, and the relative strength of active faults in the Basin and Range, western United States: Geology, v. 22, p. 1031-1034.

Wojtal, S.F., 1994, Fault scaling laws and the temporal evolution of fault systems: Journal of Structural Geology, v. 16, p. 603-612.

—, 1996, Changes in fault displacement populations correlated to linkage between faults: Journal of Structural Geology, v. 18, p. 265-279.

Zhang, P., Ellis, M., Slemmons, D.B., and Mao, F., 1990, Right-lateral displacements and the Holocene slip rate associated with prehistoric earthquakes along the southern Panamint valley fault zone: Implications for southern Basin and Range tectonics and coastal California deformation: Journal of Geophysical Research, v. 95, p. 4857-4872.

Zoback, M.L., 1989, State of stress and modern deformation of the northern Basin and Range province: Journal of Geophysical Research, v. 94, p. 7105-7128.

BIOGRAPHY

Timothy Patrick Sheehan was born to Patrick and Susan Sheehan on July 4th, 1978, at Oschner Hospital in what was then considered rural New Orleans (now Jefferson, Louisiana). After spending his first two years living on a farm near Picayune, Mississippi, the family, including a younger brother, Sean, moved to Jackson, Mississippi, where Patrick worked as a landman for Pruett Oil Company. When the oil industry took a downturn a year later, Patrick decided to open his own law practice in Biloxi, Mississippi. The family settled in nearby Ocean Springs where Tim attended grade school through high school. After graduating high school in the spring of 1997, he enrolled at Millsaps College in Jackson, Mississippi. His interest in geology was sparked during his sophomore year under the guidance of Dr. James Harris. During the next few years Tim excelled in his studies and eventually earned a B.S. in Geology with a minor in Computer Science. Soon after graduation, Tim applied for, and was accepted to a Ph.D. program in the Geology Department (currently the Department of Earth and Environmental Science) at Tulane University in New Orleans, Louisiana. He enrolled in the fall of 2001 under the guidance of Dr. Nancye Dawers. During the course of the next few years Tim spent several field seasons in Owens Valley collecting the data and observations that comprise the bulk of this project. During the summer of 2005, while still enrolled at Tulane, he received an internship offer from Shell Exploration and Production Company in New Orleans. The internship was cut short due to Hurricane Katrina, and Tim returned home to Ocean Springs where he helped his parents salvage what they could from the wreckage left by the storm. By January 2006, Tim was back in New Orleans where he began in earnest to complete his Ph.D. During the following summer he spent three months in the far northeast of Russia where he worked for Fortress Minerals, a gold exploration company. Upon returning from abroad, Tim was able to complete and successfully defend his dissertation on January 18th, 2007. Tim plans to start work in March 2007, with Shell Exploration and Production Company in New Orleans